Magnetars: Distances, Variability and Multi-Wavelength Observations

by

Martin Durant

A thesis submitted in conformity with the requirements
for the degree of Doctor of Philosophy
Graduate Department of Astronomy & Astrophysics
University of Toronto

Abstract

Magnetars: Distances, Variability and Multi-Wavelength Observations

Martin Durant
Doctor of Philosophy
Graduate Department of Astronomy & Astrophysics
University of Toronto
2006

The Anomalous X-ray Pulsars (AXPs) represent our best opportunity to study in detail the physics of magnetars: neutron stars with amazingly strong magnetic fields, so strong, that they fundamentally affect their energetics, evolution and appearance. In order to constraints the processes occurring in magnetar interiors and magnetospheres, I have conducted a phenomenological study of their behaviour.

I have observed AXPs in the infrared, optical and X-ray bands, and measured both their variability and global spectral energy distributions. By measuring the interstellar extinction, these spectra do not have the large uncertainties of previous works, and by measuring the distances to the objects, the spectra can be fairly compared. During this work: infrared or optical counterparts have been found for all but one AXP; the brightest source (4U 0142+61) was found to vary rapidly and significantly in each waveband over years of monitoring, yet with no apparent correlations between spectral regions; the contradictions in the previous measures of extinction were resolved; and all six Galactic AXPs had their distances determined and were placed on a map of the Galactic Plane.

From these studies, I find that, despite differences among AXPs and their variability in time, some patterns emerge. Perhaps most importantly, the X-ray luminosities of AXPs are very similar, as are their X-ray to infrared flux ratios. In this way, information is starting to mount with which to confront theoretical models, and understand the underlying conditions that give rise to the emission seen.

Acknowledgements

Thanks to my supervisor, Marten van Kerkwijk, whose ideas and methodology can be seen throughout this thesis. Thanks to others who helped me with my work over the last four years: the good people of McGill, Vik Dhillon, Bryan Gaesler and others. Specific thanks to those who helped to correct my thesis: Kevin, Hilding and Heather, and my external Deepto Chakrabarty. I have been dealt with well by telescopes, been glad for the existance of data archives, and had smooth computing throughout thanks to Hugh and Ross.

My parents have ever been behind me, when I needed reassurance; Szonya has told me just how to deal with the academic world, and finally, for keeping me going day to day, I thank Sharon.

Contents

Chapter 1

Introduction

1.1 Opening Remarks

This thesis is a phenomenological study of the Anomalous X-ray Pulsars (AXPs), one of the groups of magnetars: neutron stars whose energetics and evolution is dominated by their immense magnetic fields. They offer perhaps the best chance to study the behaviour of matter in the most extreme of environments (for electromagnetic effects with relativistic particles, for instance).

The AXPs as a group, have an interesting and rich range of observational characteristics. Although they (all six AXPs) share a number of parameters (spin, luminosity, X-ray spectrum), each object has certain behaviours and properties that make it unique. A central question then has to be, what causes the differences among the AXPs? Conversely, what intrinsic attribute of the AXPs sets them apart from the other types of neutron stars? In order to answer these questions, the properties and behaviours must first be thoroughly and systematically described.

In this introduction, I present the background material relating to my research on the AXPs. First I present a brief overview of neutron stars in general, and the motivations for their study. Next, I give a brief history of the observations of neutron stars in the various wavebands. This brings the reader to the state of play circa 1990, when radio pulsars and interacting binary systems were the only known manifestations of neutron stars.

The observed diversity of the neutron star population has changed rapidly in recent times, due to the discovery of objects, that were neither radio emitters nor in binary systems, with wave after wave of improving X-ray and γ-ray telescopes (Uhuru, Einstein, ROSAT, IPN, etc.). Current X-ray observatories such as *Chandra* and *XMM* have revolutionised astronomers' ability to observe in detail the emission of the various X-ray sources. As a consequence, the new X-ray sources have been classified into several groups, and it would seem that the demographics of neutron stars are not quite as simple as, at first, it would have appeared. I describe in brief the discovery and general parameters of the new classes.

With the arrival of heretofore unknown types of astronomical objects, new explanations were sought. One in particular, the *magnetar* theory was devised originally to account for the energetic outbursts of the Soft Gamma-ray Repeaters (SGRs), and later extended to describe the more sedate AXPs. This provides the theoretical framework upon which my investigation of the AXPs is based. I introduce the general ideas behind the magnetar model, and describe how they account for the properties of SGRs and AXPs. In the final part of the introduction, I describe the objects of interest themselves, the AXPs, giving details that will be referred to time and again throughout the rest of the thesis. I end with a very brief summary of this thesis, chapter by chapter.

1.2 Neutron Star Basics

Neutron stars are the compact remnants of massive stars which have ended their normal fusion-powered life. The heavy-element core collapses under its own gravity, and the resulting release of gravitational energy blows off the outer layers in a spectacular supernova. With typical mass $m \approx 1.4 M_\odot$ and radius $r \approx 10\,\mathrm{km}$, neutron stars represent the densest observable matter in the universe, even denser than the nuclei of atoms. As such, they offer the hope of investigating the properties of matter at extremes beyond the reach of laboratory-based experimentation, where high energies, densities, electro-magnetic fields and gravitational forces are all simultaneously important.

Neutron stars cannot be made of neutrons alone, but the description of neutron star interiors is still a matter of intense debate. The simplest description has a neutron-dominated star, with small concentrations of electrons and protons throughout the interior. A multitude of different models exist, however, including the possibility of condensation of the normal nucleons into higher-mass species (e.g., pions or even kaons, which include the strange-quark). Even the simplest models need detailed considerations of the thresholds to the onset of superfluidity and superconductivity. It is fair to say that researchers are far from settling on a particular *equation of state*. In any case, there must be a maximum mass, beyond which the degeneracy pressure and strong force is insufficient to withstand gravity, and thus a black hole or some more compact object is formed (cf., Chandrasekhar mass for white dwarfs).

The most basic properties which an observer might hope to measure for a neutron star, which would constrain the equation of state, are mass and radius. The most sought-after properties of neutron stars, which would constrain their internal physical processes, are temperature, mass and age. Much effort has gone into finding these, but in practice it has proven very hard through four decades of observations. The interplay of the magnetic field with superfluidity/superconductivity in the core and the implications for the energetics of neutron stars is immensely complicated. These effects, however, offer the chance to get a grip of physical processes beyond the realm of terrestial experimentation.

1.3 History of Neutron Star Observations

Landau (1932) suggested the existence of compact objects with nuclear densities. For reference, the neutron was discovered in 1932 by Chadwick (after Joliot-Curie & Joliot's and Bothe's earlier work) *after* Landau's prediction. Baade & Zwicky (1934) coined the term neutron star, and suggested they could be formed in the collapse of stars and that their creation might be responsible for the awesome energy release of a supernova.

It was many years until neutron stars were detected. Although the early V2 rocket-based X-ray experiments saw point-sources which later turned out to be neutron stars, it was Jocelyn Bell (Hewish et al. 1968) who first unambiguously identified the signal from neutron stars in radio observations. Interestingly, the pulsations they observed were so regular that initially no natural explanation could be thought of for their origin, and hence they were termed "Little Green Men" signals. The pulsations were soon linked with rotation, and became the defining characteristic for neutron stars (the rotation was too fast to be due to any known stars such as white dwarfs). As a lighthouse flashes when the light beam passes an observer's line of sight, so a neutron star pulses as it rotates.

Objects which emitted highly-pulsed regular radio signals with a well-defined period were termed (regular) *pulsars*. For example, the well studied Crab Pulsar, used often as a prototype system, has a whole vocabulary relating to its radio emission: glitches (sudden change in the pulse period), drifting sub-pulses, giant pulses, etc. Although radio pulsations have been observed for over thirty years, the emission mechanism is still not clear. There is certainly a strong beaming of radiation and particles associated with the magnetic poles, which, being offset by an angle to the rotational poles, causes the observer to see pulsations.

Pulsars have been modelled as pure magnetic dipoles spinning freely in space, spinning down due to the drag of the magnetic field at the speed-of-light cylinder ($\omega R_L = c$). Using this assumption, one can estimate the size of the magnetic field and age of the pulsar from the observed period and period derivative ($B = 3.2 \times 10^{19} (P\dot{P})^{1/2}\,\mathrm{G}$, $\tau = P/2\dot{P}\,\mathrm{s}$); thus the population has classically been plotted on $P - \dot{P}$ diagrams (see Figure 1.1). The quantities measured (P,$\dot{P}$) are real and physical even if the derived quantities are only estimates under the dipole radiation assumption. Such estimates point to the existence of a large range of magnetic fields ($B_{dipole} \sim 10^9 \ldots 10^{13}\,\mathrm{G}$) in the classical radio pulsar population. Since the emitted energy is derived from the rotational kinetic energy of the star, these radio pulsars are commonly referred to as "rotationally powered."

The canonical view of neutron star evolution is follows: neutron stars are born spinning rapidly (initial periods of order 10 ms) inside a supernova remnant (SNR). In the absence of a binary companion, pulsars spin down with constant magnetic field, such that $\dot{\nu} \propto \nu^n$, $n = 3$, and luminosity $\dot{E} = 4\pi^2 I \nu \dot{\nu}$ (I is the moment of inertia $\sim 10^{45}\,\mathrm{g\,cm^2}$ for the canonical neutron star, ν is the spin frequency, $\nu = 1/P$). That this view cannot be the whole story is clear from the fact that the few measured values of n are generally inconsistent with 3, with the majority slightly less than 3 and the extreme case of $n = 1.4 \pm 0.2$ inferred for PSR B0833$-$45 (the Vela pulsar; Lyne et al. 1996).

Aside from neutron stars detected in radio emission, another population of neutron stars has been known of for a long time, with periods ranging from milliseconds to hours, which are accreting matter from a binary companion. These are seen in X-rays and are termed either High-Mass (accretion from the wind of their massive companion) or Low-Mass (accretion from the overflowing Roche lobe of their evolved low-mass companion) X-ray Binaries. The detailed physics of the accretion process is an ongoing scientific puzzle. Pulsars which have undergone accretion at some point in their lives show up as millisecond or *recycled* radio pulsars with the shortest pulse periods and smallest period derivatives. They have gained angular momentum and lost magnetic flux due to the material they have accreted.

From the above, it is clear that plenty of puzzles remain for the isolated radio- and accreting X-ray pulsars (such as, how are radio pulsations formed?). Here, however, I concentrate on one of the relative newcomers on the neutron star scene, the AXPs.

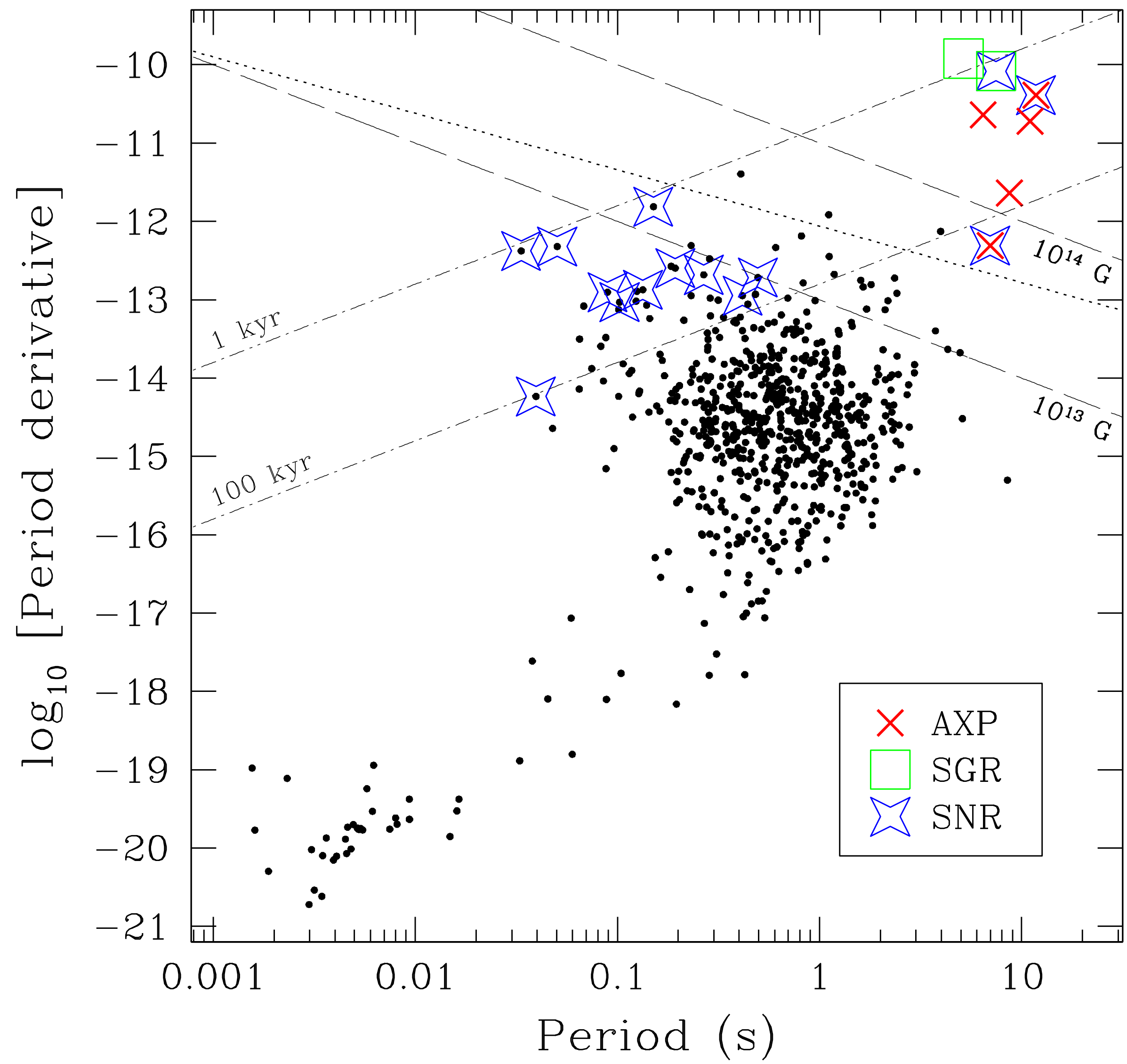

Figure 1.1 Period versus period derivative for the known isolated neutron stars. Overplotted are lines of constant characteristic age $\tau = P/2\dot{P}$ s and magnetic field $B = 3.2 \times 10^{19}(P\dot{P})^{1/2}$ G. Three distinct populations are seen: classical radio pulsars make up the bulk in the centre, with the younger, more energetic ones to the top left (often in supernova remnants, SNRs); millisecond pulsars located on the bottom left, the majority of which are in binary systems; and SGRs/AXPs show up in the high magnetic field area of the diagram in the top right. From Camilo et al. (2000)

1.4 New Diversity

For a long time the rotation-powered pulsars (classical radio pulsars or millisecond pulsars) and accretion-powered neutrons stars (X-ray binaries) were thought to cover the whole taxonomy of the field. It turns out that Nature is more varied. For instance, the AXPs are a group of neutron stars which do not fit within either the radio pulsar or accreting systems described in the previous section. In total, four distinct new classes of neutron star have been found, which are not detected in radio waves, are not rotation-powered, and have no binary companions. These are all newly discovered objects, or objects whose identity for a long time was not known. I wish to establish, first, the position of the Anomalous X-ray Pulsars within the growing phenomenological classification for the new types of neutron stars. Then, in §1.6, I will describe the properties of AXPs in more detail.

Table 1.1 lists the most basic properties of the different classes of neutron stars, showing their relationships to one-another.

1.4.1 Soft Gamma-ray Repeaters

As the name suggests, the Soft Gamma-ray Repeaters (SGRs) are characterised by sporadic energetic outbursts of hard X-ray, or soft gamma-ray emission. These outbursts tend to come in episodes of activity, sometimes with periods of years in-between. SGRs have been observed to emit much more energetic and longer-lasting *giant flares*, and persistent X-ray emission. Pulsations are seen as the giant flares fade, and have the same periods as eventually seen in the persistent X-ray emission from the sources, linking the periodicity with rotation. The SGRs have, so far, not been detected as radio pulsars.

The most recent and largest large flare from SGR 1806−20, which happened on 27 December 2004, was the most energetic Galactic outburst yet recorded. The SGR also was detected as a radio source immediately after the flare, the second SGR where this was possible (Cameron et al. 2005).

There currently are four known SGRs, three in the Galactic Plane and one in the Large Magellanic Cloud (LMC). The SGRs fall in the far top-right corner of Figure 1.1, suggesting extremely large magnetic fields. Association with SNRs (for one SGR; Kulkarni et al. 2003) and their location near star-forming regions, suggest that the SGRs are young neutron stars ($\sim 10^4$ yr).

1.4.2 Anomalous X-ray Pulsars

AXPs were discovered as pulsating point sources with various X-ray satellite observatories from *Uhuru* to *ROSAT* to *RXTE* and *Chandra*. In terms of spin-down parameters, luminosity and spectral shapes, the AXPs are remarkably similar to the SGRs, above (see Table 1.1), despite their very different methods of discovery. In Figure 1.1, the AXPs overlap somewhat with the SGRs, but with generally lower implied magnetic fields. Woods & Thompson (2004) give an excellent review of AXP (and SGR) properties.

The term *anomalous* refers to the initially unknown source of energy for their observed luminosity. The loss of rotational energy through spin-down is much less than the observed luminosity, and there is no evidence for binary companions.

There are currently six AXPs known, with a couple of candidate sources; candidates have similar pulse periods and luminosity as AXPs, but the period derivative has not been measured, or they have faded beyond easy detectability. The AXPs' basic properties are listed in Table 1.1. A more detailed description of the characteristics of the AXPs is given in §1.6 below. Two AXPs are very likely associated with SNRs, and so this class is also probably young, with ages of the order the life-time of a SNR ($T \sim 10^4 \ldots 10^5$ yr).

It is likely that the AXPs are closely related to the SGRs, by being perhaps evolutionarily connected, different states of the same intrinsic object type, or just the less energetic variation. However related, AXPs offer one huge observational advantage over SGRs: because they were detected in soft X-rays, they are not too highly extincted, and so the thermal part of their spectra and indeed optical and infrared counterparts can be observed. Thus, AXPs offer a window into the extreme energetics and magnetic field strengths, but with much more information available for un-tangling the physical picture.

1.4.3 Dim Isolated Neutron Stars

The *ROSAT* All Sky Survey (Voges et al. 1999) revealed seven sources with remarkably low interstellar hydrogen column densities, extremely low optical to X-ray flux ratios, and thermal spectra ($kT \sim 0.1$ keV). These sources are thus thought to be nearby neutron stars passively cooling, and their existence suggests a larger population of neutron stars in the Galaxy beyond that seen in the radio pulsars.

Recent observations have found pulsations for some Dim Isolated Neutron Stars (DINSs) with periods comparable to the AXPs and SGRs, whereas at least two show no pulsations to very good pulsed fraction limits. Strong, broad spectral features have been seen in at least four of the X-ray spectra, which can be explained best by proton cyclotron absorption or absorption by neutral hydrogen in moderate to strongly-magnetised atmospheres (generally, but not in every case, smaller values of magnetic field strength than those quoted for the SGRs or AXPs; e.g., van Kerkwijk et al. 2004). Their timing solutions also imply that they are older than AXPs or SGRs: might they just be older versions of the short-lived AXP/SGRs? The brightest DINS, RX J1856.5−3754 has failed to yield any spectral features as of yet, despite large amounts of observation time devoted to it (e.g., Burwitz et al. 2003).

1.4.4 Central Compact Objects

There exists a number of point sources located within supernova remnants, whose nature is unclear. In the category of Central Compact Objects (CCOs), fit all those objects which have not been classified elsewhere, but they are all associated with spatially coincident supernova remnants, and therefore neutron stars. They must also be very young (some historically dated), younger than the SGRs and AXPs appear to be.

The best studied case of a CCO is in Cas A, the 330 yr old SNR. The X-ray point source is more luminous than the DINSs, with a relatively hot spectrum ($kT \sim 0.5$ keV; Mereghetti et al. 2002), but very faint (i.e., with a small implied black-body radius) yet with no pulsations. To date, no optical or infrared counterpart to Cas A has been found down to deep limiting magnitudes (e.g., Fesen et al. 2006). Intriguingly, light echoes have been detected around Cas A, suggesting a luminous out-burst or flare similar to the SGRs within the last century

(Krause et al. 2005). This raises the interesting possibility: could CCOs be AXPs or SGRs in a prolonged quiet state?

1.4.5 High-B Radio Cut-off?

The AXPs and SGRs have inferred dipole magnetic fields which clearly set them apart from the radio pulsar population (see Figure 1.1). This could then be the explanation for their lack of radio emission: a high magnetic field suppresses the radio emission mechanisms (whatever that may be). If so, then the other radio-quiet neutron stars could be naturally explained as having high magnetic fields (but perhaps not high enough to power AXP or SGR-like energetics).

The first clue of possible evolutionary connection between radio pulsars and AXPs has been the discovery of radio pulsations from XTE 1810−197, some time after it ceased being AXP-like (more details in Section 1.6.4). CCOs are, after all, known to be younger than SGRs and AXPs, so some kind of progression is conceivable.

In Figure 1.1, the dotted line is the prediction of Baring & Harding (1998). It represents the boundary between ordinary radio pulsars and the region where the magnetic field was thought to be strong enough to quench radio emission. It turns out, however, that pulsars do exist in the region above the line. The new objects behave just like ordinary radio pulsars and not at all like the exotic objects described above. What is it, then, that makes the AXPs different from the high-B pulsars? With the decreasing gap between them and the radio pulsar population, can the DINSs and CCOs have a parameter space to reside in? The answers to these questions are not yet known, but one distinct possibility is that the difference lies in the structure of the internal magnetic field: a strong toroidal component or high-order multi-poles can create high-field conditions at or near the surface, but not affect the field far from the star (the timing method is sensitive to the field at the light cylinder, far from the star).

1.5 The Magnetar Theory

In order to make sense of the phenomenology of the AXPs, and to be able to draw some physical conclusions from the characterisation of their behaviour, an underlying theoretical basis is needed. This is provided by the magnetar model, which has become the standard description of AXPs and SGRs. All of the results later in this work are viewed in light of this theory, and so it needs first to be not only described in some detail (both its mechanisms and observational implications), but also a justification provided for why this is a reasonable starting point. Although at the time of starting this work (2003), the magnetar theory was already the leading contender for describing AXPs, there exists extensive literature suggesting one main alternative: that the luminosity is derived from the accretion of a supernova fall-back disc (Chatterjee et al. 2000). In Section 1.6, I describe the main reasons for taking the magnetar model as the most likely description of AXPs.

Used first to explain the bursting behaviour and giant flares with pulsed afterglow of the SGRs, the magnetar model has been extended to describe the persistent emission and evolution of the SGRs and AXPs (Thompson & Duncan, 1995, 1996). In some cases it has been invoked to describe the CCOs and DINSs, either in their present state or as an evolutionary link. At its most basic, the magnetar theory describes a neutron star with a large reservoir of internal magnetic energy (field strengths approaching $B \sim 10^{16}$ G), which dissipates with time through the crust, and powers the observed X-ray luminosity.

The argument that SGR flares require magnetar-strength magnetic fields ($\sim 10^{14}$ G) is as follows. The pulsations observed (period, $P \sim 10$ s) are most easily explained as coming about from the rotation of a neutron star, with the emission localised to within one radius above its surface. The temperature of the radiation requires the presence of $e^{\pm}$ pairs, the long duration of the pulsation tail requires strong confinement and the total emergent flux requires a very large energy source. These can be simultaneously satisfied by a dense pair-plasma in a hot fireball confined by a magnetar-strength magnetic field. Such intense radiation ($L \gg L_{Eddington}$) can be explained by the suppression of opacities as a consequence of super-strong magnetic fields.

The first confirmation of this theory was the detection of slow ($P \sim 10$ s) pulsations, rapidly spinning down, in SGRs (Cline et al. 1980). The SGRs and AXPs fall into the high-B-field part of Figure 1.1. They are joined by the high-B regular (radio) pulsars, and one might ask what causes the distinction between them. The field inferred from the spin parameters is the dipole component, and much higher surface and internal fields is possible for any given dipole. The magnetar theory argues that it is the internal magnetic field energy reservoir which distinguishes the magnetars from other neutron stars.

Below, I give details of the magnetar model, starting with possible origins for such a strong magnetic field, then discussing the evolution of this field in energy terms, and finally describing how this translates into radiative emission and observational implications.

1.5.1 Origins

In order to explain the physical properties of SGRs, neutron star internal magnetic fields up to $B \sim 10^{16}$ G must exist. Such high field strengths are possible, but is there any physical justification for their existence? Three plausible scenarios have been suggested for strongly magnetised neutron stars.:

- Flux conservation from the neutron star predecessor. If flux is conserved, then the flux density goes as R^{-2} as a main-sequence star (or white dwarf) collapses to a neutron star, so large amplifications of B are therefore possible. White dwarfs with field strengths high enough to do this are not known, but there may be a population of O-stars with anomalously high magnetic fields (e.g., Ferrario & Wickramasinghe, 2006).

- Differential rotation in the nascent neutron star. Due to the rapid collapse of many mass shells from the progenitor star into the newly-created neutron star, there will be very strong differential rotation in the early stages after formation. This mechanism is effective only for short initial spin periods of $\sim$1 ms, but that might not be rare in the inital stages of supernova collapse (Akiyama et al. 2003).

- Neutrino-driven convection. Thompson & Duncan (1993) present a model where an initially much smaller field in the nascent neutron star is amplified through dynamo action. The seed field can come from either the progenitor or differential rotation during the collapse phase. This also requires a fast initial spin of order 10 ms.

Models of supernovae are still unable to describe the complex phenomenology and classification of observed events, and, in fact, have trouble simulating any supernovae explosions at all. It is not until recently that the first numerical simulations were able to follow a star through collapse to a proto-neutron star. The details of the supernovae themselves, and how magnetic fields are imparted to neutron stars, is another discussion altogether. For the sake of brevity, we assume that some fraction of neutron stars acquire $B > 10^{15}\,\mathrm{G}$ internal magnetic fields, which are stable over long periods. If the magnetic field is generated on scales smaller than the neutron star (e.g., $\sim 1\,\mathrm{km}$ for the dynamo action), than a significant portion of the magnetic field will be stored in non-dipolar geometry, such as a toroidal field (Thompson & Duncan, 1993).

1.5.2 Energetics

Before considering the details of the magnetar model and the various implications of it, it should be pointed out that there will in every case be two distinctive mechanisms for the dissipation of magnetic energy: internal heating and external particle acceleration.

Thompson, Lyutikov & Kulkarni (2002) developed a model for the persistent X-ray emission from magnetars, within the framework of a globally twisted dipolar external magnetic field around a magnetar. They considered the *force-free* case, where the energy density associated with the local magnetic flux density dominates over particle kinetic energy (and inertia) throughout the magnetosphere.

Figure 1.2 illustrates the mechanism by which an internal twist of the magnetic field is transferred to the exterior magnetosphere of the magnetar. In the initial case (left side), a large toroidal component exists in the interior twisted magnetic field, along with the global poloidal component. The toroidal part is maintained by a current along the helix, which closes within the highly conductive neutron star. Some current, therefore, crosses the field lines near the surface and induces a torque. The crust will deform either plastically or in rigid quakes; the latter giving rise to short, sharp outbursts of energy. As the crust yields, the external field lines are twisted up, and some current is forced into the magnetosphere to maintain this twist (right side of diagram). The net effect is the transferral of helicity (i.e., toroidal field) from the interior to the exterior, releasing energy.

There are two major sources of energy dissipation: the gradual relaxation of the internal magnetic field gives rise to deep heating in the core, and the external current gives rise to external dissipation of the twist on a much shorter timescale. The transfer of a large reservoir of stored energy in magnetism to luminosity is thus explained through the periodic twisting and relaxation of the magnetic field. This process also implies the existence of a large density of charges in the magnetosphere, which present an optical depth of order unity to cyclotron resonant absorption at any frequency.

1.5.3 Emission Mechanisms

Magnetar bursting is due to the intermittent expulsion of internal toroidal magnetic energy into an external magnetospheric twist. An external twist dissipates with time by driving currents through the magnetosphere. When the external magnetic field is twisted up faster than the twist dissipates, it eventually becomes unstable to global magnetic reconnection (when the twist angle, $\Delta\phi \approx 1$). This sudden release of energy produces a pair-plasma

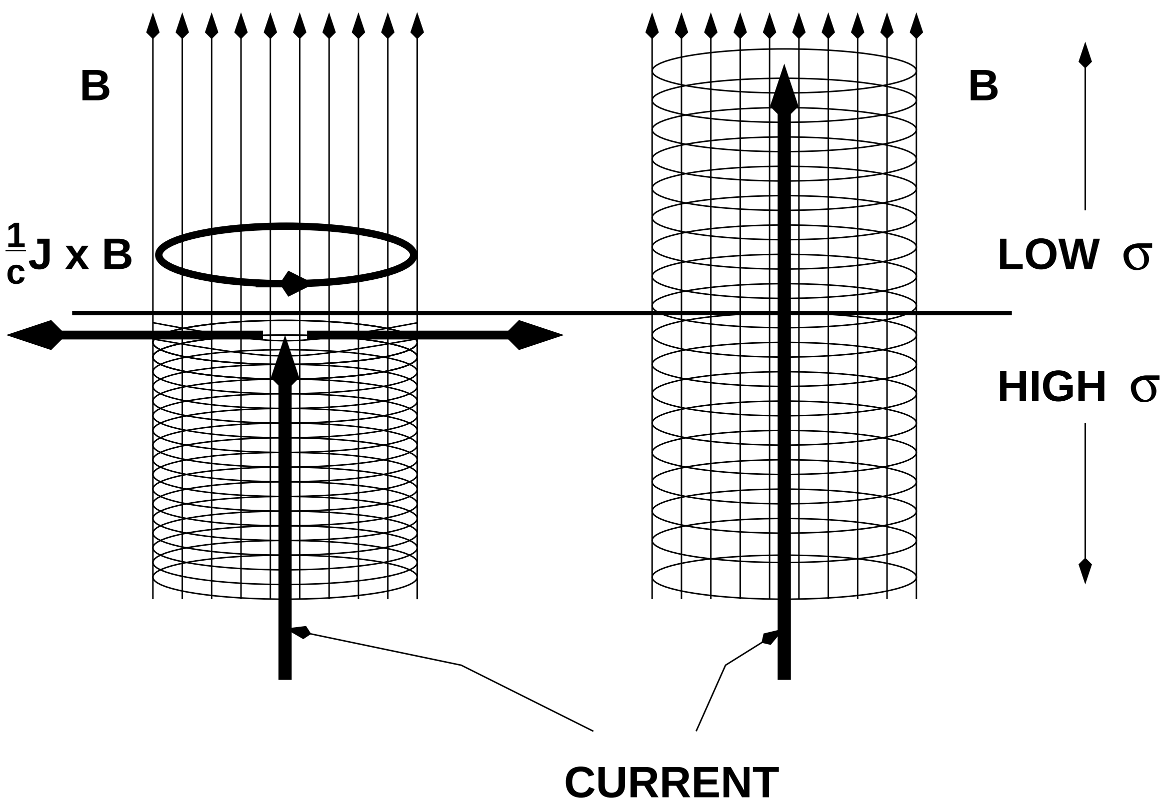

Figure 1.2 Expulsion of toroidal field into an external magnetospheric twist. $\frac{1}{c}\mathbf{J} \times \mathbf{B}$ is the Lorenz force (torsional in this case) and σ is electrical conductivity: high in the neutron star crust and interior. Taken from Thompson, Lyutikov & Kulkarni (2002).

fireball confined to the magnetosphere by field lines, and results in the giant flares observed from the SGRs.

Lyutikov (2003) suggested a mechanism for the emission of energy stored in the magnetospheric currents through the tearing mode instability between adjacent current sheets. Later, the model was extended to include both explosive reconnection events (which would appear as flares) and repeated up-scattering of photons off hot magnetospheric particles at the cyclotron resonances, which can produce an extended high-energy tail to the emergent spectrum.

More recently, Beleborodov & Thompson (2006) extend their model to consider the acceleration of particles in the magnetosphere. The system can be viewed as an electric circuit problem along a bundle of field lines. At voltages around 1 GeV, pairs are created which screen the electric field and suppress further acceleration. This acts as a choke and regulates the rate of energy release by keeping the voltage along field lines near the pair-production threshold. A magnetic twist is expected to be dissipated in time-scales of order decades.

As far as optical emission is concerned, the picture is not yet clear. Three plausible emission mechanisms have been suggested: coherent plasma radiation from dense bunches near the stellar surface (Eichler et al. 2002), ion cyclotron radiation far from the star by absorption of long wavelength photons and re-emission closer to the star, and curvature radiation by pairs (Thompson & Beloborodov).

1.5.4 Radiative Processes

The external magnetic field strength of magnetars, of order 10^{15} G is above the so-called Quantum Electro-Dynamic (QED) -critical field where the Landau gyrational energy (quanta of transverse motion about the magnetic field) of an electron equals its rest-mass:

$$\frac{\hbar e B_{QED}}{m_e c} = m_e c^2 \tag{1.1}$$

This yields a field of $B_{QED} = 4.4 \times 10^{13}$ G. In this regime, a number of processes become important, which are forbidden or suppressed at lower fields:

- the vacuum becomes birefringent, with the opacities of photons with electric vectors perpendicular to the local B-field much suppressed compared to electric vectors with a component along the field, because electrons do not want to be accelerated across field lines
- photon modes can swap over at the *vacuum resonance* where plasma and vacuum effects are of equal importance, as a photon leaves the dense crust (Ho & Lai, 2003)
- atomic binding energies increase dramatically as the transverse motion of electrons is suppressed, making a condensed surface of atomic polymer possible
- photons can split (and merge), the momentum being conserved by the magnetic field.

See Duncan (2000), for a derivation of each high-B effect from fundamental principles. Considerations of the emergence of radiant energy from a magnetar must include these effects, which are generally geometry-dependent. In general, these effects greatly complicate the modelling of radiative transfer and emergent spectra from the neutron star surface.

1.6 The Anomalous X-ray Pulsars in Detail

AXPs were termed *anomalous*, since the origin of their X-ray luminosity was not at first known. The two main contenders which arose were the magnetar model (see §1.5) and the disc accretion model. I summarise the reasons for not considering it further in this thesis in §1.6.5.

In the chapters that follow, all of the AXPs are investigated. They share a number of properties (e.g., spin parameters and spectral shapes; see Table 1.1), but there are, however a number of differences among them. The details of their similarities and differences are listed below, as a reference for later chapters, which refer to specific objects within the AXP class.

As a group, AXPs have one large observational advantage over the SGRs: since they were detected not by their outbursts, but by their quiescent emission, their steady state (which they are in the vast majority of the time) is much easier to investigate. Specifically, the SGRs are generally too highly extincted to be able to detect the soft part of their X-ray emission, or optical/infrared counterparts.

There are five AXPs lying in the plane of the Galaxy (within 1°), and one in the Small Magellanic Cloud. In addition, there are two candidate AXPs, which were observed with AXP-like properties, but only for particular epochs. They are sometimes referred to as *transient AXPs*, as they only seem to have similar luminosity to the other AXPs during heightened activity periods. Although all the AXPs appear to be variable on some level, none of the six have faded to the low levels shown by the transient AXPs.

Two AXPs (and one candidate) are associated with SNRs, lying close to the centres of these. The remaining AXPs are not seen near SNRs, however, which given their short life-spans, indicates either that the supernovae were of low energies, were within a low density medium, did not leave a remnant at all or that perhaps the magnetars received large kicks (momentum imparted by the supernova explosion). The simplest resolution to this would be that the magnetars are older than we think.

1.6.1 Timing Characteristics

Compared to classical radio pulsars, the AXPs are slow rotators ($P \sim 10\,\mathrm{s}$), but with rapid spin-down. They inhabit the upper right-hand corner of Figure 1.1, implying a strong magnetic field out to the light cylinder (i.e., the dipole component $B_{dipole} \sim 10^{14}$–$10^{15}\,\mathrm{G}$).

None of the AXPs show any evidence of modulation of their spin period by an unseen binary companion. The AXPs have fairly sinusoidal pulse profiles, with pulsed fractions ranging from a few percent, for 4U 0142+61, to upwards of 60%, for 1E 1048.1−5937. The pulse profiles and pulsed fractions are energy dependant, but only weakly.

All the AXPs spin down persistently, some with highly regular spin-down, well described by a simple ephemeris (e.g., 4U 0142+61; Gavriil & Kaspi, 2002), others with a considerable amount of deviation from a simple model (1E 1048.1−5937; Gavriil & Kaspi, 2004). Glitching (a sudden increase in spin frequency, accompanied by enhanced spin-down) has been observed in the AXPs, possibly coincident with bursting (see below) or active phases.

The characteristic ages of the two AXPs associated with SNRs do not match the inferred ages of those remnants (1E 2259+586 and 1E 1845−045; Gaensler et al. 2001). The AXPs'

Table 1.1. Measured properties of a selection of neutron stars, including all of the AXPs and candidate AXPs.

Object	P (s)	B_{dipole} (10^{13} G)	T_{bb} (keV)	Radio	Optical/ IR	SNR	Bursts
SGRs							
SGR 1806−20	7.5	78		afterglow	IR	no	yes
SGR 0526−66	8.0	74	0.53	no	no	possible	yes
SGR 1627−41	6.4			no	no	no	yes
SGR 1900+14	5.2	57	0.43	afterglow	no	no	yes
AXPs							
CXOU J010043.1−721134	8.0		0.41	no	optical[b]	no	no
4U 0142+61	8.7	13	0.46	no	both	no	no
1E 1048.1−5937	6.4	39	0.63	no	IR	no	yes
1RXS J170849.0−400910	11.0	47	0.44	no	IR[c]	no	no
XTE J1810−197[a]	5.5	29	0.67	no	IR	no	no
1E 1841−045	11.8	71	0.44	no	no	yes	no
AX J1845−0258[a]	7.0			no	no	yes	no
1E 2259+586	7.0	6	0.41	no	IR	yes	yes
DINSs							
RX J0720.4−3125	8.4	2.3	0.08	no	optical	no	no
RX J1605.3+3249			0.1	no	optical	no	no
CCOs							
Cas A XPS			0.5	no	no	yes	no
High-B pulsars							
PSR J1119−6127	0.4	4.1		yes	no	no	no
PSR J1814−1744	3.975	5.5		yes	no	no	no

Note. — Basic measurable properties of different types of neutron stars, with all the AXPs and example objects for the other categories.

[a] "Transient" AXP, only *on* as an AXP some of the time. The numbers reflect the high on state.

[b] The optical counterpart is discussed in §3.1.

[c] The IR counterpart is discussed in §3.3.

characteristic ages are too long, indicating either that their initial spin periods were long (1–5 s) or that their rate of spin-down are significantly lower now than their historical average.

1.6.2 X-ray Spectra

All the AXPs show a spectral peak in the soft-X-rays, usually interpreted as a thermal component (in which case, black-body temperatures of the order $kT \approx 0.5\,\mathrm{keV}$ are inferred), coming from some fraction of the neutron star surface. The spectrum then falls with a soft power-law to the $\sim$10 keV range, slower than a Wien tail. The spectra have often been fitted with a combination of continuum models, for example the sum of a black-body and a power-law, extincted by interstellar absorbing matter. These models adequately fit the data.

No spectral features have been found to date for an AXP, apart from hints of transient features or lines seen only at certain phases of pulsation (Rea et al. 2003) and not confirmed by other instruments.

In efforts to model the pulsation of AXPs, generally the same types of fits have been performed for each phase bin as are used for the phase-averaged spectra. Although the parameters (e.g., black-body and power-law relative normalisation) are found to change from phase to phase, no systematic model has yet been made to explain how the pulsation is manifested. In general, the pulsed fraction increases with energy, and an anti-correlation between pulsed flux and total flux has been reported (for 1E 1048.1−5937; Tiengo et al. 2005).

1.6.3 Optical and Infrared

The first detection of an AXP in the optical was of 4U 0142+61 by Hulleman et al. (2000). Since then, counterparts to some of the other AXPs have been found, all in the infrared. The reason for this is that there is considerable extinction to each of the (Galactic) AXPs, which affects least the infrared, and particularly the K-band (the M- and L-bands are very hard to observe in, due to sky brightness).

The photometric points in the optical and infrared fall, in every case, well below (by orders of magnitude) extrapolations of the power-law tails seen in the 2–10 keV range, yet well above extrapolations of the black-body spectral components. This was used by Hulleman et al. (2004) as the clinching argument for the magnetar hypothesis: were the luminosity of an AXP powered by accretion from a faint companion or fallback accretion disc, the high temperatures of infalling material would assure a much higher optical/infrared flux than that which is seen (but see also 1.6.5).

Intriguingly, the spectral energy distribution derived by Hulleman et al. for the brightest AXP, 4U 0142+61, shows a sharp cutoff at the B-band: a significant optical spectral feature.

1.6.4 Recent Developments

It was a great success for the magnetar theory, when first 1E 1048.1−5937, and then 1E 2259+586 were observed to burst in a similar way to the SGRs in RXTE monitoring data (e.g., Gavriil et al. 2002). Intriguingly, SGR 1627−41 and SGR 0526−66 have not shown any bursting activity for years, and appear more similar to AXPs (e.g., Kouveliotou et al. 2003). One concludes that either the SGRs and AXPs form a continuum of properties, resulting in differing recurrence times for their periods of activity, or perhaps objects evolve from one type of source to the other (probably SGR to AXP).

Kern & Martin (2002) observed strong pulsations in the optical emission of 4U 0142+61, with an even higher pulsed fraction (≈27%) than in X-rays. This was confirmed by Dhillon et al. (2005), who found 29±8%. The period of the pulsations is identical to the X-ray pulse period, indicating that both share the same cause: the rotation of the neutron star. Since the pulsed fraction in the optical is higher than in X-rays (and so cannot be produced by reprocessing), the optical emission must originate from near the stellar surface in the magnetosphere, rather than from any circumstellar material.

In the case that the crust of a neutron star is torqued by the magnetic field extending to the light cylinder, and that the interior is superfluid, one would expect glitching behaviour: sudden transferral of angular momentum from the core to the crust through magnetic stress. At least two of the AXPs have been seen to glitch: 1RXS J170849.0−400910 and 1E 2259+586 (Kaspi et al. 2000; Dall'Osso et al. 2003; Woods et al. 2004). It is possible that some fraction of the timing noise seen in AXPs is due to unresolved glitching behaviour.

Variability has become one of the most readily recognised characteristic of AXPs, in both the infrared (e.g., Hulleman et al. 2004) and X-rays (e.g., Mereghetti et al. 2004). In two cases, the X-ray and infrared appear to have brightened simultaneously: for 1E 2259+586 (Tam et al. 2004) and XTE J1810−197 (the object was discovered in this "high" state; Gotthelf et al. 2004). With limited data-points, the optical magnitudes of 4U 0142+61 (the only one detected as of 2004) were consistent with no variability.

Wang et al. (2006) detected 4U 0142+61 in the mid-infrared using the *Spitzer* satellite observatory. From their two photometry points, they infer a large infrared excess (above the extrapolation of near-infrared photometry), which can be fit as a thermal spectrum. The implication is the existence of a circumstellar disc, which re-radiates at low energies, high-energy radiation incident upon it. The inner radius of the disc matches the location of the onset of dust sublimation. Thus, they propose that the disc is the dusty remnant of fallback material from the supernova which created the magnetar. Any accretion would be at much too low a level to significantly affect the energetics of the magnetar at higher frequencies. Such a detection has thus far not been made for any other of the AXPs. It will be very interesting to see if dust features are seen in the Spitzer spectrum, when it is observed.

1E 1841−045 was the first AXP detected in hard X-rays (20–200 keV) with INTEGRAL and RXTE/HEXTE (Kuiper et al. 2004). Since then, two and possibly three more have been detected, with similar characteristics: the radiation is highly pulsed, and has a very hard spectrum (den Hartog et al. 2006; Kuiper et al. 2006). The energy contained in these high-energy tails dominates the emission. From archival CGRO/COMPTEL observations, the spectra must turn over in each case below ~ 500 keV, but the location and shape of this turnover is not yet known. Interestingly, the pulsation of the highest energy part of the spectrum has a peak which is shifted in phase with respect to the soft-X-rays (in intermediate energy ranges, both peaks are visible). This seems to be a feature of every source with INTEGRAL detections, and indicates that different mechanisms power the soft- and hard-X-rays.

Following the INTEGRAL discoveries, additional work was required in the magnetar model to explain the previously unseen large energy output. The extension of the magnetar model accounting for particle interactions (Beloborodov & Thompson, 2006; see also §1.5.3, above), achieves this, and explains the form and luminosity of the high-energy tail.

With the new spectral windows now open, see Figure 1.3 for the latest spectral energy distribution of 4U 0142+61 at the end of the thesis. From this, one can judge the relative energetic importance of the different measurements.

In breaking news: XTE 1810−197, the objects which appeared as an AXP only for a brief time, before fading in both X-ray and infrared brightness, has been detected as a radio pulsar by Camilo et al. (2006). This critically demonstrates that transitions between the energetic AXP-like behaviour and radio-emitting pulsar behaviour are possible.

1.6.5 Alternative Theoretical Descriptions

In this thesis I assume that the magnetar theory (§1.5) is the best description of the AXPs. It has become the leading theory and generally accepted during the progress of this work. The main contender is the idea that some material from the supernova explosion does not escape the system, but forms an accretion disc, which powers the observed X-ray luminosity, analogous to binary accretion systems (which are also X-ray bright and have energetic outbursts; Chatterjee et al. 2000).

An advantage of the disc model is that it provides a fairly natural explanation for the spin periods seen: these are roughly equal to the equilibrium spin period expected for a neutron star with a (dipole) magnetic field strength similar to that of normal radio pulsars which is accreting at a rate required to power the X-ray luminosity (Alpar et al. 2001). However, there are number of problems. The first is that the optical emission of 4U 0142+61 is substantially below what was predicted for an irradiated accretion disc (Hulleman et al. 2000). It may be possible, however, to reproduce the optical and infrared emission at least qualitatively by adjusting the reprocessing efficiency and other parameters (e.g., Ertan et al. 2006). Although this does not seem to account for all detais (such as the sharp break between V and B), the advantage is that this accounts fairly naturally for the mid-infrared counterpart discovered by Wang et al. (2006), which in the context of the magnetar model may require a rather ad-hoc presence of a debris disk. It does not seem possible, however, to account in a simple fashion for the fact that the optical emission is strongly pulsed. Indeed, in accreting X-ray binaries such as Her X-1 (Middleditch & Nelson, 1976) and 4U 1626−67 (Middleditch et al. 1981), only weak optical pulsations are seen.

But perhaps the most severe problem is that in the context of an accretion scenario, there is no explanation for the extremely short but hard X-ray bursts and for the SGR flares, which are so unlike anything seen in any known accreting binary. Indeed, recently hybrid models have been proposed (Ertan & Alpar, 2003), in which the dipole magnetic field strength is relatively low and the main source of energy is from accretion, but in which the short bursts and flares are due to magnetic events in much stronger magnetic fields near the surface. In our opinion, however, this makes the model overly complicated compared to the magnetar model. For completeness, we note that this thesis presents further observations that appear inconsistent with an accretion scenario: the rapid variability in the K-band flux of 4U 0142+61 without corresponding variability in the X-ray (Chapter 4); and the similarity of the X-ray luminosities of all the AXPs (Chapter 6).

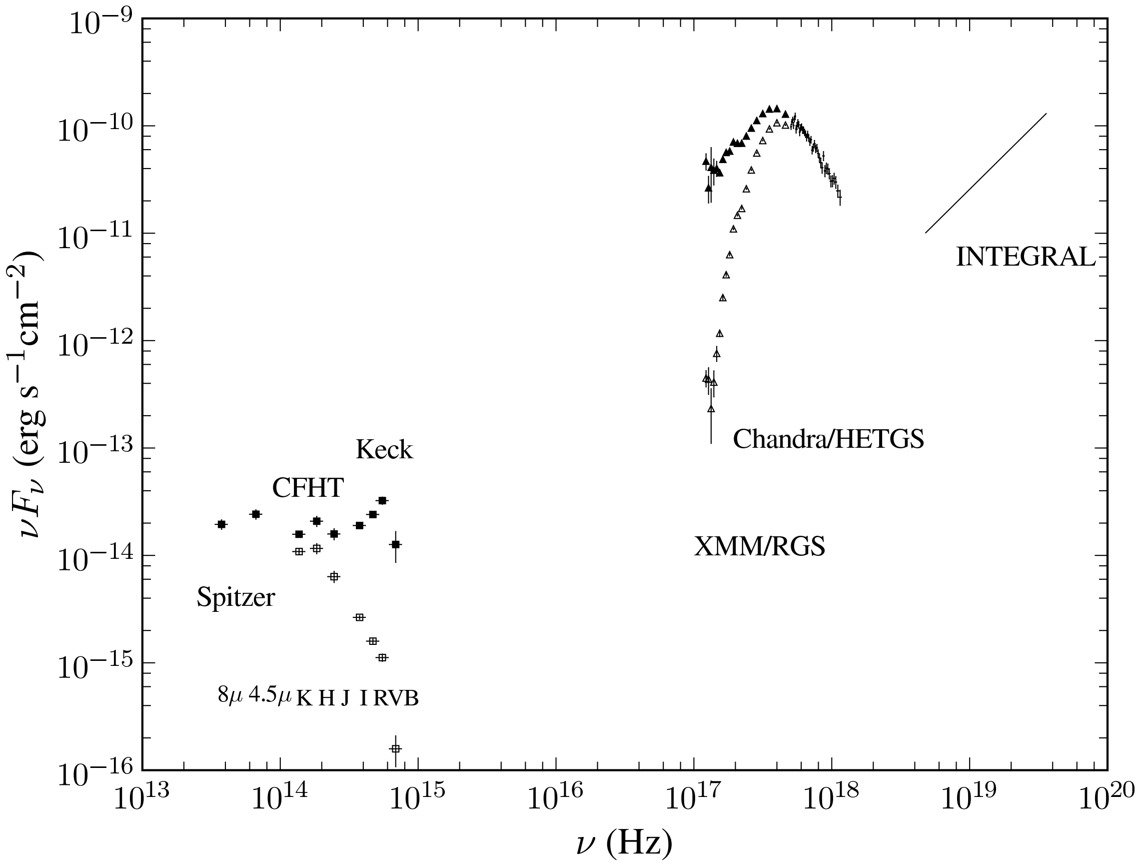

Figure 1.3 Spectral energy distribution of the brightest AXP, 4U 0142+61. This incorporates my own work and work by others during the progress of this thesis. Spitzer points are from Wang et al. (2006), CFHT from Chapter 4 (Durant & van Kerkwijk, 2006d), XMM spectrum from Chapter 5 (Durant & van Kerkwijk, 2006a), Chandra spectrum from Juett et al. (2002), and INTEGRAL spectral fit from den Hartog et al. (2006). Open symbols are observed fluxes, with corresponding closed symbols corrected for extinction with $A_V = 3.5$, from Chapter 5 (Durant & van Kerkwijk, 2006a). These measurements were not simultaneous.

1.7 Thesis Summary

The AXPs are an intriguing group of highly energetic, highly magnetic objects with fascinatingly varied and not yet understood behaviour. In order to disentangle the physical processes going on and gather tangible information, first the phenomenology must be characterised. Do the AXPs all have optical and infrared counterparts sharing the properties of 4U 0142+61? Is there variability in all wave-bands and do these correlate to one-another? Can the intrinsic spectra be extracted in the presence of high extinction? What are the luminosities of the AXPs? These questions will all be addressed in the following chapters, and the implications considered in light of the magnetar theory.

Here follows a brief summary of the rest of this thesis. In Chapter 2, I present the detection of the IR counterpart to AXP 1E 1048.1−5739 after its dramatic dimming. This raises questions of reddening, variability in multiple wavebands and the similarities between sources – themes I probe deeper in the rest of my work. In Chapter 3, I search for further optical and infrared counterparts of AXPs. I find two counterparts, but do not succeed in the third case, due to extreme crowding in the field. I investigate variability in X-rays, optical, and infrared for the best-studied AXP, 4U0142+61, in Chapter 4. In Chapter 5, I investigate the problem of extinction and the derivation of intrinsic X-ray spectra. I use high-resolution X-ray spectroscopy to measure interstellar column densities of individual elements for each AXP in a model independent way, and thus derive intrinsic spectra. These estimates of the amount of interstellar extinction are used in conjunction with the novel *red clump* technique to determine distances in Chapter 6. This technique uses field giant stars to calculate the function of reddening versus distance along a line of sight.

By the end of this work, the infrared and optical counterparts of all of the AXPs will have been investigated, variability will have been extensively described, the spectral energy distributions of AXPs will be better characterised through the measurement of extinctions, and the intrinsic luminosities and thermal emitting area will be calculated through the measurement of distances.

Chapter 2

The Broad-Band Spectrum and Infrared Variability of the Magnetar AXP 1E 1048.1−5937 [1]

2.1 Abstract

We present photometry of the Anomalous X-ray pulsar 1E 1048.1−5937 in the infrared and optical, taken at Magellan and the VLT. The object is detected in the I, J and K_s bands under excellent conditions. We find that the source has varied greatly in its infrared brightness and present these new magnitudes. No correlation is found between the infrared flux and spin-down rate, but the infrared flux and X-ray flux may be anti-correlated. Assuming nominal reddening values, the resultant spectral energy distribution is found to be inconsistent with the only other AXP SED available (for 4U 0142+61). We consider the effect of the uncertainty in the reddening to the source on its SED. We find that although both the X-ray and infrared fluxes have varied greatly for this source, the most recent flux ratio is remarkably consistent with what is is found for other AXPs. Finally, we discuss the implications of our findings in the context of the magnetar model.

2.2 Introduction

Over the last decade or so, evidence has been mounting for the existence of a class of neutron stars called the *magnetars* (Thompson & Duncan, 1996). They have enormous external magnetic fields of order $\sim 10^{14}\,$G (and even larger internal field), the decay of which powers luminous high energy radiation. Examples of this type of astrophysical source are the Soft Gamma-ray Repeaters (SGRs), which give sporadic bursts of hard X-ray/soft gamma rays as well as rare, very luminous ($\sim 10^{44}\,$erg) "giant flares"; and the Anomalous X-ray Pulsars (AXPs), so called because their luminosity far exceeds the spin-down value, and no binary companion is seen. This implies that the source of power cannot be rotational energy and that accretion is excluded. Both the SGRs and AXPs have spin periods of order $P = 10\,$s and derivatives $\dot{P} = -10^{-10} \ldots - 10^{-12}$, and are inferred to be young from their energetics and spin-down, and from supernova remnant associations in some cases. The two groups

[1] Published as Durant & van Kerkwijk, 2005, ApJ, 627, 376.

have been linked by the discovery of persistent emission from SGRs that is similar to the AXPs and bursting behaviour in the AXPs. See Woods & Thompson (2004) for a review.

It is with the discovery of optical and infrared counterparts (Hulleman et al. 2000) that models for AXPs other than the magnetar became untenable. Hulleman et al. (2004) were the first to produce a spectral energy distribution for the AXP 4U 0142+61, showing an intriguing hint of a spectral feature: a sharp break in the optical. Furthermore, Kern & Martin (2002) discovered, optical pulsations with pulsed fraction of the order 25%, modulated at the X-ray period.

Although in the magnetar model all the details are not yet ironed out, it does explain how such emission can arise from cyclotron emission by ions in the outer magnetosphere (Thompson, 2004, priv. comm.; Thompson, Lyutikov & Kulkarni, 2002). From the magnetar theory, it is not entirely clear whether one would expect the X-ray and infrared fluxes to be correlated. Such a relationship has been seen for the AXP 1E 2259+586, which has recently been shown to have correlated X-ray and infrared fluxes following an X-ray bursting episode (Tam et al., 2004). The return to the quiescent flux was found to occur on the same time-scales in both bands, and the flux ratio to remain roughly constant throughout the active episode.

1E 1048.1−5937, is a 6.4 s AXP in the field of the Carina Nebula, one of the two AXPs to have shown SGR-like outbursts to date and also the most noisy in terms of its timing characteristics (Kaspi et al., 2001; Gavriil, Kaspi & Woods, 2002). This, as well as its relatively hard spectrum, make it the most SGR-like of the AXPs (Woods & Thompson, 2004). A possible infrared counterpart to 1E 1048.1−5937 was observed by Wang & Chakrabarty (2002; henceforth WC02), who found the magnitudes: $J = 21.7(3)$, $H = 20.8(3)$ and $K_S = 19.4(3)$. Intriguingly, the source was not detected by Israel et al. (2002) down to limits of $J \sim 23$, $H \sim 21.5$ and $K_S \sim 20.7$. Ergo the object is highly variable, and therefore of particular interest.

Here we present further deep photometry in both the optical and the infrared, showing detections in three bands at levels far fainter than those of WC02, but consistent with Israel et al.'s limits. It may be that WC02 observed the object in a state similar to 1E 2259+586 in which its infrared flux was enhanced because of a preceding outburst. If so, this work probably shows the spectral energy distribution of the object in its quiescent phase.

Below, we will first present imaging observations performed at the VLT and Magellan, and describe their analyses. Next, we describe the implications of these in three main areas: the variability, spectral energy distribution, and X-ray to infrared flux ratio. We conclude with a brief discussion.

2.3 Observations and Analysis

Infrared imaging (J, H and K_s bands) was performed of the field of AXP 1E 1048.1−5937 using ISAAC at the VLT. At Magellan, further imaging data were taken both in the optical (I, z' and a wide 'VR' filter) and infrared (J and K_s) using MagIC and PANIC, respectively. See Table 2.1 for a list of observations and the conditions for each, and Figure 2.1 for images of each of the detections.

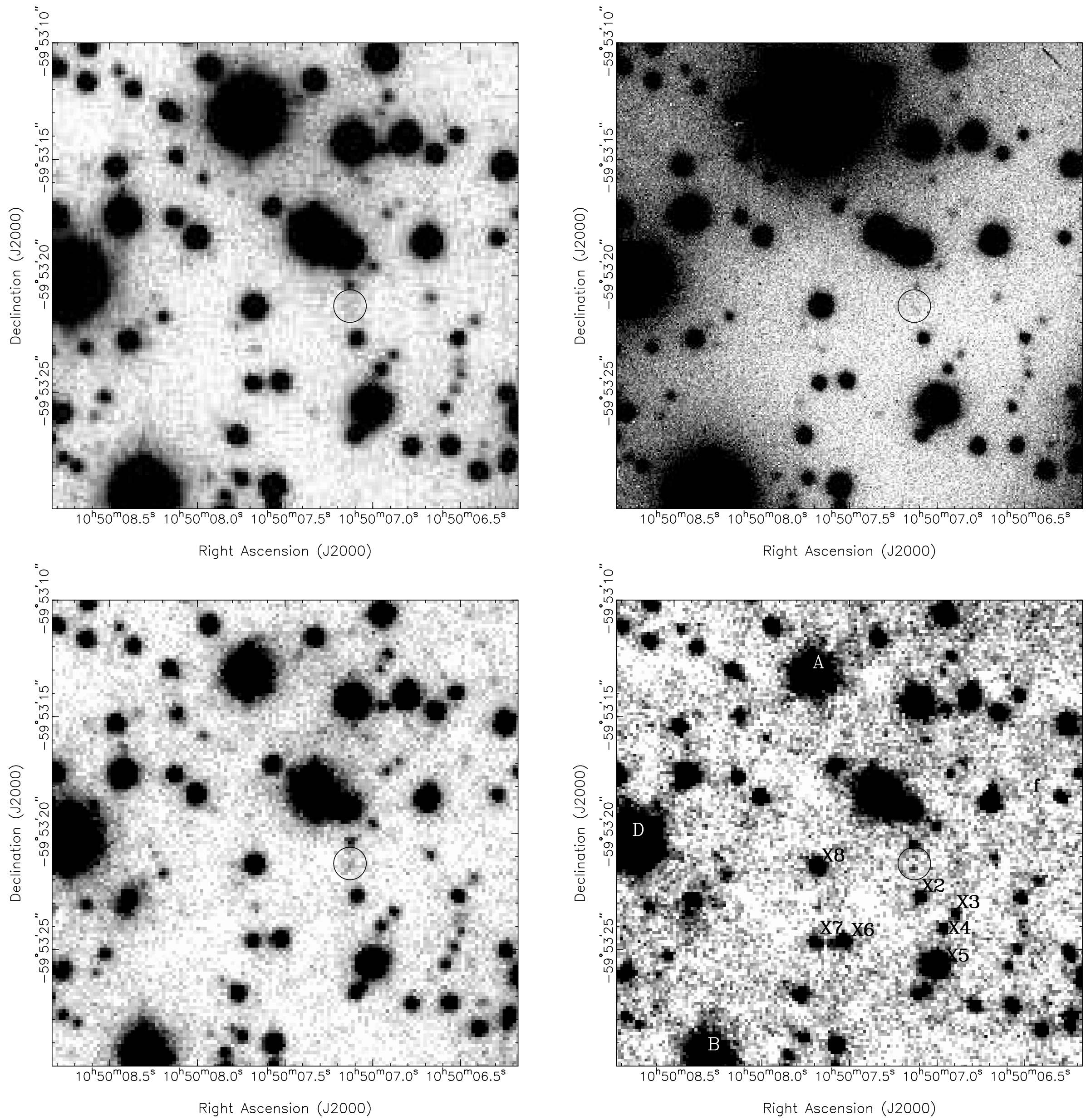

Figure 2.1 Images of the field of 1E 1048.1−5937, in all bands with detections: J-band (top left), I-band (top right) and the K_s-band (bottom) centred on the position of the AXP. The left-hand images were taken with the VLT and the right-hand ones with Magellan. The $0.74''$ radius error circle is shown on each image. Note that the horizontal band-like structure in the Magellan K_s image is due to a irreproducible "pattern noise" that existed on the PANIC instrument at the time (see text).

Table 2.1. Observation log of 1E 1048.1−5937.

Date	Telescope, instrument	Mid-exposure (UT)	Band	Integration time (s)	Seeing [a] (arcsec)	Magnitude	νF_ν (erg s^{-1} cm^{-2})
24 April 2003	VLT	01:40[b]	K_s	2772	0.34	21.3(3)	$2.6(9) \times 10^{-15}$
	ISAAC	01:45[b]	H	1848	0.47	>21.3	$< 5.6 \times 10^{-15}$
		02:15	J	3255	0.43	23.4(4)	$1.6(8) \times 10^{-15}$
6 June 2003	Magellan	03:50	I	7200	0.33	26.2(4)	$3.0(13) \times 10^{-16}$
	MagIC	05:35	VR	2700	0.45	>26.0[c]	$< 6.8 \times 10^{-16}$
		06:30	z′	2700	0.44	>24.2[d]	$< 3.0 \times 10^{-15}$
7 June 2003	Magellan	03:30	K_s	2300	0.38	>20.9	$< 3.8 \times 10^{-15}$
	PANIC	06:00	H	3780	0.34	>20.8	$< 9.0 \times 10^{-15}$
		05:00	K_s	1375	0.30	21.5(4)	$2.2(10) \times 10^{-15}$

Note. — Limits are at 95% confidence levels.

[a]Full width at half maximum.

[b]The VLT images were taken alternating between the filters, hence the close mid-exposure times.

[c]This is on a Vega-like magnitude scale, with $F_\nu(VR = 0) = 3.33(2) \times 10^{-20}$ erg s^{-1} cm^{-2} Hz^{-1} (see text).

[d]This magnitude is not on the Vega, but on the AB-system (see text).

2.3.1 Astrometry

The images below were referenced to the International Celestial Reference System through identifying stars in the USNO B1.0 catalogue on a short (30s) I-band image. Sixty-five stars were cross-identified, and a solution found with RMS deviations $\sim 0.3''$ in each coordinate (after rejecting objects with residuals greater than $0.6''$, leaving 49 good matches), and thus an astrometric error of $0.3/\sqrt{49} = 0.04''$ in connecting to the USNO reference frame. This in turn has a systematic uncertainty of $0.2''$ (Monet et al. 2003) in connecting to the ICRS. Thus the total uncertainty in astrometry is $\sim 0.2''$ in each coordinate.

The uncertainties in connecting the coordinates of the short I-band exposure to the rest of the frames are negligible in comparison with the above errors. The $0.6''$ error radius, at 90% confidence, in the *Chandra* position of 1E 1048.1−5937 (Zombeck et al., 1995; WC02) combined in quadrature with the astrometric error above, corresponds to an error of $\sim 0.74''$ on any of the images in Figure 2.1.

2.3.2 VLT/ISAAC

On the night of 23 April 2003, infrared images of the field of 1E 1048.1−5937 were taken with ISAAC (Infrared Spectrometer And Array Camera; Moorwood, 1998) on Antu, unit telescope 1 of the Very Large Telescope. We used the Long Wavelength (LW) arm with the Aladdin 1k×1k InSb infrared array, with pixel size $0.148''$. Seeing conditions were excellent. See Table 2.1 for a list of integration times and seeing for each image. The source was detected in the long J- and K_s-, but not in the shorter H-band observations.

Standard reduction was carried out in order to subtract the dark current, flat field (using median averages derived from the science frames) and combine the frames using `IRAF`. Photometry was performed using `DAOPHOT II` (Stetson, 1987).

In order to calibrate the frames, aperture photometry was performed on short-exposure images of three standard stars obtained on the same night. The aperture size was set large enough to include the majority of the flux from the star, as the sky noise was negligible in comparison; this established the magnitude zero point for each of the frames. The airmass of these exposures was in every case within 0.1 of the science exposures, so an atmospheric extinction correction was not necessary. Colour terms were negligible. In order to find the magnitude of the stars in the science field, the aperture correction was calculated using the difference between the magnitudes produced by the `allstar` task and those derived using the same large aperture used for the standards for several bright, relatively isolated stars in the frame (after the removal of fainter neighbours). See Table 2.2 for a list of the magnitudes of field stars around the AXP, with the numbering scheme as in WC02.

The errors on measurements, and also the limiting magnitudes where the source was not detected, were determined empirically. A routine was run which inserted stars of known magnitude (scaled from the PSF) into areas of the image free of stars, and then the new image was passed through the same analysis procedure as for the science frame and the standard deviation of the measured magnitudes was calculated for the inserted stars. The latter is used as the measurement error for that known magnitude. It incorporates the fact that fainter stars will be spread over a wider magnitude range as measured, and that near the magnitude limit the faintest stars will not be measured at all. The method gets around any assumptions of the flat field accuracy or profile errors, which are assumed constant parameters in the error model used by `DAOPHOT`. Whilst such parameters could be fitted for each image in turn, and then used to determine the errors, we found that in every case the function of error versus magnitude found by `DAOPHOT` deviated both from our standard deviations and from photon noise whatever the choice of flat-field and profile error. This turned out to be significant at the very bright end and near the magnitude limit.

We find, in the manner described above, the following magnitudes for the star X1, the AXP counterpart: $H > 21.3$, $J = 23.4(4)$, $K_S = 21.3(3)$. The limit in H corresponds to 95% confidence.

2.3.3 Magellan/PANIC

On the night of 6 June 2003, PANIC (Persson's Auxilliary Nasmyth Infrared Camera; Martini et al., 2004), the 1k×1k infrared imaging array with 0.125″ pixels on the Magellan Clay Telescope [2], was used to acquire images of the field of 1E 1048.1−5937 in the H- and K_s-bands under good conditions. Two separate imaging runs were performed in the K_s-band through the night, resulting in two images for analysis. The AXP was detected in only one of the K_s frames and not at all in H; see table 2.1.

There was a roughly periodic pattern noise in the PANIC detector at this time. This noise was not reproducible, and its effect can be seen in our final processed images in Figure 2.1 as a band-like variation in the brightness of the sky.

The images were processed and analysed as above, unsing three standard stars. We find the following magnitudes for the AXP: $K_S = 21.5(4)$, $K_S > 20.9$, and $H > 20.8$.

2.3.4 Magellan/MagIC

On 5 June 2003, MagIC (The Raymond and Beverly Sackler Magellan Imaging Camera[3]; Shectman & Johns, 2003), a 2k×2k CCD with quad readout amplifiers and 0.069″ pixels on the Clay Telescope, Las Campanas was used to image 1E 1048.1−5937 in the I- and z′-bands. A set of images were also taken using the custom 'VR' filter installed on MagIC (a wide, roughly rectangular pass band covering much of V and R; see Jewitt, Luu & Chen, 1996). For the I band, about 90% of the integration time was at excellent seeing conditions of $< 0.4''$, whereas the average seeing was 0.44″ in VR and 0.46″ in z′; see Table 2.1. The I-band images with the brightest sky and worst seeing were excluded from the stacking process, leaving a total of integration time of 7200 s.

Again, the frames were processed and combined using `IRAF-DAOPHOT II`, with bias subtraction and trimming performed by the `ccdmagic` task provided by the observatory and flat fields again derived from the science frames (this proved more successful than screen flats). Magnitudes were calibrated using several standard stars and errors calibrated empirically as before (following the ISAAC experience above).

Seven photometric standard stars for this run were taken from the E5 field (Stetson, 2000), at an airmass close to the mean airmass of the science exposure. The I-band zero point was a simple average over the values inferred from the well exposed stars on the frame.

The source was not detected in the VR-band. For calibration of this non-standard filter, the E5 standard field was also imaged with the VR filter, and also the standard V and R

[2] see `http://www.ociw.edu/lco/magellan/instruments/PANIC/panic/`

[3] see `http://occult.mit.edu/instrumentation/magic/`

filters to check for consistency. The VR zero point and effective wavelength were deduced in the following manner: the standard stars were assumed to have power-law spectra over their V. . . R range, so that the VR magnitude would be a simple interpolation, $VR = (1-b)V + bR$, where the parameter b is to be found. Next, VR was defined to be such that the colour-term coefficient is zero: $VR = vr + z_{VR}$ (where vr is the instrumental magnitude and z_{VR} the zero point). In effect, this makes this particular VR filter the prototype for this magnitude scale. Finally, the value of b was found which minimised variance about an average value for the zero point. This minimum value was found to be $b = 0.51(7)$, yielding the values: $\lambda_{VR} = 0.592(7)\,\mu$m, $z_{VR} = 27.9(4)$ (for 1e-/s), and $F_\nu(VR = 0) = 3.33(4) \times 10^{-20}$ erg s^{-1} cm^{-2} Hz^{-1}.

The z′ band is on the magnitude AB system, and is based on a different set of standard stars for its basic calibration. In order to find the zero point, well-known empirical transformations between z′ and the VRI bands were used (Smith et al., 2001) to find the magnitudes of each of the standard stars. These were compared with the measured magnitudes of the standard field with the z′ filter.

The AXP counterpart was found to have magnitudes $I = 26.2(4)$, $VR > 26.0$ and $z' > 24.2$.

2.4 Results and Implications

Figure 2.2 shows a colour-colour diagram for stars in the field of 1E 1048.1−5937. The AXP is clearly offset from the bulk of the stars. Its J-K$_s$ = 2.1(5) colour is similar to that found by WC02 (who found J-K= 2.3(4)), despite the fact that it is ~ 2 mag fainter, and to that of the brightest AXP, 4U 0142+61. Given the variability and peculiar colours, we believe there is no longer any doubt that the source, labelled X1 by WC02, lying at the centre of the error circle derived from *Chandra* is indeed the infrared/optical counterpart to the AXP.

We now discuss the inferred spectral energy distribution, X-ray to infrared flux ratio and variability. The spectral energy distribution and X-ray to infrared flux ratio of the AXP depend on our assumption for the amount of reddening to the source. Our knowledge on this matter is discussed in Section 2.4.2.

2.4.1 Variability

As has already been noted by Israel et al. (2002), 1E 1048.1−5937 has shown large variability in its infrared flux. The K$_s$-band magnitudes presented here are much fainter than those given in WC02, but consistent with the limits found by Israel et al. This is illustrated in Figure 2.3.

1E 1048.1−5937 is currently part of a regular monitoring programme using the Rossi X-ray Timing Explorer (RXTE), and has been observed many times over the last two years, at particularly closely spaced intervals during the time of the observations above (Gavriil & Kaspi, 2004). Marked changes are seen during this period in pulsed flux[4] and spin-down rate ($\dot\nu$). The hardness ratio shows no clear variations during this time. Figure 2.4 shows the pulsed flux and spin-down rate, with K-band photometry points as a comparison. One sees

[4]Due to nearby strong X-ray sources and the non-imaging nature of the RXTE observations, only the pulsed flux could be measured

Table 2.2. Photometry for selected stars in the field of 1E 0148.1−5937.

Star id[a]	I	J	H	K_s
X1	26.2(4)	23.4(4)	>21.5	21.3(3)
X2	23.09(2)	20.44(5)	19.51(5)	19.21(4)
X3	24.85(14)	21.7(2)	20.64(15)	20.00(8)
X4	23.54(4)	21.0(1)	20.12(9)	19.80(6)
X5	18.51(2)	16.83(2)	16.34(3)	16.28(2)
X6	22.24(2)	19.66(4)	18.67(4)	18.46(2)
X7	22.59(3)	20.21(5)	19.35(5)	19.11(3)
X8	20.61(2)	18.63(2)	18.05(3)	17.95(2)
f	22.95(3)	20.46(5)	19.61(5)	19.24(3)
A	15.59(2)	14.68(2)	14.41(3)	14.46(2)
B	16.47(2)	14.97(2)	14.65(3)	14.59(2)
C[b]	17.42(2)	15.96(2)	15.52(3)	15.54(2)
D[b]	17.11(2)	14.57(2)	13.69(3)	13.46(2)

Note. — I-band magnitudes are from the Magellan data, the rest from the VLT.

[a]As labelled in WC02. Figure 2.1 shows the locations of some of these sources within the field.

[b]There appears to have been an error in WC02, where the IR magnitudes for Stars C and D were switched (Wang, Z., 2005, priv. comm.)

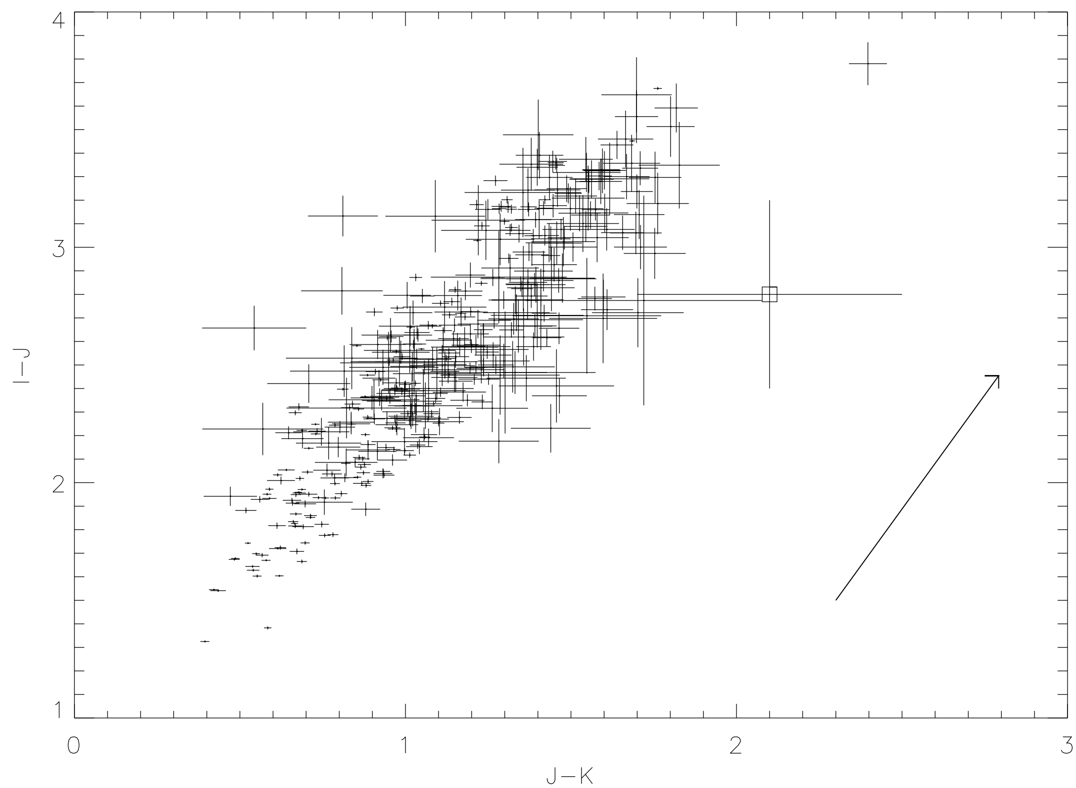

Figure 2.2 Colour-colour plot of stars in the field of 1E 1048.1−5937. The AXP (star X1) is labelled with an open square and the arrow shows the direction of increasing reddening. The outlier in the top-right is probably a genuine, highly reddened background star and a 3σ deviation; it lies far from the error circle.

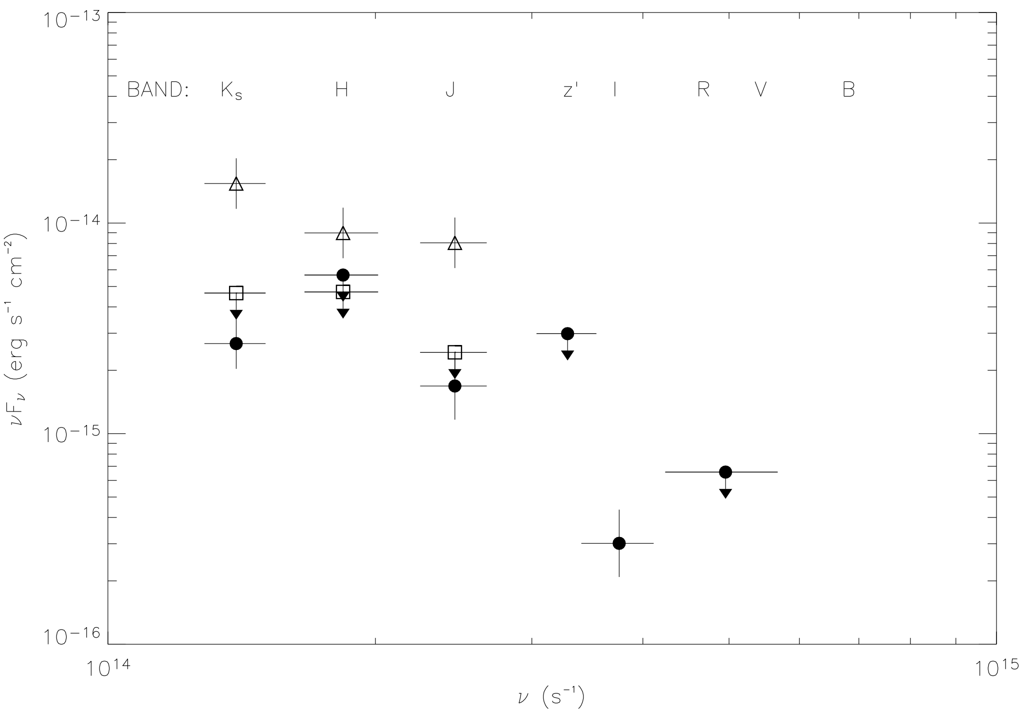

Figure 2.3 Photometry for 1E 0148.1−5937, as measured. The filled circles represent this work (where the H-, z′- and VR-band points are the respective best limits, and for K_s only the more accurate measurement, from the VLT, is shown); open triangles are those of WC02 and open squares the limits established by Israel et al. (2002).

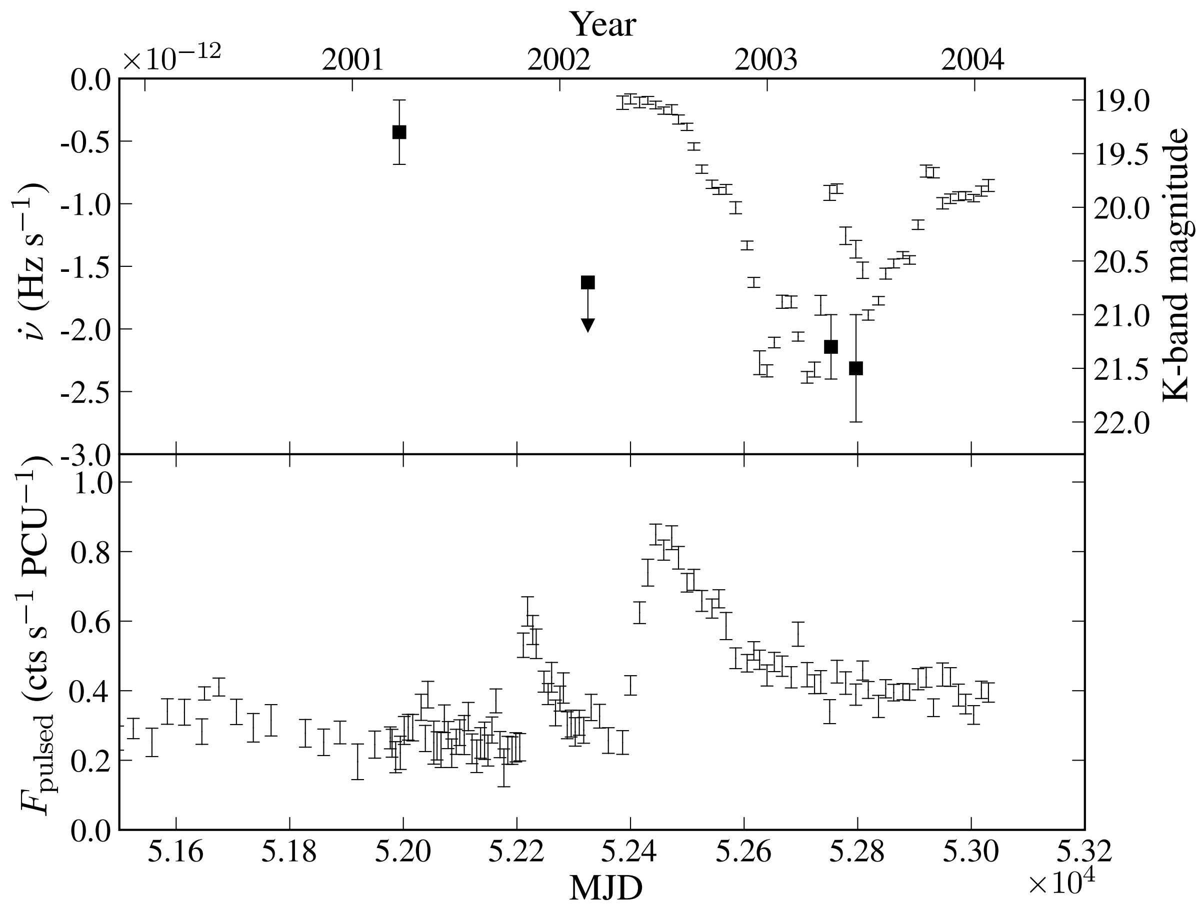

Figure 2.4 Spin-down rate, $\dot{\nu}$ (top panel, crosses), K_s-band apparent magnitude (top panel, filled squares) and pulsed flux (lower panel) as a function of time. The spin-down and flux data are taken from Gavriil & Kaspi (2004). The wide point centred at ($MJD = 51650, \dot{\nu} = -9.15 \times 10^{-13}$) represents a period in 2000 throughout which phase-connected timing was possible (Kaspi et al., 2001). At MJD$\sim$52400, the observing strategy was changed to enable spin-down measurements without long time-baseline phase coherence.

a hint of anti-correlation between the X-ray and infrared fluxes, and no obvious relationship between the infrared flux and spin-down rate. As Gavriil & Kaspi (2004) stated, X-ray flux and spin-down rate are clearly not related.

For another source also in the RXTE monitoring programme, 1E 2259+586, recent results indicate that X-ray and infrared fluxes *were* correlated in the period following multiple X-ray bursts and increased activity (Tam et al., 2004) with both spectral bands showing increased persistent fluxes, which decayed towards the pre-burst values on the same time-scale. This suggests that the mechanism at work in 1E 2259+586 is different from that of 1E 1048.1−5937, possibly because of the bursting activity (note that bursting activity cannot be excluded by the RXTE observations of 1E 1048.1−5937).

2.4.2 Distance and Reddening

The intrinsic spectrum that we derive for the AXPs depends strongly on the value that we assume for the interstellar reddening along the line of sight. Since the reddening to all of the magnetars in the plane of the Galaxy have nominal reddening $A_V \geq 5$ (which includes all of the AXPs, apart from the recently discovered CXOU J010043.1-721134, Majid et al., 2004), the extinction correction is huge and has a profound impact on the spectrum derived. As an example, the inferred optical spectrum of 4U 0142+61 changes from Rayleigh-Jeans like to flat (in νF_ν) for a change $A_V = 5$ to $A_V = 2$ (Hulleman et al., 2004). It is therefore important to consider this as part of the analysis.

Usually, the model for the intrinsic X-ray spectrum is used to infer the amount of extincting material (given as the Hydrogen column, N_H), and assuming the relationship derived by Predehl & Schmitt (1995) to calculate the reddening due to dust.

For 1E 1048.1−5937, Tiengo et al. (2002) found an apparently featureless X-ray spectrum well-fitted by an absorbed power law ($\nu F_\nu \sim \nu^{-\alpha}$, $\alpha \sim 2{-}3$) plus blackbody ($kT \simeq 0.64\,\mathrm{keV}$). This model for the X-ray spectrum yields an extremely high value for the extincting column to the source of $N_H = 1.04(8) \times 10^{22}\,\mathrm{cm}^{-2}$, comparable to values of total extinction seen through many lines of sight through the galactic plane (but see also below). In this way, values typically of order $A_V \sim 5.8$ have been arrived at (WC02) for 1E 1048.1−5937. Comparing this estimate to the typical reddening to stars in the Carina nebula ($A_V \sim 2$), Seward et al. (1986) argued that the AXP must lie behind the Carina Nebula, and thus placed a lower limit on its distance of $d \gtrsim 2.8\,\mathrm{kpc}$.

There exist other independent methods for estimating the run of reddening with distance in any given line of sight. For our field, we found the following relevant measurements.

Neckel, Klare & Sarcander (1980) measured the average function of reddening with distance, $A_V(d)$, in many galactic-plane fields including one containing this source. They find that as a function of distance, the visual extinction is constant between 1.5 kpc – 6 kpc at $A_V \simeq 1$. It should be stressed, however, that this value is an average over their field (size of order ∼square degrees), and one could argue that measurement biases would favour a lower value of extinction at any given distance in an area of highly variable dust content.

Carrero et al. (2004) performed colour-magnitude studies of three nearby open clusters in the Carina complex (approximately 1° from the region of interest). For the clusters Trumpler 16 and Trumpler 14, they find that A_V =2.0(1) and 1.8(7) and distances of d =3.9(5) and 2.5(3) respectively. This is in a region where the dust density is visibly greater than the surrounding sky; for 1E 1048.1−5937 to have a greater extinction, this suggests a more constraining lower bound on its distance. It should be noted however, that the authors of this study stress the variability of reddening from star to star in the clusters.

Finally, Merehgetti, Caravea & Bignami (1992) find that one of the brighter stars in the field is probably very highly redenned ($A_V > 7$), based on two interstellar absorption bands (4428 and 5778Å) in its spectrum. The distance to this star is unknown.

To summarise, there is reason to question our assumption that the value of N_H gained through the fitting of the X-ray spectrum gives an appropriate value of reddening; such a suggestion has also arisen in the case of the brightest of the AXPs, 4U 0142+61. Hulleman, van Kerkwijk & Kulkarni (2004) suggest that values in the range $A_V = 2 \ldots 6$ are possible. A similar uncertainty was also suggested in the case of AXP 1E 2259+586 (from the measurements of optical filaments in its associated supernova remnant, Fesen & Hurford, 1995). As we see below, the value we use to de-redden flux measurements will alter the shape of the resultant spectrum drastically.

2.4.3 Spectral Energy Distribution

Figure 2.5 shows the inferred spectral energy distribution (SED), de-redenned using $A_V = 5.8$ (the value derived from the X-ray spectral fit). As can be seen, a line of $\nu F_\nu \simeq const$ would be consistent with these points (the H-and VR-band limits are consistent with such a hypothesis).

Also on Figure 2.5 is plotted the SED of 4U 0142+61 (Hulleman, van Kerkwijk & Kulkarni, 2004), showing the optical and infrared regions for comparison, de-redenned with the nominal value for that source of $A_V = 5.1$. The inferred SEDs of the two AXPs are clearly inconsistent (see particularly the I-band point).

It is worth noting here, following from Section 2.4.2, that the reddening to both these objects is rather uncertain. With $A_V = 5.8$, 1E 1048.1−5937 has as SED with $\nu F_\nu = \nu^\alpha$, $\alpha = 0.2(4)$. This changes to $\alpha = -1.3(4)$ for $A_V \sim 2$. Hulleman, van Kerkwijk & Kulkarni (2004) suggest that for 4U 0142+61, values of reddening as low as $A_V \simeq 2$ are possible, based on the run of reddening with distance along the line of sight. Were one to take $A_V \simeq 2$ for 4U 0142+61, its SED would look much flatter and not unlike that which is shown for 1E 1048.1−5937 with $A_V = 5.8$. Thus it could indeed be that the two have similar intrinsic spectra but that the value assumed for reddening is wrong for either or both of the sources.

If we were to assume that the intrinsic spectra of the two AXPs 1E 1048.1−5937 and 4U 0142+61 are the same, then this allows us to calculate the relative reddening between the two objects, ΔA_V. This value enables a comparison between the two objects without knowledge of the specific reddening to either one. By comparing the $I - K$ colours of the two objects we find $\Delta E(I-K) = (I-K)_{1048} - (I-K)_{0142}$ =1.2(5), implying $\Delta A_V = 2.5(5)$. Thus, if the intrinsic spectra are indeed the same, 1E 1048.1−5937 would have $V = 28.2(5)$ and $R = 26.9$. These predictions can be tested.

2.4.4 X-ray to Infrared Flux Ratio

In Table 2.3 we list the currently known X-ray to infrared flux ratios of the AXPs, corrected for extinction using the nominal values of N_H derived from fits to the X-ray spectra. Note that neither the 2. . . 10 keV range nor the K-band suffer considerable extinction, so these

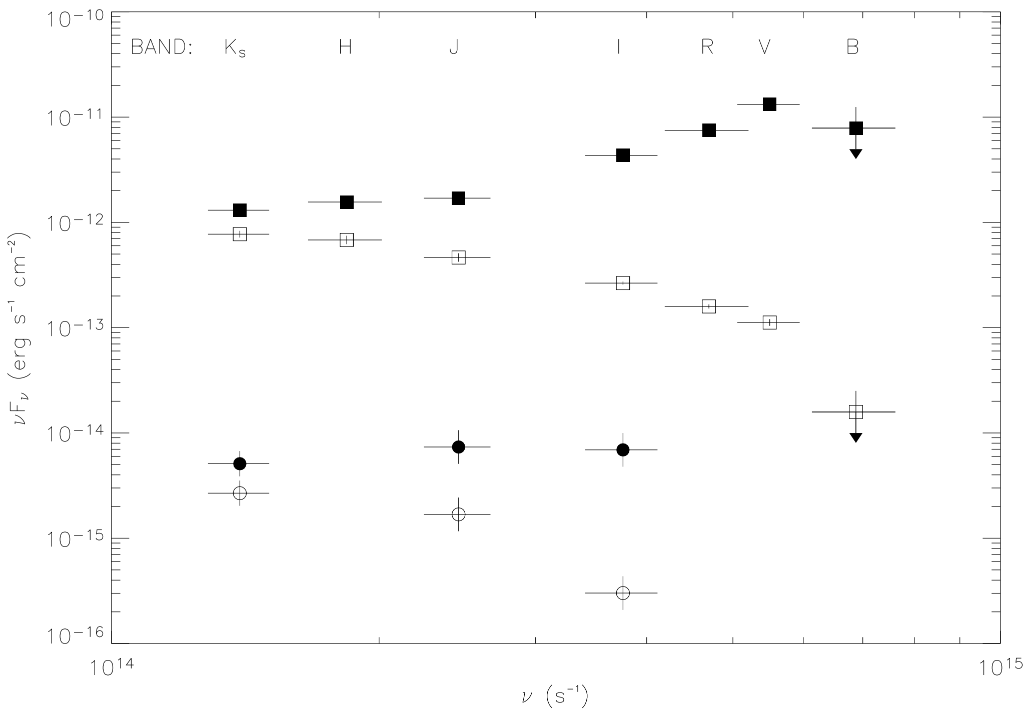

Figure 2.5 Spectral energy distribution for 1E 0148.1−5937 (circles), both as measured (open) and de-reddened with $A_V = 5.8$ (filled). Also shown is the spectral energy distribution for the brighter AXP 4U 0142+61 (squares), multiplied by a factor of 100 for clarity and de-redenned with $A_V = 5.1$ (filled squares). Only detections are shown; notice that the B-band point for 4U 0142+61 is a marginal detection. The data for 4U 0142+61 is taken from Hulleman, van Kerkwijk & Kulkarni (2004) and Israel et al.(2004).

numbers are not heavily dependent on the values of reddening chosen. However, some of the sources have shown large variability in both their X-ray and infrared fluxes, and the numbers here represent values only at some particular time.

Given the variability, the flux ratios are remarkably consistent, except for that of 1RXS J170849−4009 Interestingly, the counterpart for the latter is the least secure amongst the AXPs, as its association is based on astrometry and possible peculiar colours only (Israel et al., 2003). In fact, its inconsistency with the other sources in this table suggests that perhaps the other, fainter source within the *Chandra* error circle (named Star 'B' by these authors) could be the counterpart. The relative contributions of the sources to the J-band flux is unknown, and might account for the apparent strange colours of Star A.

1E 1048.1−5937 has varied in both its X-ray and infrared emission (see Section 2.4.1) by over a factor of 2, so the range which the flux ratio could take, when measured at some particular epoch is large. From Figure 2.4, we see that the ratio of pulsed X-ray flux to infrared flux has varied from $8 \times 10^{12} \ldots 1 \times 10^{14}$ (in units of $\mathrm{cts\,PCU^{-1}\,/\,erg\,cm^{-2}}$) . On the one hand, then, the X-ray to infrared flux ratios of AXPs are similar, and for 1E 2259+586 the X-ray and infrared fluxes were correlated following an outburst. On the other hand, the infrared and X-ray fluxes of 1E 1048.1−5937 seem, if anything, to be anti-correlated. These two statements appear hard to reconcile with one-another.

2.5 Discussion

In this work, we have detected the likely quiescent counterpart to the AXP 1E 1048.1−5937. To summarise our findings, we have found large ($\sim$2 mag) variations in the infrared brightness of 1E 1048.1−5937 which suggest a possible anti-correlation with X-ray flux, but no clear relationship with spin-down rate. This variability is the largest that has been seen in the AXPs, but variability is not unique to this source. The anti-correlation between infrared and X-ray flux is opposite to the behaviour of 1E 2259+586, where a positive correlation was found (Tam et al., 2004).

The infrared spectrum has remained of a consistent shape with WC02. We find that the inferred spectral energy distribution of 1E 1048.1−5937 is inconsistent with that inferred for 4U 0142+61, but that they can be made consistent with an appropriate choice of relative reddening (for which there may be justification). We find that although both the infrared and X-ray for this source vary a large amount and are not correlated, that the X-ray to infrared flux ratio is consistent with the other AXPs. Perhaps this challenges our understanding of whether the AXPs do indeed have quiescent periods, and of the time-scales on which the magnetosphere reacts to internal magnetic changes. We now discuss what relationships might be expected from the magnetar model.

The model proposed for how infrared and optical emission might arise from a magnetar is as follows. The decay of the internal magnetic field of the magnetar induces a twist in the magnetosphere of the magnetar. This large-scale twist is supported by global, persistent currents, which exist out to large radii. These currents power the non-thermal X-ray and gamma-ray luminosity, and may also produce infrared and optical emission, through ion cyclotron radiation at large radii (Thompson, Lyutikov & Kulkarni, 2002).

In the case that the infrared radiation is indeed cyclotron emission by ions gyrating in the outer magnetosphere, the infrared flux and torque should be correlated because of the

Table 2.3. Comparison of the un-absorbed X-ray flux and infrared flux for all Anomalous X-ray Pulsars with infrared counterparts.

AXP	X-ray flux[a] (erg s^{-1} cm^{-2})	K[b]	N_H[c] (10^{22} cm^{-2})	K-band flux[d] (erg s^{-1} cm^{-2})	F_X/F_K /1000
1E 1048.1−5937	1.4×10^{-11}	21.3	1.0	5.1×10^{-15}	2.7
4U 0142+61	8.3×10^{-11}	20.1	0.91	1.4×10^{-14}	5.9
1RXS J170849−400910	6.4×10^{-11}	18.3	1.4	9.7×10^{-14}	0.66[e]
1E 2259+586	2.0×10^{-11}	21.7	1.1	3.5×10^{-15}	5.7
XTE J1810−197	2.2×10^{-11}	20.8	1.1	8.1×10^{-15}	2.7

Note. — Data from Woods & Thompson (2004) and references therein. The values are not thought to be within active periods.

[a]Un-absorbed flux in the 2-10keV range.

[b]Apparent K_s magnitude.

[c]Inferred from fits to the X-ray spectrum.

[d]νF_ν, de-redenned assuming $A_V = N_H/1.79 \times 10^{21}$ (Predehl & Schmitt, 1995).

[e]This number is for the first suggested counterpart, Star A in Israel et al. (2003). In §3.3, we argue that Star B is more likely the counterpart, which would give a flux ratio 2.3-2.9×10^3 for the different measures of K-band flux.

following argument. First, the number of ions travelling to large enough radii to have Landau transition energies in the optical/infrared range is a fixed fraction of the total electric current. The total current in the magnetosphere defines the amount of twist in the global magnetic field structure (that is, the departure from a pure dipolar field), which in turn affects the rate at which the field strength falls off with radius. Since the torque is caused by the field strength at the light cylinder, it must then be correlated to the ion population at large radii and so to the infrared flux (Thompson, Lyutikov & Kulkarni, 2002).

Whether the infrared and X-ray flux are expected to be correlated depends on the details of their respective emission mechanisms. Changes in X-ray flux would be possible, for example, from internal heating, which would not directly affect the infrared emission.

In order to constrain the emission mechanism for the infrared flux, it will be important to establish whether the anti-correlation between infrared and X-ray flux is indeed real, and whether the IR flux to torque correlation can really be ruled out. It would also be interesting to look for a correlation with the flux in the strong, hard X-ray tail of the spectrum that was recently discovered by Kuiper at al. (2004). Furthermore, it would be worthwhile to seek further spectral signatures, and to find or at least constrain the reddening and distance to the various sources.

Acknowledgements: MD would like to thank Cees Bassa for help with producing astrometric figures, Fotis Gavriil for providing XTE results, Chris Thompson for discussion, the VizieR Service (provided by CDS and ESA) and Victor at Las Campanas. This work is supported by NSERC.

Chapter 3

Further Counterpart Searches

3.1 Abstract

The following three sections concern the attempt to identify other AXPs in the optical in infrared. A possible counterpart is found for CXOU J010043.1−721134 in the optical from archival WFPC2 images, based on unusual colours and probably variability. Due to crowding in the field, none of the infrared sources within the positional error circle for 1E 1841−045 can be confidently proposed as the counterpart. For 1RXS J170849.0−400910, a previous infrared counterpart had been suggested, but after re-analysis of the data, together with new photometry, a fainter infrared source seem the more likely counterpart.

3.2 Possible Optical Detection of the Anomalous X-ray Pulsar CXOU J010043.1−721134 [1]

3.2.1 Abstract

Archival Hubble Space Telescope Wide Field/Planetary Camera 2 observations of the Small Magellanic Cloud serendipitously reveal a possible counterpart to the Anomalous X-ray Pulsar CXOU J010043.1−721134. The candidate is faint, but its location and strange colours make it an interesting object. We estimate, that the probability of such a detection being due to a non-physical source is less than 1.5%. We have tried to confirm the identification with Gemini-South and Magellan, but the conditions were insufficiently favourable. If confirmed, the object will allow the first detailed studies of the optical and ultraviolet emission of magnetars.

3.2.2 Introduction

The anomalous X-ray pulsars (AXPs) are a class of neutron stars, numbering about half a dozen, which are radio-quiet, with periods of the order ~ 10s and estimated ages of 10^3 to 10^5yr. Like the soft gamma-ray repeaters, they are thought to be *magnetars*, whose emission is powered by the decay of a super-strong magnetic field ($\sim 10^{15}$G). See Woods & Thompson (2004) for a review of the known magnetars and their properties.

[1] Published as Durant & van Kerkwijk, 2005b, ApJ, 628, L135.

While energetically, the emission at X-ray energies dominates, optical and infrared photometry of AXPs is giving interesting constraints on the physical processes of the stellar magnetospheres. Particularly intriguing is that for the brightest object, 4U 0142+61, the optical spectral energy distribution is not just a power law. It shows, unique among neutron stars, a spectral break between V and B (Hulleman et al., 2004). Unfortunately, because of the uncertainty in the high amount of reddening, the precise shape cannot be measured.

In the magnetar model, the optical emission could be dues to ion cyclotron emission. If so, the spectral break should be a general feature (C. Thompson, 2004, priv comm.) due to the existence of a *cooling radius* in the magnetar magnetosphere from within which ions do not radiate (for a brief discussion, see Hulleman et al., 2004). The ~ 5 other AXPs known so far are, unfortunately, too highly reddened to be detected in V or B. Another prediction is that the spectra of different AXPs should be similar, but again uncertainties in the reddening do not allow us to test this (e.g. Durant & van Kerkwijk, 2005a). As an alternative model, Eichler et al. (2002), considered the possibility of coherent optical and infrared emission from the lower magnetosphere of a magnetar, in analogy to some radio pulsar models. Unfortunately, no clear predictions for the spectral shape were made.

For the purposes of investigating the optical spectra of AXPs, the recent discovery of an AXP in the Small Magellanic Cloud (SMC), CXOU J010043.1−721134 (Lamb et al., 2002; Majid et al., 2004) is particularly interesting. It is the only AXP found so far, that is not confined to the disc of the Milky Way. The reddening to this source is, therefore, much less than for the other AXPs. Furthermore, its distance is relatively well known at 60.6(1.0) kpc (e.g. Hilditch et al., 2005). It thus presents a unique opportunity to study an AXP in the blue/UV.

3.2.3 Archival Observation and Analysis

Seeking imaging data on CXOU J010043.1−721134, we searched all the archives available to us. We found that the field was observed on 20 April 2004 with the Wide Field and Planetary Camera 2 (WFPC2) on board the Hubble Space Telescope (HST), as part of a snapshot programme for three-colour photometry of several patches of the SMC (Tolstoy, 1999). Single exposures were taken of 230s in the near-ultraviolet F300W, 180s in the "broad V" F606W and 300s in Cousins I-like F814W filters. The position of our object of interest is on chip WF2 of the WFPC2 array.

We determined an astrometric solution by matching sources off the WF2 image to objects in the USNO B1.0 catalogue (Monet et al., 2003), and fitting for offset, rotation and scale. Eight stars were matched, after rejecting 7 objects which had poorly measured positions or which corresponded to multiple sources on the WF2 image. With these eight sources, the uncertainty in the astrometric fit is $0\farcs19/\sqrt{6} = 0\farcs08$ in each co-ordinate for the F606W frame. The uncertainty in applying the astrometry to the other two bands was negligible in comparison. The systematic uncertainty in connecting the USNO astrometry to the International Celestial Reference System is $0\farcs2$ in each co-ordinate, and the uncertainty in the *Chandra* position of CXOU J010043.1−721134 is a radius $r = 0\farcs6$ at 90% confidence. Note that the latter is from the nominal *Chandra* performance, despite being somewhat off-axis (Lamb et al., 2002). The above numbers, combined in quadrature, give a total uncertainty in the AXP's position on our images of $r = 0\farcs72$ at 90% confidence. Photometry was performed using `HSTphot 1.1` (Dolphin, 2000).

Table 3.1. Astrometry and photometry of stars near CXOU J010043.1−721134

Star	R.A.$_{J2000}$	Dec$_{J2000}$	m_{300}	m_{606}	m_{814}	$m_{606} - m_{814}$	M_V[a]
X[b]	01:00:43.109	-72:11:33.77	> 21.7	24.19(15)	> 24.5	< -0.3	5.0
Y	01:00:43.187	-72:11:34.14	> 21.7	24.40(15)	23.61(14)	0.8(2)	5.2
Z	01:00:42.990	-72:11:33.01	16.295(8)	17.915(4)	18.022(7)	-0.107(8)	-2.9

Note. — Limits are at the 3σ level.

[a]Calculated using $(m - M)_0 = 18.9$ and $A_V = 0.3$ (Hilditch et al., 2004) and assuming $m_{606} \simeq V$

[b]Proposed counterpart to CXOU J010043.1−721134, which has position $R.A. = 01:00:43.14$, $dec = -72:11:33.8$

Figure 3.1 shows the F606W image of the field immediately around CXOU J010043.1−721134, with the positional error circle indicated. Stars X and Y have positions consistent with that of the AXP, with Star Z being a nearby, much brighter source. Their positions and magnitudes are listed in Table 3.1, and indicated in a colour-magnitude diagram of all stars detected in the WFPC2 images in Figure 3.2.

From the photometry, Star Y is consistent with being a G5V star at the distance and reddening of the SMC, and Star Z an early B-type star. The colours and magnitudes of Star X do not correspond to any known stellar type, and make it a clear out-lier in Figure 3.2, suggesting a very blue, possibly hot object. Based on its position and unusual colours, we therefore consider Star X a likely counterpart to CXOU J010043.1−721134.

As a caveat, however , it should be remembered that this measurement is based on a single F606W exposure. The source in Figure 3.1 does not appear like a cosmic ray hit, and the `HSTphot` χ and *Sharp* parameters are within reasonable limits for a point source: $\chi = 1.18$ (goodness of fit parameter; reasonable values: < 2.5) and $Sharp = -0.425$ (where 0 corresponds to a stellar point spread function, positive values to more peaked profiles and negative values to more diffuse ones; reasonable values: -0.5– 0.5). There were no bad pixels within Star X's profile.

In order to test the robustness of this identification, we estimated the likelihood of such a detection in an error circle of this size at any point on this chip of the detector. We searched the photometry for all objects in the F606W image which are classified as stellar ($\chi < 2.5$, $-0.5 < sharp < 0.5$), and with $m_{606} - m_{814} < -0.3$, i.e. at least as blue as Star X. Forty such objects are found on the same chip as Star X (including those near Star X in Figure 3.2), giving the probability of one falling within a circle of radius $0\farcs72$ of $\approx 1.5\%$. We note that the majority of these are within 3 pixels of brighter sources in the F814W image, and consequently were not detected in that band. Since this does not apply to Star X, and there

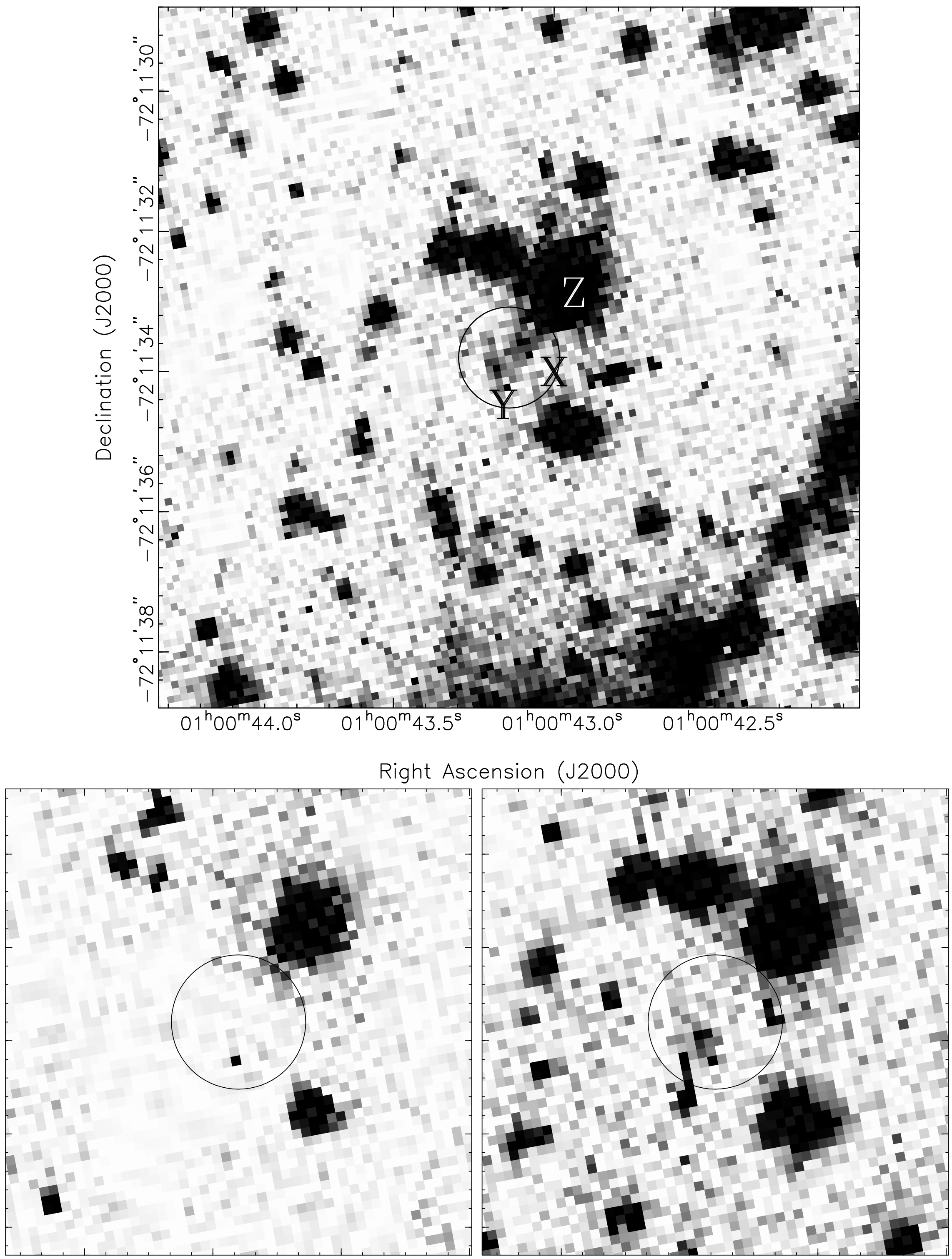

Figure 3.1 WFPC2 images of the field of CXOU J010043.1−721134, in F606W (top), F300W (bottom left) and F814W (bottom right). Star X is the proposed counterpart, and Stars Y and Z its nearest neighbours. The circle shows the uncertainty in the Chandra position at 90% confidence.

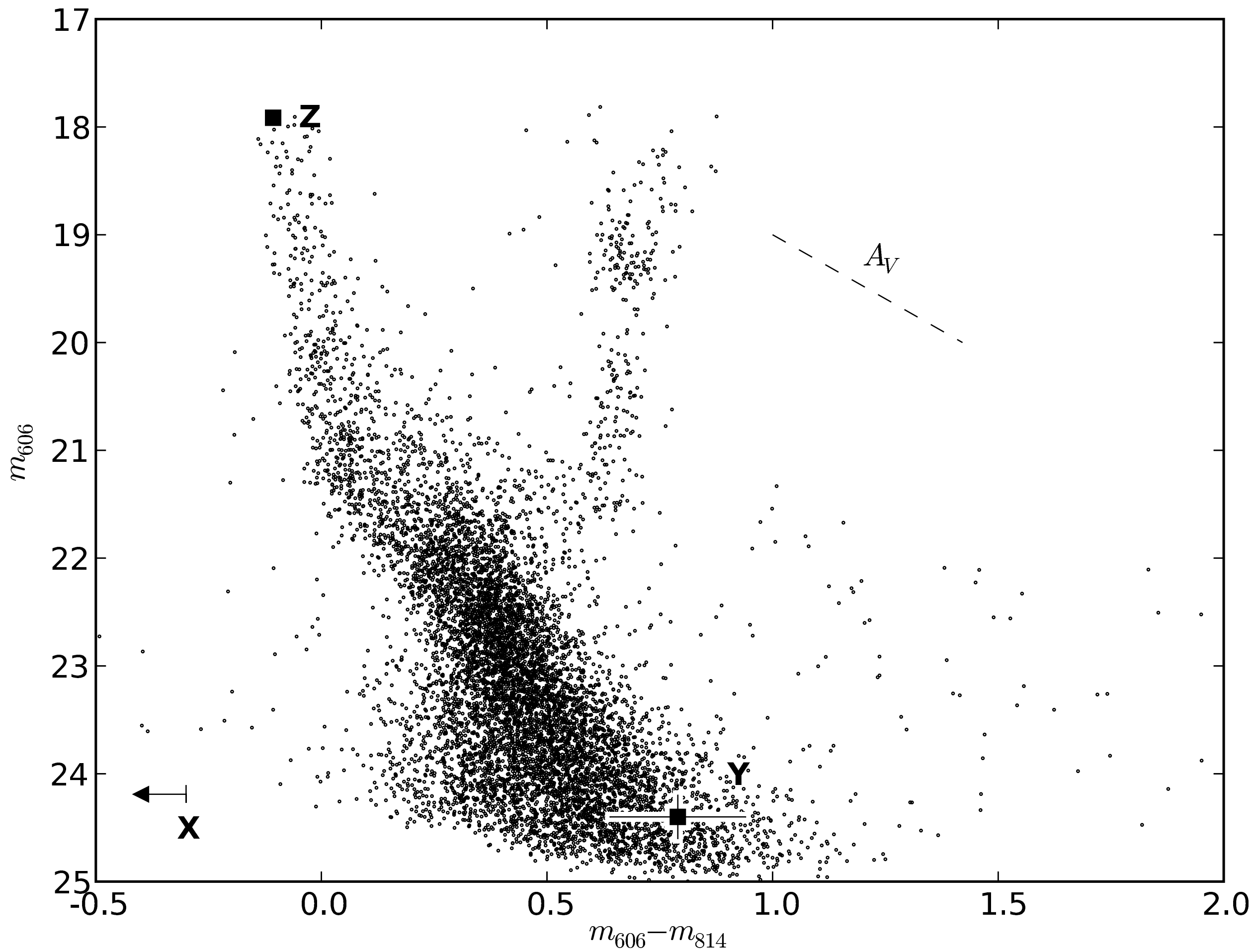

Figure 3.2 Colour-magnitude diagram of the field around CXOU J010043.1−721134. Stars Y and Z are labelled, and Star X is shown as a limit. The effect of one magnitude of visual reddening is shown by the dashed line.

do not appear to be any artifacts close to it (i.e. the location of Star X appears like sky in the F814W image), the chance of it being a false detection is somewhat smaller, but how much smaller is hard to quantify.

We also calculated the likelihood of our putative detection being due to a cosmic ray hit or instrumental effects. We searched for objects which are classified as stars in terms of their *Chi* and *Sharp* parameters as above, which were detected in F300W but not in F606W. We find thirteen objects, which implies that the probability of Star X being due to a cosmic rays hit or purely instrumental effects is 0.4% (after correcting for the difference in exposure time between F300W and F606W).

Seeking to confirm this detection, we searched other archives for optical images. We found a V-band image from the Wide Field Imager (WFI) on the 2.2m ESO telescope, La Silla, Chile. This demonstrated that the area of sky was very crowded, and extremely good seeing would be required to separate and securely detect Star X. In this case, the seeing was poor. We also obtained Gemini DDT observations with GMOS-S (Crampton & Murowinski, 2004) at Cerro Pachon, Chile. Unfortunately, the seeing was also not good enough in these images to distinguish between the sources in the crowded field. A proposal was also accepted at Magellan, Las Campanas, Chile, but conditions have not been good enough to obtain images so far. Unfortunately, the presence of Star Z means that only the most exceptional seeing conditions will allow further measurements of this object from the ground. The separation between Stars X and Y is about $0\farcs5$, and seeing better than $0\farcs6$ would be required to obtain a measure of Star X.

3.2.4 Discussion and Conclusions

Taking Star X as the true optical counterpart, CXOU J010043.1−721134 has an X-ray to optical flux ratio $F_X/F_V = 1.0 \times 10^{-13}/5.5 \times 10^{-15} = 18$ (un-absorbed X-ray flux in the 2–10keV range from Woods & Thompson, 2004; visual νF_ν flux is de-reddened using $A_V = 0.3$ [Hilditch et al., 2005], and assumes $m_{606} = V$). This compares with $F_X/F_V = 460$ for 4U 0142+61 (for $A_V = 5.1$, the nominal reddening), the only other AXP with an optical detection (Hulleman et al., 2004). Clearly the two ratios are very different.

It has been observed that infrared to X-ray flux ratios are similar for those AXPs with secure measurements (4U 0142+61, 1E 1048.1−5937 and 1E 2259+586; Durant & van Kerkwijk, 2005a). Variations have, however, been observed to be very large, of orders of magnitude in some cases. For example the *transient AXP* XTE J1810-197 (Ibrahim et al, 2004) increased dramatically in both X-rays and infrared flux before slowly dimming again.

It is possible that the difference in V-band to X-ray flux ratio above arises because the measurements for CXOU J010043.1−721134 were not simultaneous; the AXP could have been brighter by a large factor at the time of the HST observation. CXOU J010043.1−721134 was observed to be $\sim 50\%$ brighter in X-rays by Majid et al. (2004) than Lamb et al. (2002), but they attribute this to the different instruments used to make the observations rather than genuine variability. 4U 0142+61 has been the most stable of the AXPs in both X-ray and optical flux (Hulleman et al., 2004). This could, in principle, mean that the intrinsic spectra of the two objects are very different, possibly indicating differing magnetic field configurations.

The limit in F814W already provides some constraints on the shape of the optical spectrum. Whilst a Rayleigh-Jeans form $\nu F_\nu \sim \nu^n$, $n = 3$ is possible, a flat spectrum ($n = 0$)

is excluded. The 90% confidence limit is $n \geq 2$. Since the spectrum should not increase steeper than Rayleigh-Jeans (in the absence of an emission feature), we predict that the I-band magnitude is not much below the limit we have established. The F300W limit is not constraining in this respect.

In summary, we present Star X, with $m_{606} = 24.19(15)$, as the probable optical counterpart to CXOU J010043.1−721134. It is at the right location and has colours unlike normal stellar sources. Although based on a detection in a single exposure, `HSTphot` diagnostics point to it being a real detection, with only a $\lesssim 1.5\%$ probability of a false detection. If confirmed, this discovery will enable the measurement of AXP properties in the blue and UV.

Acknowledgements: This work made use of archival observations made with the NASA/ESA Hubble Space Telescope and with observations from ESO Telescopes at the La Silla Observatories. We thank Slavek Rucinski and the Gemini Observatories for attempting follow-up observations. We thank an anonymous referee for very useful comments which much improved the presentation of our results. We acknowledge financial support from NSERC.

3.3 A Deep Infrared Search for AXP 1E 1841−045 [2]

3.3.1 Abstract

Multi-colour (JHK_S) imaging and photometry of the field of the Anomalous X-ray Pulsar AXP 1E 1841−045 is analysed in the light of new, accurate coordinates from *Chandra* (Wachter et al, 2004). From excellent quality images, we find multiple sources in and around the position error circle. Of these, none can be confidently identified as the infrared counterpart. The limiting magnitudes reached were $J = 22.1$, $H = 20.7$ and $K_S = 19.9$ (95% confidence).

3.3.2 Introduction

The Anomalous X-ray Pulsars (AXPs) are a small group of young, energetic neutron stars, whose luminosity is thought to be powered by the decay of a super-strong magnetic field: *magnetars* (Thompson & Duncan, 1996). Since the discovery of the first optical counterpart to an AXP (Hulleman, van Kerkwijk & Kulkarni, 2000), searches have been undertaken to identify further optical and infrared counterparts in different colours. Due to the large extinction to most of these sources, the infrared has proved the more successful route. See Woods & Thompson (2004) for a review of the AXPs and their counterparts to date.

1E 1841−045 is located within the supernova remnant Kes 73, and has a pulse period of 11.8s and a soft X-ray spectrum well-fitted by either a black-body plus power-law or the sum of two black-bodies with a fitted hydrogen absorption column of $N_H = 2.5 \times 10^{22}\mathrm{cm}^{-1}$ (Morii et al., 2003; Gotthelf et al., 2004). As a recent surprise, this source was found by Kuiper at al. (2004) to have hard, pulsed X-ray emission with a rising power-law spectrum out to about 100keV. Since this, then, dominates the emission energetics, it has prompted an ongoing revisal of magnetar electrodynamics.

The supernova remnant Kes 73, has an estimated age of ∼1500yrs (e.g. Gotthelf et al., 2002) and using H I measurements towards the SNR, its distance has been determined as 6–7.5kpc (Sanbonmatsu & Helfand, 1992). Geometric alignment and the youth of both the SNR and AXP (whose age is not easily determined, but is of the order thousand of years) point to the association of the two being real.

Mereghetti et al. (2001) were the first to search for an infrared/optical counterpart to 1E 1841−045 by performing multi-colour imaging and selected spectroscopy, but based on only *ROSAT* and *Einstein* positions.

Wachter et al. (2004) report a precise location for the AXP based on new *Chandra* observations. They give the source's coordinates as RA=18:41:19.343, Dec=-04:56:11.16, with a 3σ error radius of $0.9''$. The images presented by these authors show an object in the error circle that is either extended or made up of multiple sources.

Here we present deeper images taken in better seeing, from which we attempt to identify the infrared counterpart to 1E 1841−045.

3.3.3 Observation and analysis

We imaged the field of 1E 1841-045 on the night of 5th June 2003 with PANIC (Persson's Auxiliary Nasmyth Infrared Camera, Martini et al., 2004), the 1k×1k infrared imaging array

[2]Published as Durant, 2005, ApJ, 632, 563.

with 0.125″ pixels on the Magellan Clay Telescope[3], under excellent conditions. The total integration times were 1125s in J, 1825s in K_S, and 1825s in H, at seeing of $\simeq 0.35''$. A second J-band integration was performed, but the seeing had deteriorated, and so this is not included in the analysis.

Standard reduction was carried out to flat field and combine the frames using `IRAF`. The flat fields were derived by median combining many images in each filter of a less crowded field. This proved more successful than either screen flats or median images from the data frames themselves. Photometry was performed using `DAOPHOT II` (Stetson, 1987).

In order to calibrate the frames, short-exposure images were obtained of standard stars, from Persson et al. (1998). Because of some light cloud in patches on the night in question, it was found more reliable to use standards from the following night and find the magnitude transformation from one night to the next using fields which were imaged on both nights (see Durant & van Kerkwijk, 2005a). The offsets were small in each band, $\simeq 0.03$mag. The standards were taken at a range of airmasses, so the zero point at the appropriate airmass could be found (the variation with airmass is slight in the infrared in any case).

The magnitudes found for stars in the field tend to be fainter than those found by Wachter et al. (2004) and Mereghetti et al. (2001) by typically 0.3mag for their faintest stars (note that there are also some substantial differences in the magnitudes presented by these two sets of authors). This can be attributed to the better seeing conditions, which allowed sources to be separated which would otherwise have been blended in this extremely crowded field. Many of the stars measured by Mereghetti et al. (2001) are saturated on our deeper images, and so cannot be compared. We believe that the better separation of sources entirely explains the discrepancy in measured magnitudes.

An astrometric solution was found for the images based on 2MASS sources (Curti et al., 2003) in the field. 86 stars were matched for J in the $\simeq 2' \times 2'$ field, and after rejecting large residuals, the RMS deviation in each coordinate was $\simeq 0.1''$ with 71 points. The error in connecting this image to the others is negligible in comparison. The astrometric uncertainty is in connecting our images to the 2MASS reference frame. Since Wachter et al.'s coordinates are also based on 2MASS stars, there should be no additional uncertainty in the astrometry.

3.3.4 Results

Figure 3.3 shows the stacked images, with the position error circle of radius 0.9″ (3-σ confidence) derived by Wachter et al. (2004) overdrawn. Table 3.2 gives the magnitudes of stars in and around the circle, as labelled on the images, and Figure 3.4 shows those stars with three measured magnitudes on a colour-colour diagram compared to the rest of the stars in the field.

From Figure 3.4, one sees that, of the stars near the positional error circle (see Figure 3.3), none have significantly different colours to other stars in the field. Note that the large scatter is due to the extreme crowding in the field, particularly in K. This means that the measured magnitude of a given star can be strongly affected by the halo of a neighbouring brighter star. The magnitude limits reached at 95% confidence are: $J = 22.1$, $H = 20.7$ and $K_S = 19.9$.

By fitting the X-ray spectrum with an absorbed black body plus power-law spectrum,

[3] see `http://www.ociw.edu/lco/magellan/instruments/PANIC/panic/`

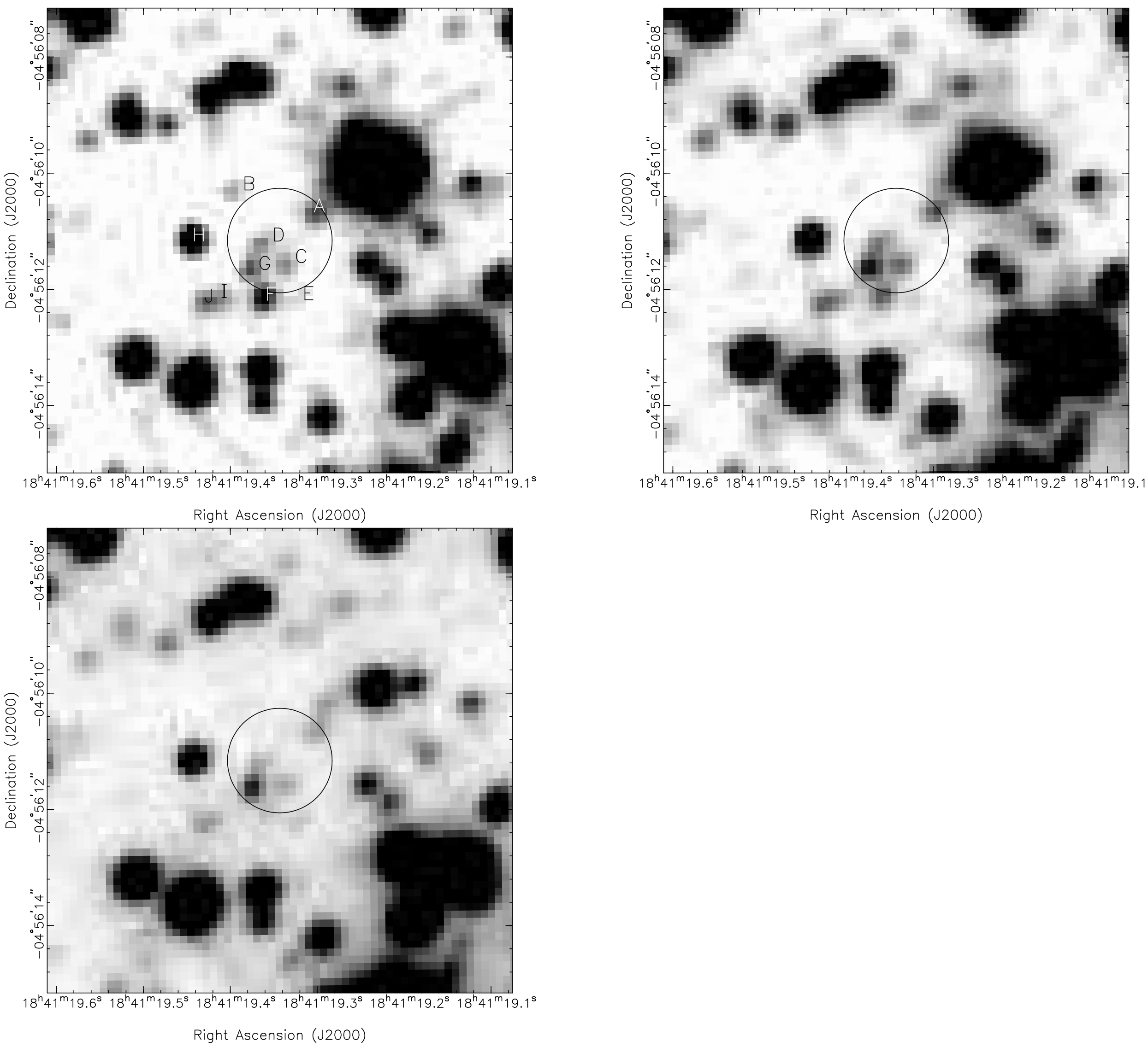

Figure 3.3 Images of the field of 1E 1841-045 in the K_S- (top-left), H- (top right) and J-bands (bottom). In the left hand image are labelled the stars whose magnitudes are presented in Table 3.2

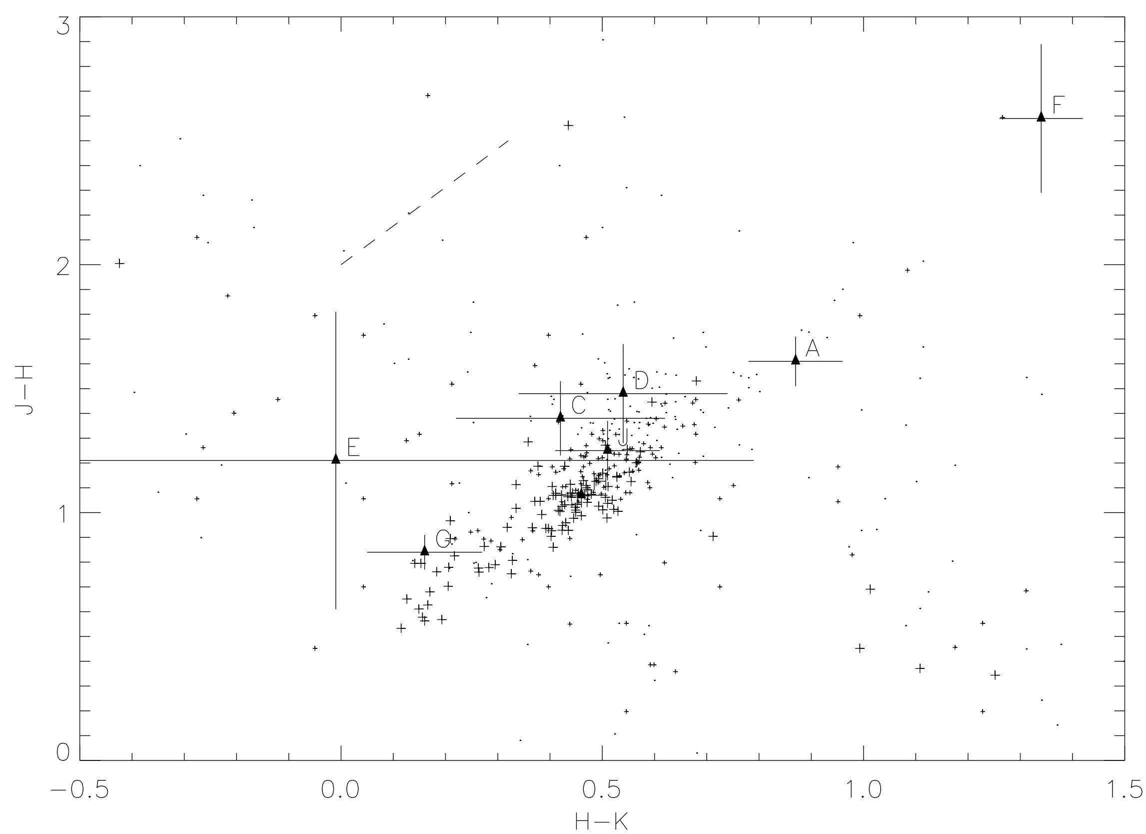

Figure 3.4 Colour-colour diagram of stars in the field of 1E 1841−045. The stars in or close to the *Chandra* error circle are labelled with letters. Only stars with magnitude errors less than 0.15 in each band are plotted (comparable to stars C and D). Bigger symbols represent stars with lower magnitude errors in all three bands. The dashed line shows the effect of five magnitudes of visual extinction. AXPs are expected to lie below the bulk of the stars in this diagram, based on 4U 0142+61 (Israel et al., 2004).

Table 3.2. Positions and magnitudes of stars within or near the *Chandra* error circle.

Star ID[a]	R. A.	Dec	J	H	K_S
A	18:41:19.293	-04:56:10.67	20.96(9)	19.35(6)	18.44(7)
B	18:41:19.388	-04:56:10.28	> 22.1	20.8(4)	19.6(2)
C	18:41:19.327	-04:56:11.57	21.28(12)	19.90(11)	19.44(18)
D	18:41:19.356	-04:56:11.23	21.38(14)	19.90(11)	19.32(15)
E	18:41:19.315	-04:56:12.20	22.2(3)	20.9(5)	20.9(6)
F	18:41:19.352	-04:56:12.15	22.1(3)	19.47(7)	18.09(5)
G	18:41:19.367	-04:56:11.64	19.93(4)	19.09(5)	18.89(9)
H	18:41:19.435	-04:56:11.13	18.97(3)	17.90(3)	17.40(4)
I	18:41:19.401	-04:56:12.15	> 22.1	20.04(13)	19.14(12)
J	18:41:19.421	-04:56:12.24	20.82(8)	19.57(8)	18.99(10)

Note. — Magnitude limits are at 95% confidence. The systematic uncertainty in position does not affect relative co-ordinates.

[a]as labelled in Figure 3.3.

a value for the hydrogen column density can be derived. Assuming the Predehl & Schmitt (1995) relationship, this translates to an extinction towards the source of $A_V \approx 14$. With the caveat that the intrinsic X-ray spectrum is not known, this number provides an approximate measure of reddening. Figure 3.4 shows that the effect of extinction means that one cannot distinguish between an intrinsically hot but highly extincted source and an intrinsically cool (i.e. red) source. Also note that, since the main sequence is known to start around (0,0) on this diagram, the bluest sources here have $A_V \approx 2$, although extinction is known to increase rapidly in this direction (e.g. Drimmel et al., 2003).

Although an out-lier on Figure 3.4, Star F is consistent with being a very highly reddened red super-giant. De-reddening it with $A_V = 14$ would not place it below the bulk of the stars, as is the case with 4U 0142+61 ($H - K_{\mathrm{S}} = 1.0(1)$, $J - H = 1.2(2)$, Israel et al., 2004, Hulleman et al., 2004). Whether these two objects would be expected to have the same spectrum is an open question, as is the appropriate value of reddening. Those AXPs with confirmed infrared counterparts appear to have similar X-ray to infrared flux ratios (Durant & van Kerkwijk, 2005a), and Star F would have both a much brighter counterpart and much lower X-ray to infrared flux ratio than 4U 0142+61. Although stars with colours as red as Star F are rare in the field, it cannot be presented as a likely counterpart. It is worth mentioning that Star B, if close to the the magnitude limit in J, would fall in the right region of Figure 3.4, but again this can hardly be more than a suggestion of a candidate counterpart.

Comparing with the spectrum of 4U 0142+61 again (the brightest and best-measured AXP, $J = 22.3(1)$, $H = 21.1(1)$, $K_{\mathrm{S}} = 20.15(8)$), one would expect 1E1841−0145's magnitudes to fall beyond the magnitude limits given above, especially if the nominal reddening values to the two sources are to be believed (which would make the magnitudes above fainter by about 2.5, 1.7 and 1.1 magnitudes respectively). Thus a non-detection here does not imply that the two spectra are necessarily different, but does demonstrate that this part of the sky is so crowded that finding the counterpart will prove very difficult.

In conclusion, we have found the magnitudes of several sources in or near the accurate *Chandra* error circle for the position of 1E 1841−045. Despite the depth and quality of the images, we find no source which can be confidently presented as the likely counterpart. Extremely deep images with narrow point-spread functions will be required in order to find the counterpart to this AXP.

3.4 The infrared counterpart to the magnetar 1RXS J170849.0−400910 [4]

3.4.1 Abstract

We have analyzed both archival and new infrared imaging observations of the field of the Anomalous X-ray Pulsar 1RXS J170849.0−400910, in search of the infrared counterpart. This field has been previously investigated, and one of the sources consistent with the position of the AXP suggested as the counterpart. We, however, find that this object is more likely a background star, while another object within the positional error circle has non-stellar colors and shows evidence for variability. These two pieces of evidence, along with a consistency argument for the X-ray-to-infrared flux ratio, point to the second source being the more likely infrared counterpart to the AXP.

3.4.2 Introduction

The anomalous X-ray pulsars (AXPs) are a class of neutron stars, numbering about half a dozen, which are radio-quiet, with periods of the order $\sim 10\,\mathrm{s}$ and estimated ages of 10^3 to 10^5 yr. Like the soft gamma-ray repeaters, they are thought to be *magnetars*, whose emission is powered by the decay of a super-strong magnetic field ($\sim 10^{15}$ G). See Woods & Thompson (2004) for a review of the known magnetars and their properties.

While energetically, the emission at X-ray energies dominates, optical and infrared photometry of AXPs is giving interesting constraints on the physical processes of the stellar magnetospheres and environment. Recently, Wang et al. (2006) identified a mid-infrared and K-band excess around a magnetar, 4U 0142+61, which they interpret as thermal emission from a passively illuminate dusty fall-back disc. It would be interesting to see whether this is a generic property of the AXPs. If so, it might explain the consistency of K-band to soft X-ray flux ratios for most of the AXPs (Durant & van Kerkwijk, 2005a).

1RXS J170849.0−400910 is a magnetar with 11s pulsations, discovered in the soft X-ray band by *ROSAT* and *ASCA* (Sugizaki et al. 1997). Recently, a hard X-ray component ($\sim 100\,\mathrm{keV}$) to its spectrum has been found, which dominates the magnetar energetics (Kuiper at al. 2006).

Israel et al. (2003) reported a tentative identification of the infrared counterpart to 1RXS J170849.0−400910, based on near-infrared H- and K-band adaptive optics observations with the Adaptive Optics Bonette (AOB) on the Canada-France-Hawaii Telescope (CFHT), and further JHK photometry from the European Southern Observatory's New Technology Telescope (ESO NTT). They found two possible faint counterparts in the positional error circle, Stars "A" and "B" separated by only $0.\!''26$ (see images below). Israel et al. suggested Star "A" was the more likely counterpart, based on its peculiar colors. Below, we present a re-analysis of their CFHT data, together with our own data and deep archival Very Large Tetescope (VLT) imaging. We first describe these datasets and our analysis methods, followed by the lines of argument which lead to our conclusion that in fact the true counterpart is Star "B".

[4] Accepted for publication in ApJ (Durant & van Kerkwijk, 2006c).

Table 3.3. List of observations.

Date	Telescope	Instrument	Filter	Exposure Time (s)	FWMH[a]
2002-08-17	CFHT	AOB/KIR	K’	60×45	0.14
			H	60×45	0.14
2003-06-06	Magellan Clay	PANIC	J	60×9	0.44
			H	60×9	0.35
			K_S	25×21	0.31
2003-06-07	Magellan Clay	PANIC	J	60×18	0.38
			H	60×9	0.4
			Y	60×9	0.36
		MagIC	I	300×15	0.44
2003-06-20	VLT-UT3	NA-CO	J	60×40	0.11
			H	10×40	0.10
			K_S	20×80	0.08

[a]Typical stellar profile size in arcsec. For AO images, measured close to the stars on interest.

3.4.3 Observation and Analysis

We analyzed observations made with Magellan/PANIC and archival observations from CFHT/AOB and VLT/NACO (see Table 3.3 and below for details). The Magellan observations provide the widest field of view, and a uniform PSF and background; they are therefore the best images to base our photometric calibration on. The CFHT and VLT observations both made use of adaptive optics (AO) in order to reduce the size of stellar PSFs and thus increase the signal to noise ratio as well as reduce the problem of blending. Unfortunately, this comes at the cost of a PSF which has a complicated shape and varies with position on the image (particularly for shorter wavelengths). We thus calibrate the AO images using Magellan as our baseline.

3.4.4 Magellan

We imaged 1RXS J170849.0−400910 in the K_SHJ bands using PANIC (Persson’s Auxilliary Nasmyth Infrared Camera; Martini et al., 2004) on the Magellan Clay Telescope, at Las Campanas, Chile. PANIC is a 1024×1024 Hawaii infrared array with $0\farcs125$ pixels.

The conditions were good to excellent, with seeing between $0\farcs30$ and $0\farcs45$ (see Table 3.3). We also obtained further imaging in the I-band using MagIC (the Raymond and Beverly Sackler Magellan Imaging Camera[5]; Schectman & Johns, 2003), but neither this nor

[5]see `http://occult.mit.edu/instrumentation/magic/`

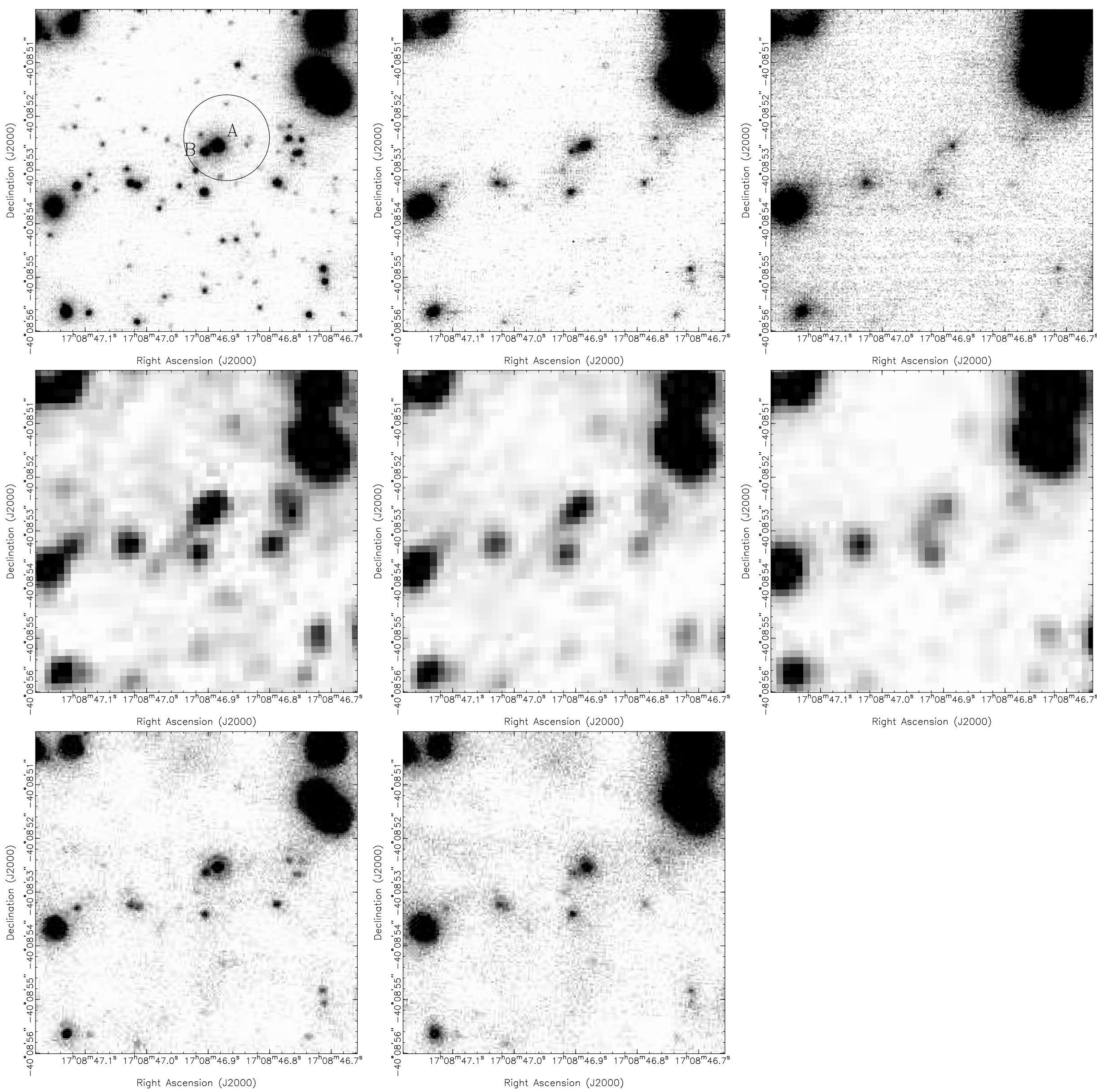

Figure 3.5 Images of the field of 1RXS J170849.0−400910, from VLT/NACO (top), Magellan/PANIC (middle) and CFHT/AOB (bottom), with KHJ from left to right. In the VLT/NACO K-band image, the 90%-confidence 0.″8-radius *Chandra* position error circle (at 90 %) is shown and the two candidate counterparts, Stars A and B are labeled.

the Y-band[6] were sufficiently deep to detect Stars A and B and are not considered further. (For completeness, we note that for the I band, where we have photometric callibration, the 95% confidence detection limit is $I > 25.1$).

We reduced the images in a standard way, by first subtracting off a dark frame from each raw image, flat-fielding using the median of the images, and then registering and combining them. For the H- and J-bands, we select the better of each of the two final images (from the 6^{th} and 7^{th}, respectively) for analysis rather than combine the images from both nights, since the inclusion of the slightly poorer images leads to at best a marginal improvement in the signal-to-noise ratios. The final JHK$_S$ images we use are shown in Figure 3.5.

We carried out PSF-fitting photometry on each stacked image using `DAOPHOT` (Stetson, 1987), using isolated sources on the image to model the PSF. To calibrate the photometric zero points, we imaged standard stars P576-F, S165-E, S264-D and S279-F (Persson at al. 1998), took photometry in a large aperture containing most of the flux and aperture-corrected the science-frame PSFs using aperture photometry on the PSF stars (after subtraction of neighboring fainter stars). We estimate the uncertainty in the photometric zero points to be $\approx$0.025 mag for each band. For future reference, we give the photometry and positions for a number of stars in the field in Appendix A.

To find the astrometric solutions for our images, we identified stars from the Guide Star Catalog (GSC) 2.2[7] on our J-band image. With 24 stars, the RMS residuals in the solution were $\approx 0\farcs15$ in each co-ordinate. The systematic uncertainty in the GSC astrometry is $0\farcs2$ to $0\farcs4$, so our total uncertainty in transforming the *Chandra* position reported by Israel at al. (2003) (accurate to $0\farcs7$) is $0\farcs8$ at 90% confidence. This positional error circle is shown in Figure 3.5. We found astrometric solutions for the rest of our images by tying them to the Magellan J-band image, which introduces negligible additional uncertainties. Stars A and B are the two brightest sources within the error circle. Their positions are ($17^{d}08^{m}46\fs890$, -40°08′52″.53) for Star A and ($17^{d}08^{m}46\fs904$, -40°08′52″.64) for Star B. (Here the relative positions are accurate to the digits given, as measured from the NACO K-band image below, and are on the same astrometric system as the positions listed in Appendix A from Magellan.)

The separation between Star A and Star B is only $\approx 0\farcs26$ (measured from the NACO images below), and so they can only be measured individually in the K-band, where there is the most flux and the seeing was best. Even so, one might expect that the magnitude of the fainter Star B is poorly measured. Star A's magnitude, however, should be robust and not affected by the proximity of Star B. For the H and J bands, Star B could not be measured, but this should not affect the magnitudes for A too much since the AO images show that Star B is over a magnitude fainter in both bands. The final magnitudes are shown in Table 3.4.

3.4.5 CFHT

We retrieved from the CADC archive and re-analyzed the CFHT images presented by Israel et al. (2003). The AOB uses a wavefront sensor and deformable mirror to correct for atmospheric distortions, as measured from a natural guide star. The corrected beam is sent through to the KIR detector, a Hawaii array with $0\farcs035$ pixels (see Rigaut et al. 1998). The

[6]The broad-band filter centred at 1.035 μm
[7]Vizier Catalogue I/271

final reduced stacked images were created in a standard manner as above; the result is shown in Figure 3.5.

The region of interest is about $12\farcs5$ off-axis with respect to the (fairly faint) AO guide-star and the field is never below an airmass of 1.9 from CFHT. The AO correction is therefore far from optimal, and the isoplanatic patch is smaller than the field of view. This means that the PSF varies from something core-dominated near the guide star (ideally an Airy pattern) to something more Gaussian at the furthest point. At no place on the image does the PSF fit a simple analytic model. This makes photometry difficult, whether by PSF fitting or by integrating in fixed-sized apertures.

In order to photometer Stars A and B on the CFHT images, we constructed a PSF based on the average of many stars across the field with a Lorentzian analytic portion, which hopefully will be a reasonable fit in the field center. Even though this fit will not be particularly good, Stars A and B will share the same true PSF (being so close together), and their relative magnitudes will be accurate. Note that although `DAOPHOT` does have the ability to handle a PSF which varies across the image, there were not enough PSF stars available on a relatively small field of view for this to work.

In order to calibrate our magnitudes, we calculated the magnitude offset relative to the calibrated Magellan images (above) for a number of isolated stars near to and roughly circularly distributed around the area of interest. Although the magnitudes show a fair amount of scatter ($\sigma \sim 0.05$ mag in each band), with some systematic trends with position, the average offset is well determined and should be suitable for calibrating the two stars of interest. We estimate a total uncertainty in the photometric zero points of 0.03 mag in each band. See Table 3.4 for the final calibrated magnitudes.

Although the K_S-band and the K' band do not exactly overlap, they are close enough that an error due to this is negligible compared to the uncertainty in the photometric zero point above. We see no significant trend in the zero-point offset with $H - K$ color.

3.4.6 VLT/NACO

The source was imaged in three bands using NAOS-CONICA, the Nasmyth Adaptive Optics System and Near-Infrared Camera on VLT Unit telescope 4 (NACO: see Lenzen et al. 2003; Rousset et al. 2003). CONICA is a 1024 pixel square Aladdin detector (with $0\farcs027$ pixel scale).

We retrieved these data from the ESO archive and reduced them in a similar way to that above. The signal-to-noise ratio of individual stars is much better than for the CFHT observations (see Figure 3.5). The isoplanatic patch is once more smaller than each of the images (particularly for the J-band), so we compare the (instrumental) magnitude offsets a set of isolated, well-measured stars near Stars A and B to those measured with Magellan. The final calibrated magnitudes and errors are shown in Table 3.4. We stress once more that while these magnitudes include systematic uncertainty from the calibration of the magnitude zero-points, the relative magnitudes between Stars A and B within an image are very well determined.

Table 3.4. List of detections.

Observation	J_A	H_A	K_A	J_B	H_B	K_B	ΔK_{AB}
Magellan/PANIC	20.83(10)	18.75(5)	17.45(4)	···	···	19.26(16)[b]	1.81(16)
CFHT/AOB	···	18.82(6)	17.52(5)[a]	···	20.29(13)	19.02(8)[a]	1.50(6)
VLT/NACO	20.88(9)	18.75(6)	17.52(3)	21.89(14)	20.19(7)	18.86(3)	1.344(15)

Note. — Numbers in parentheses indicate 1σ errors in the last digit

[a]The K' band is very close to the more common K_S band.

[b]This measurement is likely affected by the proximity of StarA

3.4.7 Results

We find that the observations above present three items of evidence that the real counterpart to 1RXS J170849.0−400910 is Star B rather than Star A as previously reported by Israel et al (2003). These items may not be conclusive individually, but together make, we argue, a compelling case. They are discussed separately below. The only argument which favors Star A is that it lies closer to the center of the positional error circle, but both lie within the 90% confidence radius.

Before discussing our lines of argument, we should mention that the magnitudes we found for Star B are in disagreement with those presented by Israel et al. (2003), but our magnitudes for Star A are in good agreement (especially with the NTT data; note that in the published paper, there was a typo: the magnitude of Star A from the NTT should have been 17.3 ± 0.1; Israel, 2005, pers. comm.). We suspect that the discrepancy is due to the use of the on-axis PSF for measuring the stars (the authors claim a $0\farcs12$ FWHM, but this is not the case at $12\farcs5$ from the guide star). With our procedure of using stars close to the sources to create the PSF, and with the much better signal-to-noise ratio with the NACO images, we believe our photometry highly accurate, particularly for the relative magnitudes of Stars A and B.

In Appendix A we also list photometry for faint sources in or near the positional error circle, which are detected only in the VLT/NACO K-band image. Without color information or previous measurements, it is not possible to judge the likelyhood of one of these being the AXP counterpart, except that they would imply a very large X-ray to infrared flux ratio in comparison to other AXPs. Given the arguments in favour of Star B being the counterpart below, we do not consider these faint sources further, but list their measurements in the Appendix for completeness.

3.4.8 Variability

The relative magnitudes (ΔK) given in Table 3.4 are independent of the photometric calibration performed, and show that one of the two stars has varied (at 3-σ significance).

From the magnitudes of the individual stars, it would appear that Star A shows no significant variability in any band, whereas Star B apparently brightened. The NACO K-band magnitude is inconsistent at the 2σ level with that from CFHT, and at the 1.9σ level with that from Magellan. A slight brightening is also seen in the H-band, but this is not statistically significant. Together, it seems highly likely that Star B has varied.

As a check, the K-band magnitudes of Star 2 (see Figure 3.7) from Magellan, CFHT and VLT are 18.74(8), 18.88(8) and 18.75(3) respectively. This shows that this field star is consistent with a constant brightness, and that the uncertainties in the magnitudes are reasonable.

Variability, especially in the K-band is a generic property of AXPs (Israel et al. 2002; see also Hulleman et al, 2004, Tam et al., 2004, Durant & van Kerkwijk, 2005a), so this hint of variability in Star B and not in Star A is a point in favor of Star B being the true counterpart.

3.4.9 Stellar colors

Figure 3.6 shows all the stars in the Magellan images on a color-color diagram (after a cut on the χ goodness-of-fit diagnostic to reject the worst measured $\sim$10% of stars). Star A has been plotted using its Magellan photometry, and Star B using its VLT/NACO magnitudes relative to Star A (since Star A has not been seen to vary, this should be secure).

Three different groups of stars with $A_V \approx 5.8$, 10.5 and 20 can be seen in Figure 3.6. Main sequence and red giant sequences are shown for these values of reddening. The first two groups are expected from our analysis of the run of reddening with distance in this direction (Durant & van Kerkwijk, 2006b). Star A appears to inhabit the most reddened group of stars ($A_V \sim 20$), with a distance $d > 5\,\mathrm{kpc}$. Star B is, however, unusual: less than 5% of field stars (about 20 out of 450 in the $40''$ square region of analysis) are as far from the expected stellar sequences. Star B does not fit stellar colors at any reddening.

Other AXPs show non-stellar colors (e.g. Hulleman et al., 2004) and similar colours have been seen in the infrared for 1E 1048.1−5937 ($J - H = 0.9(4)$, $H - K_S = 1.4(4)$; Wang & Chakrabarti, 2002) as well as 4U 0142+61 ($J - H = 1.2(2)$, $H - K' = 1.1(2)$; Israel et al. 2004). It is unlikely for an ordinary star to occupy the same region of parameter space as Star B. Its position is consistent with an infrared excess, possibly from dust emission, as has been found for 4U 0142+61 by Wang et al. (2006). The probability of a chance coincidence of a star with such colors in the positional error circle is small ($\approx 20 \times \pi 0\farcs8^2/(40'')^2 \approx$2.5%).

The color-color diagram hence offers further support for Star B being the infrared counterpart to 1RXS J170849.0−400910.

3.4.10 X-ray to infrared flux ratio

For the four other AXPs with infrared counterparts, we found that they were remarkably similar in their X-ray (2–10 keV) to K-band flux when not in outburst (Durant & van Kerkwijk, 2005a): all have $F_X/F_K = 2700\ldots6000$ (1E 1048.1−5937, 4U 0142+61, 1E 2259+589 and XTE J1810−197).

If Star A were the counterpart to 1RXS J170849.0−400910, this would imply a flux ratio $F_X/F_K = 660$, whereas for Star B we get (for the range of magnitudes) $F_X/F_K = 2300\ldots2870$. (Here we used $F_X = 6.4 \times 10^{-11}\,\mathrm{erg\ s^{-1}cm^{-2}}$ [Woods & Thompson, 2004] and

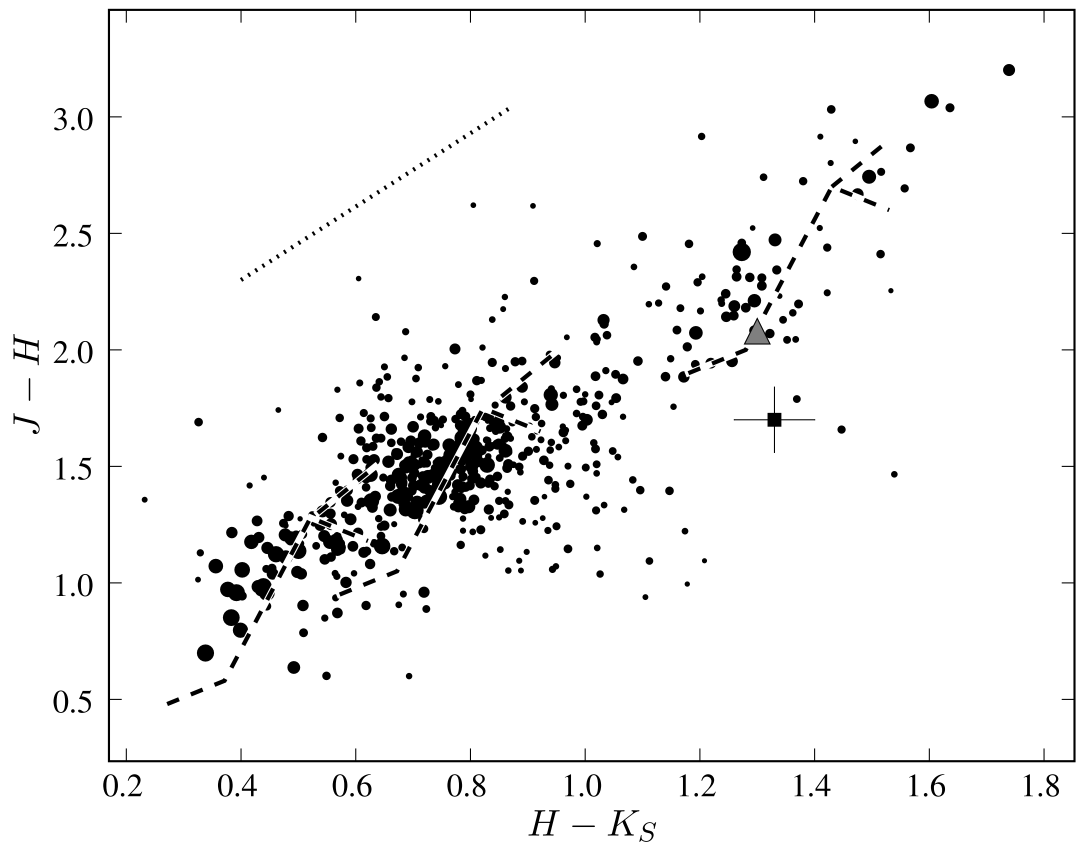

Figure 3.6 Color-color magnitude diagram for 450 stars detected in all three Magellan bands. Symbol sizes are scaled inversely to the uncertainties. Stars A and B are shown as the triangle and filled square with error bars respectively. Also shown are the reddening vector for the AXPs estimated reddening, $A_V = 7.4$ (dotted line, e.g. Schlegel et al., 1998) and colors expected for main sequence and red giant stars (dashed lines from Bessel & Brett, 1988) reddened by $A_V = 5.8$, 10.5 and 20, increasing left to right; the upper branches are main sequences and the lower branches giants.

$N_H = 1.3 \times 10^{22}\,\mathrm{cm}^{-2}$ [Durant & van Kerkwijk, 2006a]). Only the latter value is in the same range as the other AXPs, which suggests Star B is the more likely infrared counterpart.

3.4.11 Conclusions

We presented three lines of evidence that suggest that Star B is the true counterpart to 1RXS J170849.0−400910: its variability, its unusual stellar colors and the consistency with other AXPs for its inferred X-ray to infrared flux ratio. Of these, the colors are perhaps the strongest piece of evidence. Together they strongly support the identification of Star B as the counterpart.

Despite their proximity on the sky, it seems unlikely that Stars A and B are physically associated. The hydrogen column for 1RXS J170849.0−400910 of $1.3\times10^{22}\,\mathrm{cm}^{-2}$ is equivalent to a visual extinction $A_V \approx 7.3$ (Durant & van Kerkwijk, 2006a), which is hard to reconcile with the reddening of $A_V \sim$20 for Star A from its colors.

With this addition, all but one of the AXPs now have securely identified optical/infrared counterparts (with the exception being 1E 1841−045; see Durant, 2005). Intriguingly, the sources appear to be rather similar in some of their properties: they have similar X-ray luminosities (Durant & van Kerkwijk, 2006b) and similar K-band to X-ray flux ratios. From the three sources with optical counterparts however, there appear to be different X-ray to optical flux ratios. While compared to 4U 0142+61, 1E 1048.1−5937 has a similar X-ray to I-band flux ratio, CXOU J010043.1−721134 has a significantly lower X-ray to V-band flux ratio (Durant & van Kerkwijk, 2005b). This suggests that the optical and infrared emission are produced by different mechanisms, with the infrared more closely tied to the X-ray. The idea of Wang et al. (2006) of infrared emission coming from a passively illuminated dusty fall-back disc at the sublimation radius would seem to be consistent with these data.

Acknowledgments: This work made use of the CFHT archive hosted by CADC, of the ESO VLT archive (for programme 71.D-0503) and of the Vizier archive service of the CDS. We used astrometric information from the Guide Star Catalog 2.2 by the Space Telescope Science Institute and Osservatorio Astronomico di Torino. We acknowledge financial support by NSERC.

3.4.12 Appendix: Photometry

In Table 3.5 we list the Magellan JHK magnitudes and positions of stars in the field, as labeled in Figure 3.7. In Table 3.6 we list the K-band magnitudes and positions of faint sources detected in or around the position error circle, as measured in the VLT/NACO observations (Figure 3.8). None of these sources were detected in H or J, with limits $H > 22.1$, $J > 22.6$ respectively, at 95% confidence.

Table 3.5. Photometry of field stars.

ID[a]	R.A. (J2000)	dec (J2000)	J	H	K_S
1	17:08:46.919	-40:08:52.97	21.28(18)	20.6(2)[b]	20.02(6)[b]
2	17:08:46.912	-40:08:53.41	20.81(11)	19.34(9)	18.74(7)
3	17:08:47.029	-40:08:53.24	20.38(7)	19.30(9)	18.48(5)
4	17:08:47.153	-40:08:53.69	18.067(10)	17.216(12)	16.833(13)
5	17:08:46.846	-40:08:56.89	21.8(3)	19.53(11)	18.33(5)
6	17:08:47.088	-40:08:57.79	18.98(2)	16.352(6)	15.005(3)
7	17:08:47.322	-40:08:57.48	17.201(5)	15.601(3)	14.793(3)
8	17:08:47.022	-40:08:55.82	22.0(4)	20.4(3)	19.63(17)
9	17:08:47.131	-40:08:55.65	19.73(4)	18.48(4)	17.92(3)
10	17:08:47.190	-40:08:55.12	21.9(3)	20.3(3)	19.35(14)
11	17:08:47.292	-40:08:54.35	19.82(4)	18.48(4)	17.80(3)
12	17:08:47.300	-40:08:53.96	19.85(4)	18.43(4)	17.72(3)
13	17:08:47.329	-40:08:52.07	16.316(2)	15.471(3)	14.980(3)
14	17:08:47.270	-40:08:51.70	18.293(12)	16.036(5)	14.838(3)
15	17:08:47.190	-40:08:50.35	18.077(10)	16.997(10)	16.445(9)
16	17:08:47.124	-40:08:50.28	18.850(19)	17.512(15)	16.85(13)
17	17:08:47.124	-40:08:48.65	18.867(19)	18.23(3)	17.74(3)
18	17:08:46.970	-40:08:48.88	17.829(8)	15.814(4)	14.620(3)
19	17:08:46.816	-40:08:49.36	20.84(11)	19.50(7)	18.72(7)
20	17:08:46.772	-40:08:49.27	21.11(14)	19.62(11)	18.88(9)
21	17:08:46.714	-40:08:50.30	16.189(2)	15.520(3)	15.223(3)
22	17:08:46.728	-40:08:51.27	16.745(4)	15.990(4)	15.624(3)
23	17:08:46.699	-40:08:51.59	19.01(2)	16.592(7)	15.319(3)
24	17:08:46.765	-40:08:52.44	21.5(2)	19.82(16)	18.68(7)
25	17:08:46.714	-40:08:54.90	21.5(2)	19.87(17)	18.85(9)
26	17:08:46.626	-40:08:54.98	18.829(18)	17.719(19)	17.241(19)
27	17:08:46.611	-40:08:50.16	19.73(4)	18.23(3)	17.52(2)

Note. — Numbers in parentheses indicate 1σ errors in the last digit, and do not include photometric zero-point uncertainties (approximately 0.025 mag in each band). Positions are in hours for R. A. and degrees for declination. All data from Magellan imaging. For Stars A and B see Table 3.4

[a]As shown in Figure 3.7

[b]Measured from the NACO images, because of the proximity of other sources.

Table 3.6. Photometry and positions of stars in or near the positional error circle.

ID[a]	R.A. (J2000)	dec (J2000)	K_S
p	17:08:46.875	-40:08:51.75	21.12(13)
q	17:08:46.912	-40:08:52.33	20.93(11)
r	17:08:46.926	-40:08:52.85	21.6(2)
s	17:08:46.882	-40:08:53.11	20.76(9)
t	17:08:46.853	-40:08:53.25	21.40(17)
u	17:08:46.816	-40:08:52.96	21.6(2)
v	17:08:46.838	-40:08:52.52	20.85(10)
w	17:08:46.838	-40:08:52.38	21.36(17)

Note. — Numbers in parentheses indicate 1σ errors in the last digit, and do not include photometric zero-point uncertainties (approximately 0.03 mag).

[a]As shown in Figure 3.8

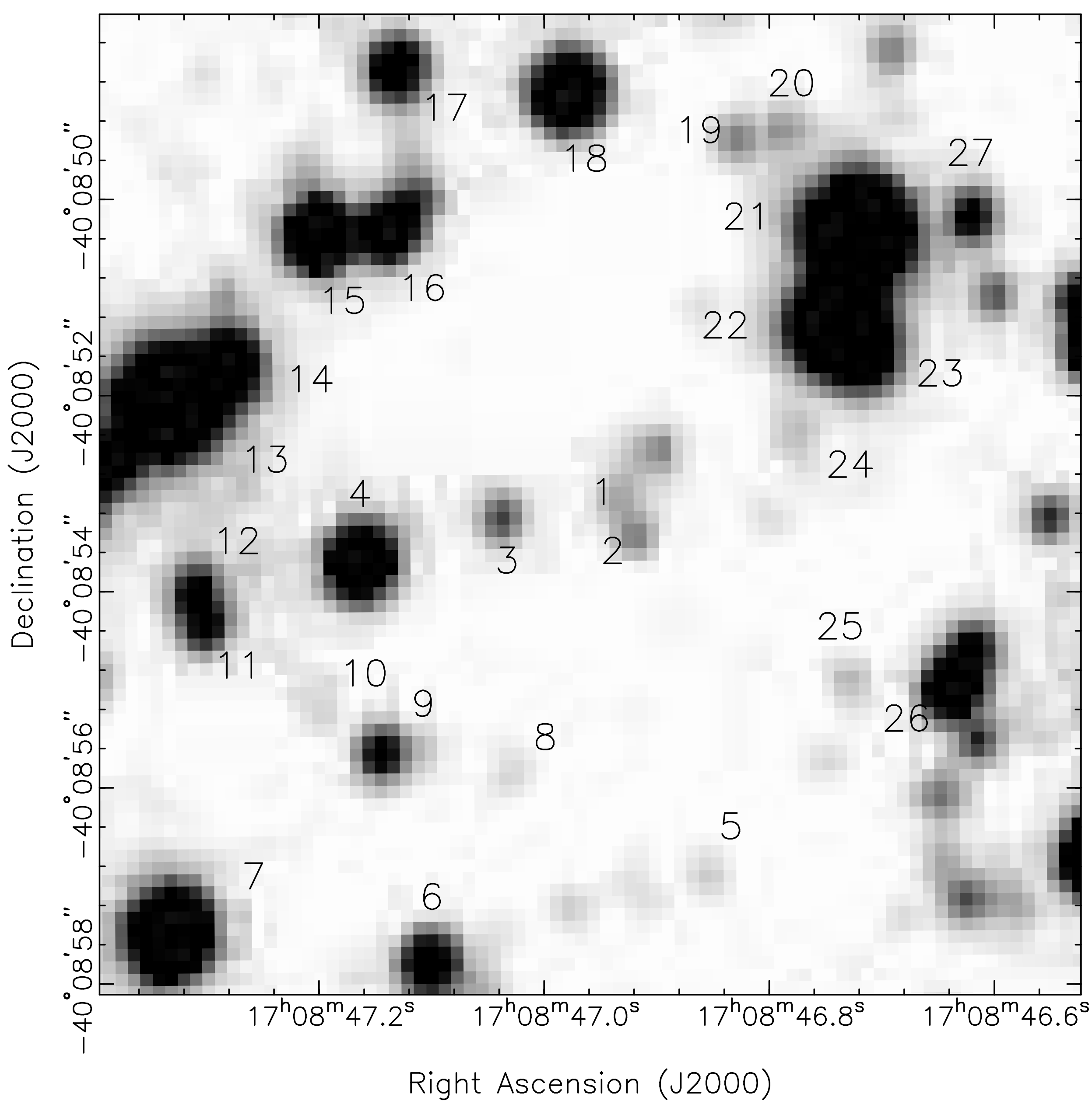

Figure 3.7 Magellan infrared J-band image of the field of 1RXS J170849.0−400910, with labeled field stars. The stars' magnitudes and positions are listed in Table 3.5.

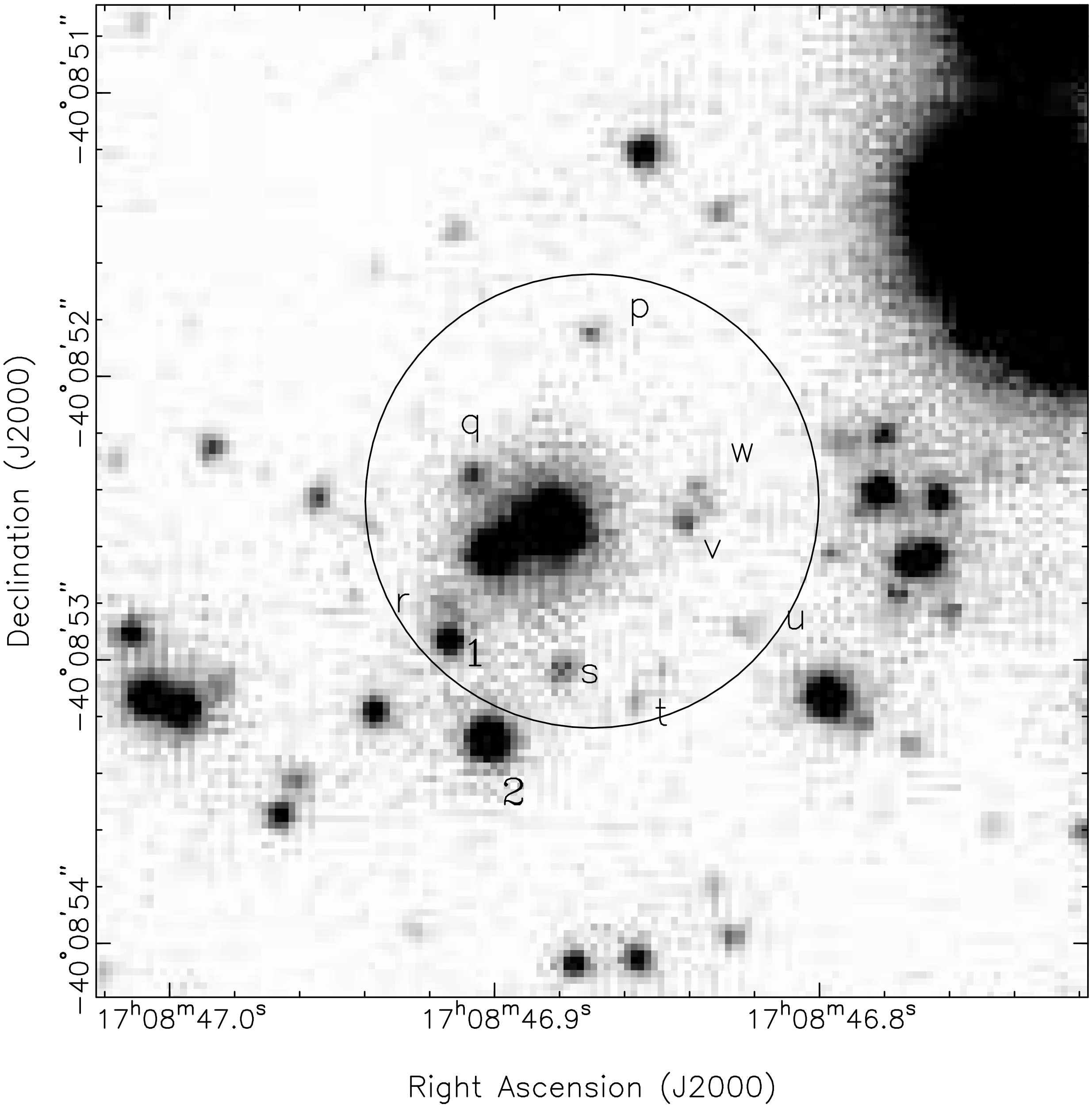

Figure 3.8 VLT/NACO infrared K_S−band image of the field of 1RXS J170849.0−400910. Stars within the *Chandra* positional error circle are labeled, and their magnitudes are listed in Table 3.6. Also shown are the two closest numbered stars from Figure 3.7.

Chapter 4

Multi-wavelength variability of the magnetar 4U 0142+61 [1]

4.1 Abstract

We have collected data spanning seven years of observations of the magnetar 4U 0142+61 in the infrared, optical and soft X-rays. These combine our own observations and analysis of archival data. We find that the source is variable in the optical, in contrast to what had been previously reported, that the K-band flux can vary by over a magnitude on the time-scale of days, and that the X-ray pulsed flux is not obviously correlated with either the total X-ray flux or infrared and optical fluxes. Furthermore, from multi-color photometry of the source within single nights, we conclude that there are two separate components to the infrared emission. The overall picture is unclear, and prompts the need for further, more frequent observations.

4.2 Introduction

The Anomalous X-ray Pulsars (AXPs) are a group of about six young, energetic neutron stars. They are termed *anomalous* since their energy source was initially not known: the rotational spin-down luminosities are too low and no binary companions are found. They are now modeled as *magnetars* along with the Soft Gamma-ray Repeaters. Magnetars are neutron stars with external magnetic fields of the order 10^{15} G and even stronger internal fields. It is this magnetic field which acts as an energy reservoir and powers the observed emission as it decays (Thompson & Duncan, 1995, 1996). See Woods & Thompson (2004) for a review of magnetar characteristics.

The variability of AXPs has for a long time been of interest both in the X-ray band and the infrared for long-term and transitory events. For example, whereas 1E 2259+586 and XTE J1810−197 showed correlated X-ray and infrared emission following outbursts (Tam et al. 2004; Gotthelf at al. 2004), Durant & van Kerkwijk (2005a) found that for 1E 1048.1−5937 there was possibly an anti-correlation between the infrared and X-ray fluxes. Nevertheless, the AXPs generally seem to have consistent X-ray to infrared flux ratios.

4U 0142+61 was discovered at a 8.7 s X-ray pulsar by Israel et al. (1994), and is the brightest of the AXPs in the sky. It was initially modeled with a hot black-body spectrum

[1] Accepted for publication in ApJ (Durant & van Kerkwijk, 2006d).

($kT \approx 0.4$ keV, e.g. White et al. 1996), and soft power-law at higher energies. No narrow features have yet been found in the X-ray spectrum in the 1–10 keV range (Juett et al. 2002).

Hulleman et al. (2000, 2004) detected 4U 0142+61 in the optical and infrared. The emission was found to be orders of magnitude below the extrapolation of an X-ray power-law fitted to the X-ray spectrum, yet orders of magnitude above the extrapolation of an X-ray black-body component. By excluding the possibility of a faint binary companion or of substantial accretion from supernova fall-back material, they excluded two alternative scenarios to the magnetar model. The optical emission was found to be pulsed at the pulsar period, with a large pulsed fraction (Kern & Martin, 2002; Dhillon et al. 2005), clearly identifying it as magnetospheric in origin.

Recently, 4U 0142+61 has been detected in new spectral windows: Wang et al. (2006) detected the object in two *Spitzer* imaging bands, attributing the measured flux to thermal emission from a dusty circumstellar disc; and den Hartog et al. (2006) identified the AXP from long (∼2 MS) INTEGRAL observations - they found it has a rising spectrum in the 20–150 keV range which dominates the energetics.

Durant & van Kerkwijk (2006a) determined the interstellar extinction to 4U 0142+61 by direct measurement of the optical depths in individual photo-electric absorption edges from high-resolution X-ray spectra. They found that the inferred column density was 40% less than had typically been stated from broad-band spectral modeling, which solved a long-standing inconsistency between the implied reddening to the source and the total reddening along the line of sight (see Hulleman et al. 2004). This also revealed a possible, broad spectral feature in the X-ray spectrum near 830 eV (13Å), a first for an AXP.

In this paper we present many different observations at different epochs, from different observatories and in different parts of the spectrum. Some of these we take from the literature, some we have obtained from archival data and some are from our own observations. We describe in detail the data and reduction for both the observations we obtained and those retrieved from the archives. The following sections enumerate the observations in decreasing order of wavelength. In Section §4.6 we compare both our data and those in the literature and investigate the time-scales, correlations and spectral dependence of the variability seen.

4.3 Near-Infrared Observations

Table 4.1 lists all the observations of 4U 0142+61 we are aware of in the near-infrared (NIR), spanning several years. The Keck magnitudes were taken from Hulleman et al. (2004), and we obtained new observations from Gemini. For the other observations (from CFHT and Subaru), we analyzed data from the archives. All the final magnitudes and associated uncertainties are listed in Table 4.1. We briefly describe the reduction and analysis procedures we followed for each of the observations that we analyzed.

For the K-band, we have analyzed observations taken in the three similar, but not identical, filters: K, K_S, and K'. Each has a roughly rectangular bandpass, centered on $\lambda_{eff} = 2.2$, 2.15 and 2.12 μm and with width 0.16, 0.15 and 0.18 μm, respectively. Using K_S as our baseline, the overlap between the filters is greater than 80% for K and greater than 90% for K'. From the standard star list of Oersson et al. (1998) and their interpolation to K'[2], we find that the magnitude difference between K_S and K, and K' and K is between 0 and

[2]see http://www.mpia-hd.mpg.de/IRCAM/FAINTSTD/faintstd_kprime.html

0.04 mag for a range of stellar colors. Since 4U 0142+61 has an intermediate $H-K$ color, the uncertainty on the K flux from assuming that the filters are identical is at most 4%.

4.3.1 Gemini

The Gemini observations were taken in a concerted effort to investigate the infrared variability of 4U 0142+61, using NIRI, the Near Infrared Imaging instrument (Hodapp et al. 2003) at Gemini-North. NIRI is available for both imaging and spectroscopy, and can be used as the detector for the output of ALTAIR, the Gemini adaptive optics (AO) system. Here we do not use AO. The plate scale is $0\farcs11$ per pixel on the 1024 square Aladdin array.

The observation are from four separate nights from September 2003 to July 2005. On the 2, Nov 2004 H- and J-band images were obtained in addition to the K-band images. The last of our Gemini infrared observations (July 2005) was taken under a DDT proposal to attempt to observe 4U 0142+61 across the whole EM spectrum quasi-simultaneously (see Den Hartog et al, in prep.).

We created final images after subtracting dark frames and dividing by a flat-field image derived from the science images. For the K_S image, we measured our magnitudes relative to the stars listed in Hulleman et al. (2004). We find that the relative zero-point offsets accurate to ≈ 0.016 mag, and that the magnitudes measured for the AXP are in-between the K and K_S magnitudes presented by Hulleman et al. In November 2004, we also obtained images of standard stars FS-34, FS-112 and FS-145 in all three filters, and used these to calibrate the magnitude zero points of the J- and H-band images. To do this, we calculated an aperture correction for the science images by performing aperture photometry around our PSF stars with the same large aperture used to measure the standard stars. These calibrations are not as accurate as for the K-band (uncertainty ≈ 0.025) mag), but the detections are poorer, so this does not contribute any additional uncertainty.

4.3.2 CFHT

Israel et al. (2004) reported observations of 4U 0142+61 on 18 August 2002 with the Adaptive Optics Bonette (AOB, Rigaut et al. 1998) of Canada-France-Hawaii Telescope (CFHT), Hawaii. The adaptive optics system produces PSFs of reduced size in order to increase the signal-to-noise ratio, and the corrected beam is imaged by KIR, a 1024 square Hawaii infrared detector with $0\farcs035$ per pixel. We retrieved the data from the CADC archive and re-analyzed them in order to derive accurate relative magnitudes. The frames were dark-subtracted and then flat-fielded using the median of the data frames. The field of view is relatively small and contains only a handful of stars. The FWHM of the PSF near the AXP was $\approx 0\farcs14$.

We performed photometry using the PSF-fitting package, `daophot` (Stetson, 1987). The PSF varies somewhat across the field of view, so we constructed the model PSF from a few stars distributed across the field. The analytic portion of the PSF was best fitted by a Lorentzian function, and the residual image showed no systematic effects.

To calibrate the magnitude zero-points for the K-band image, we used the photometry of several stars in the field listed by Hulleman et al. (2004). The K_S band and K' band do not exactly co-incide, but they are very close in effective wavelength (2.15μm and 2.12μm respectively), and so we treat them as identical, in the absence of standard stars observed on the night. To calibrate the J- and H-band photometric zero points, we used our images from Gemini (above).

We verified our calibration with two 2MASS stars on the image, which gave consistent zero points. We chose to use the relative photometry as it does not add any additional uncertainty. With the relative photometry we compare the brightness of our source with stars of similar brightness rather than the 2MASS stars which are much brighter.

4.3.3 Subaru

4U 0142+61 was imaged with the Infrared Camera and Spectrograph for the Subaru Telescope (IRCS, Kobayashi et al. 2000) on two successive nights, Sep 3 and 4, 2003 - see Morii et al. (2005). IRCS has a 1024 pixel square Aladdin array, with $0\farcs053$ per pixel. On the first night, only K-band imaging was performed, and on the second night J, H and K. We retrieved the data from the archives (SMOKA) and reduced them.

The IRCS detector suffers from a number of cosmetic artifacts, and variable sensitivity across the detector. In order to successfully perform the flat-fielding, we found the screen flats only partially useful, leaving medium to large scale variations uncorrected. We created flat-field images by taking the median of the science images, scaled by the mode of their data and after rejecting outliers. For the K-band images of the second night (showing the largest variations across the field and with a variable sky background), we used both the screen flat, followed by the median of the partially corrected images.

The photometry for the K_S-band was calibrated relative to Hulleman et al. (2004) and relative to the Gemini frames above for the H- and J-bands, as for the CFHT images. The 2MASS stars in the field again give consistent zero-point offsets to our method.

4.4 Optical Observations

Table 4.2 lists all the observations of 4U 0142+61 in the optical over the last few years. We include both measurements made by us from our own observations, and several from the literature. We do not have access to any of the archival data, so re-analysis for better relative photometry was not possible.

4.4.1 Keck

We obtained two nights of observations of 4U 0142+61 using the Echellette Spectrograph and Imager (ESI; Epps & Miller, 1998) at Keck-II, Hawaii. In imaging mode, the instrument provides a standard set of Johnson-Cousins filters, with the exception of the R-band, where the Ellis filter is used (R_E), which is slightly shifted from the standard Cousins R filter.

The detector employs dual-amplifier readout, and the bias has to be subtracted from the two separate regions of the images (the bias is easily derived from over-scan regions). In the case that the field of view was located wholly within one amplifier area, we discarded the other half of the image. We created flat-field images from screen-flats taken on each night, and registered and stacked the images after the correction. Since the observations in each band typically consisted of only two images, some artifacts and cosmic rays remain on the final image. None of these fall close to the object of interest, and they do no affect our measurements.

Table 4.1. Infrared observations of 4U 0142+61

Date	MJD	Telescope/Instrument	K^{a}	H	J
1999-02-08	51393	Keck-I/NIRC	$K = 19.68 \pm 0.02^{b}$		
2001-10-30	52213	Keck-I/NIRC	$K_S = 20.15 \pm 0.08^{b}$		
2002-08-18	52505	CFHT/AOB	$K' = 19.76 \pm 0.05$	20.52 ± 0.11	21.96 ± 0.12
2003-09-08	52891	Subaru/IRCS	$K' = 20.18 \pm 0.08$		
2003-09-09	52892	Subaru/IRCS	$K' = 20.78 \pm 0.08$	20.90 ± 0.08	22.18 ± 0.09
2003-09-14	52897	Gemini/NIRI	$K_S = 19.85 \pm 0.04$		
2003-10-29	52942	Gemini/NIRI	$K_S = 19.83 \pm 0.03$		
2004-11-02	53312	Gemini/NIRI	$K_S = 19.96 \pm 0.07$	20.69 ± 0.12	21.97 ± 0.16
2005-07-26	53578	Gemini/NIRI	$K_S = 19.96 \pm 0.10$		

Note. — Uncertainties are 1-sigma, and do not include zero-point errors (which are small in comparison); they are accurate relative to one-another.

[a]Magnitudes refer to the K, K_S and K' bands, as shown. These are all approximately interchangeable.

[b]Taken from Hulleman et al. (2004).

Table 4.2. Optical observations of 4U 0142+61

Date	MJD	Telescope/Instrument	I	R	V
1994-10-31	49657	Keck-I/LRIS		24.89 ± 0.08[a]	25.62 ± 0.11[a]
1999-09-06	51428	Keck-II/LRIS	23.84 ± 0.06[a]	24.89 ± 0.07[a]	
2002-09-12	52530	WHT/ULTRACAM	$i' = 23.7 \pm 0.1$[a]		$g' = 27.2 \pm 0.2$[a]
			23.9 ± 0.2		
2003-01-02	52642	Keck-II/ESI	23.77 ± 0.11	25.29 ± 0.19	26.10 ± 0.18
2003-09-04	52887	UH88/OPTIC	23.97 ± 0.09[a]	25.58 ± 0.18[a]	25.32 ± 0.13[a]
2003-12-21	52995	Keck-II/ESI	23.44 ± 0.18	25.34 ± 0.12	
2005-07-13	53566	Gemini/GMOS		$r' = 25.42 \pm 0.06$	
				25.2 ± 0.2	

Note. — Magnitudes that are not in the standard Johnson-Cousins system are listed under the nearest band, and the appropriate filter is given. These are based on the Sloan filter-set and have magnitudes which follow the AB system, rather than Vega magnitudes. The estimated Johnson-Cousins magnitudes are given immediately below each (for g' this is not possible, since it lies blueward of V).

[a]Taken from the literature: Hulleman et al. (2004), Dhillon et al. (2005) and Morii et al. (2005)

To calibrate the photometric zero points, we compared our instrumental magnitudes (from PSF fitting) with those listed in Hulleman et al. (2004). Whereas the I- and V-bands required no color term, the R_E-band does, since it does not well match the standard Cousins R-band. Fortunately, we identified enough stars in the December observation to achieve a well-defined zero-point offset versus $m_r - m_i$ color. For the January 2003 observation, rather that repeat this process, we found the relative offset from one R_E image to the other and used the same calibration (since the January observation was less good). Photon-noise dominates the uncertainty in the magnitudes listed in Table 4.2.

4.4.2 Gemini

As part of the simultaneous, multi-wavelength observation campaign for 4U 0142+61 (see §4.3.1 above), we obtained imaging data with the Gemini Multi-Object Spectrograph (GMOS-North, Hook et al. 2004). GMOS is equipped with an integral field unit, but we used it in imaging mode, with one amplifier covering a 1024×2304 pixel region with a pixel scale of $0\farcs07$. Unfortunately, the instrument is equipped with the SLOAN filter-set rather than Johnson-Cousins filters, so we opted for the middle of the optical band with the r' filter.

We subtracted the bias and applied a screen-flat correction, before stacking the images, and analyzing them with `daophot` as before. For the calibration, we used again the photometry listed in Hulleman et al. (2004), interpolating between the R- and V-bands using the relationship in Smith et al. (2002). Since we do not have a measure of color from the GMOS observations, we cannot interpolate the magnitude to either the R- or I-bands for comparison with earlier observations. However, we can obtain r' from earlier measurements. Doing this, we find that the r' magnitude is consistent with that inferred from the 01/2003 observations, but not from the other pairs of V and R magnitudes.

4.5 X-ray Observations

4U 0142+61 has been the subject of a long-term monitoring campaign with the Rossi X-ray Timing Explorer (RXTE) satellite. These observations have yielded roughly weekly measurements of the pulsed flux and pulse period of the pulsar. In addition, there have been extensive observations with XMM-Newton (the X-ray Multi-mirror Mission, see below) and Chandra (e.g. Juett et al. 2002). We do not consider the Chandra data, since there have been too few observations and using different instruments/modes to be useful.

4.5.1 RXTE

The Proportional Counter Array (PCA) instrument of RXTE has five proportional counting units, and provides very high time-resolution and moderate energy resolution in the 2–60 keV energy range (Jahode et al. 1996). The pulsed flux measurements are much more reliable than the total flux due to the non-imaging nature of the PCA instruments, and the nearby variable high-mass binary X-ray pulsar RX J0146.9+6121 (Motch et al. 1991). Observations were made for the epoch $MJD = 51700$ to 53700.

The data was analyzed in the same procedure as described in Gavriil & Kaspi (2002): an average pulse profile was created from several observations, and cross-correlated with each

Table 4.3. XMM-Newton/RGS soft X-ray observations of 4U 0142+61

Obs Code	Date	MJD	Flux (8–15Å) (10^{-11} erg s^{-1} cm^{-2})
0112780301	2000-12-28	51907	2.91 ± 0.04
0112481101	2003-01-24	52664	3.29 ± 0.03
0206670101	2004-03-01	53066	3.192 ± 0.013
0206670201	2004-07-25	53212	3.229 ± 0.017

Note. — 1-sigma errors are derived from the XMM task `rgsfluxer`

observation in order to obtain the (barycentred) average pulse arrival times, without losing coherence from one observation to the next.

The timing of the pulsar was found to be stable across the whole epoch, and well-described by a single ephemeris. Phase residuals are less than 0.05 cycles for the entire time-span.

In the first analysis, it appeared that the pulsed flux increased nearly linearly with time, by about 40% across the whole time-span. On closer inspection, this was found to be the case for only one of the five PCUs, and hence its data were discarded. We here use the pulsed flux measurements only from the remaining (four or less) PCUs. See Dib et al. (2006) for details.

4.5.2 XMM-Newton

In addition to the RXTE data, we analyzed archival *XMM-Newton* data, which is able to measure the total flux rather than just pulsed flux due to its better spatial resolution. Four observations exist in the archives, and these too span the range of time comparable to the other data. XMM has three telescopes and five instruments which take data simultaneously, but we decided only to use the data from the Reflection Grating Spectrometers (RGS; den Herder et al. 2001), since they were used in the same observation mode for all four observations.

We used the standard pipeline and the Science Analysis Software, (6.1.0, 2004-11-22) and the latest calibration files. For the final (background-subtracted) fluxes, we used the SAS task `rgsfluxer`. Although this task is not recommended for detailed spectral analysis, for calculating the total flux, its accuracy is ample.

In the range 515eV to 1550eV (8 to 15Å, where the sensitivity and calibration are well known), we find statistically significant variability between the observations, but only by about 10% at most, see Table 4.3.

4.6 Results

We plot the results of the measurements in infrared, optical and X-rays in Figure 4.1. For the optical magnitudes made under the AB magnitude system (from WHT/ULTRACAM and Gemini/GMOS-N), we estimate the appropriate Johnson-Cousins magnitude based on the transformations of Smith et al. (2002). In neither of the cases do we have $(r'-i')$ colors, but these can be estimated from the range of $(R-I)$ colors from the other observations. We show the points with increased error-bars to account for this uncertainty (see also Table 4.2).

4.6.1 Variability Time-scales

Whereas 4U 0142+61 was regularly observed with RXTE roughly once a week, the shortest delay between subsequent measurements occurred in the infrared K-band, with three observations within a week in September 2003. We find that the source varied by over a magnitude over a time-scale of days. Such rapid and large variability was not expected and was not seen before. Even more surprising, is the rapid dimming between the two Subaru nights – a rapid brightening could have been explained as originating in some kind of energetic outburst.

In figure 4.2 we show the three images of 4U 0142+61 in question, and clearly the object does vary substantially. The background blemish visible in the Subaru images near the source is outside of the PSF fitting radius and does not affect the photometry.

In the other wave-bands, such rapid variability is not seen, but the sampling has not been dense enough for us to be able to discount the possibility. Only in the X-ray can we state that for the longest observation, 44.1 ks for the March 2004 observation, the flux remained constant within the observation to high precision (in the 8–15Å range).

4.6.2 Correlations

We plot the flux measurement of 4U 0142+61 in the infrared, optical and X-rays versus time in Figure 4.1, and in Figure 4.3 we plot the measures of flux against one-another. We have calculated the RXTE pulsed flux appropriate for each observation in another band by linear interpolation between the two closest measurements in time.

No clear picture emerges from the two Figures. There is no apparent correlation between the K-band magnitude and pulsed flux. For the I and R bands and the XMM/RGS flux, the range of values is not big enough compared to the uncertainties to be able to make a definite statement.

Intriguingly, the large feature in the time-series of K-band photometry starting around $MJD = 52892$, showing a rapid dimming and re-brightening, has no change in the pulsed X-ray emission at that time. At this time, the source was at its faintest in I and R (but not V).

4.6.3 Spectral Changes and Components

In Figure 4.4, we show infrared and optical spectral energy distributions for each observations (each spectrum from within a single night's observation). In the infrared, the magnitude in H is clearly correlated with K, but K varies more than H. For J, it is not clear from our data

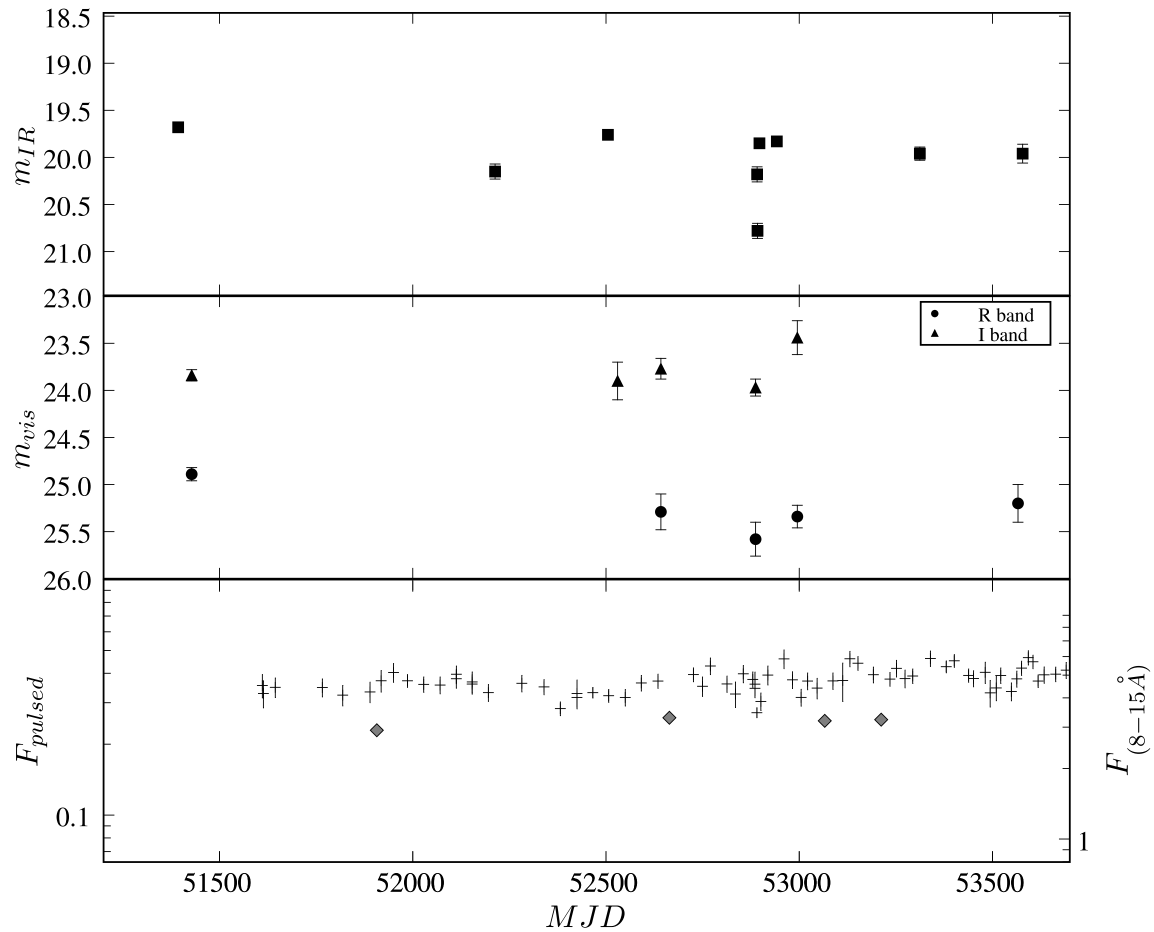

Figure 4.1 Compilation of flux data from the infrared (K-band, top), optical (middle) and X-ray (bottom). In the latter we show both pulsed flux from RXTE (pluses, in (cts s^{-1} PCU^{-1})) and total flux from XMM/RGS (grey diamonds, right hand scale, in (erg s^{-1} cm^{-2})). The X-ray fluxes are shown on logarithmic scales and span the same range as the optical/infrared, to match the logarithmic nature of the magnitude system.

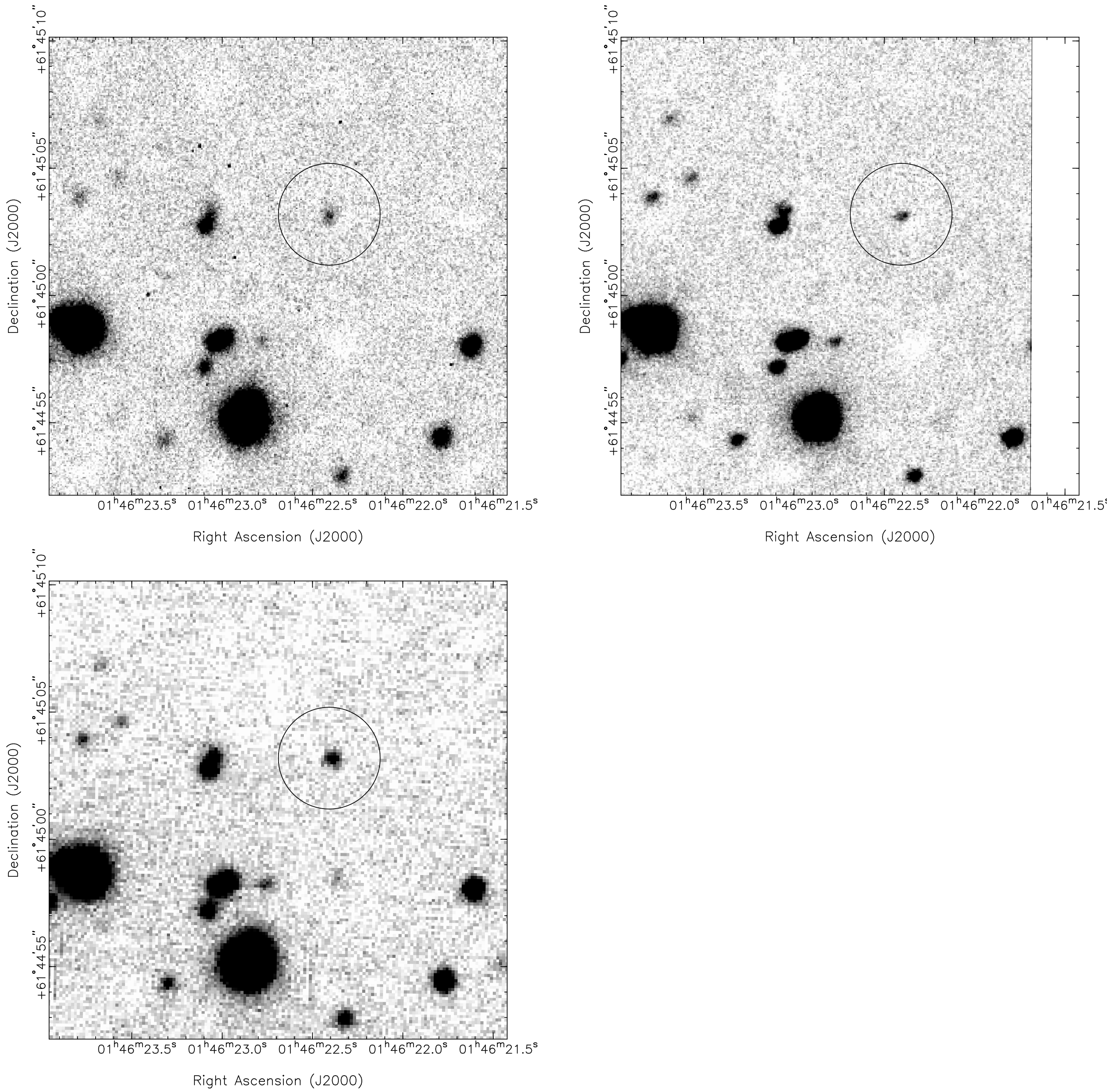

Figure 4.2 K-band images of 4U 0142+61. Top left is the Subaru image from 2003-09-08 ($K' = 20.18$), top right is the Subaru image from 2003-09-09 ($K' = 20.78$) and bottom is the Gemini image from 2003-09-14 ($K_S = 19.85$). The object is in the center of each over-drawn circle, and clearly varies compared to field stars

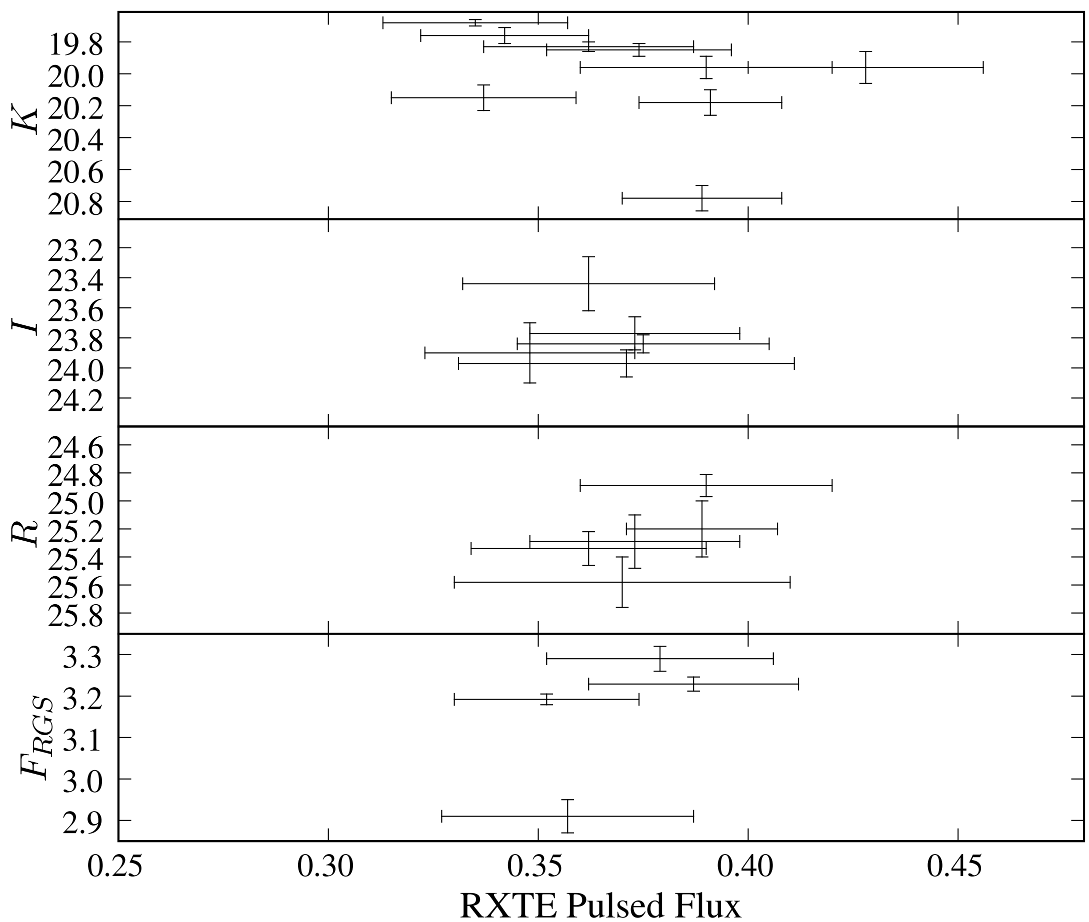

Figure 4.3 Graphs of the various measures of flux versus the only time-series which was continuous across the whole epoch: the RXTE pulsed flux (2–10 keV).

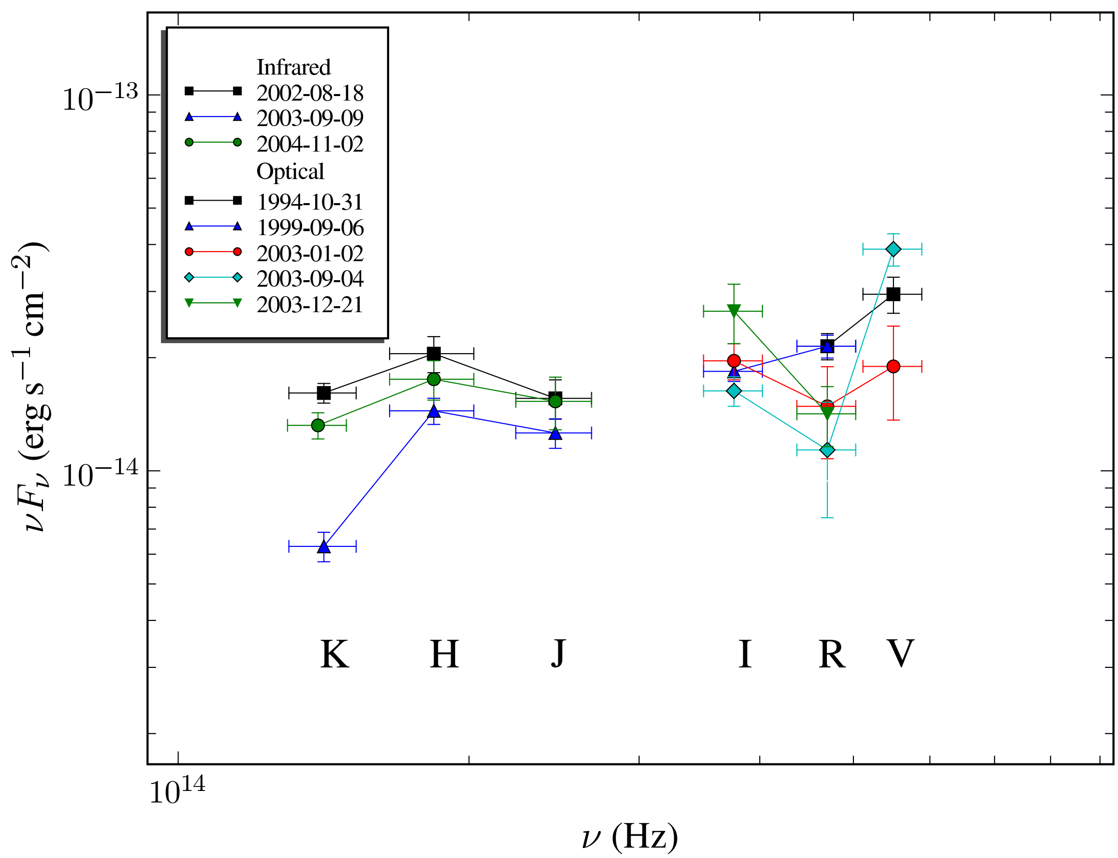

Figure 4.4 Variability in the spectral energy distribution of 4U 0142+61 for the different observations in the optical and infrared. We omit the ULTRACAM measurements, since the uncertainties are large.

whether it is also related to K, or whether it is better described as remaining constant; both are consistent with the data.

For the optical, the data show no apparent correlation at all between V and R. With only two simultaneous V and I measurements, we can say nothing of their possible relationship, except that both do vary (the estimated I and V magnitudes from the ULTRACAM data have very large uncertainties associated with them). The spectrum appears to be markedly different for each observation.

4.7 Conclusions and Discussion

We have shown that the infrared emission of 4U 0142+61 varies by over a magnitude on the time-scale of days, and that there are no obvious correlations between the infrared, optical and X-ray fluxes. The lack of correlations suggests that separate emission component are required for the various parts of the spectrum.

The first important point is that although we see no obvious correlations, if the flux in any given wave-band is varying as fast as it varies in the infrared, the observations are not near enough to simultaneous to be certain. Only a concerted campaign of simultaneous observations at each wavelength would resolve this issue. In this study we are not sensitive to shorter time-scales, so even faster variability could in principle be occurring. On the other hand, the longest XMM observations reveals a steady light-curve for over 44 ks, and significant changes are not seen in the individual exposures which make up each optical/infrared observation. (The latter is not very conclusive, however, as the signal in each frame is only small.)

The variability in the optical comes as a surprise, following Hulleman et al's (2000) statement that they saw stability to within 0.02 mag, and Dhillon et al.'s (2005) rough agreement with these magnitudes. The variability is most pronounced in the R-band, and suggests that perhaps there were transitory absorption features (e.g. in the UH88 R-band observation). Beloborodov & Thomson (2006) suggest two likely mechanisms for the optical emission from a magnetar. One possibility is from ions from the outer magnetosphere, which absorb surface radio and microwave radiation at their cyclotron resonance, and re-emit as they head nearer the poles to higher cyclotron energies. A second possibility is coherent curvature radiation from bunched pairs. Both mechanisms can in principle explain the B-band cut-off seen by Hulleman et al. (2004), but both also predict a smooth spectrum at longer wavelengths. These predictions are valid, however, only for the equilibrium state, and how they would be affected by variations of magnetic field and particle kinetic energies is as yet unclear.

Wang et al. (2006) detected 4U 0142+61 in the mid-infrared using *Spitzer*, with fluxes well described as a cool thermal spectrum. They proposed that the K-band emission also arises mainly from a dusty circumstellar fall-back disc at the sublimation radius, which reprocesses incident X-rays. If this were so, one would expect a strong correlation with X-ray flux (with perhaps a time-lag). We see, however, that the X-ray flux varies by much less than the K-band, that there is no variability in the longest (44 ks) XMM observation, and that the pulsed component is roughly stable across the whole epoch. In particular, we see no counterpart in X-rays to the dimming even seen in the K-band.

These measurements relate, however, to only the soft part of the X-ray spectrum, whereas den Hartog et al. (2006; see also Kuiper et al. 2006) have shown from INTEGRAL data that a rising power-law component in the range 20–150 keV dominates the energetics. Due to the low photon-flux and instrumental sensitivity, time resolution of the order of days is not currently possible, and it is unclear whether any variability has been seen in the INTEGRAL observations to date (P. den Hartog, 2006, pers. comm.).

If the infrared emission is magnetospheric in origin (e.g. from cyclotron emission), one would expect it to be varying on the fastest time-scales. This is because the region with cyclotron energies in the infrared range is farthest from the neutron star and thus contains the smallest inertia both in particles and in the magnetic field energy (the latter being dominant). We have shown from the correlation between the infrared magnitudes in KHJ that the component responsible for the variability in K affects also H and possibly J, but is dominant towards the long-wavelength end of the infrared.

The lack of obvious correlations between the various spectral bands comes as another surprise, compared to cases such as that of 1E 2259+586, where the X-ray and infrared decreased on the same time-scale following an outburst (Tam et al. 2004). The latter case may, however, have been a special one, where the normal emission mechanisms were overwhelmed by an extra reservoir of energy which was deposited at the time of the flare. Either the spectral components are truly independent and caused by unique emission mechanisms, the variability is of a larger scale and shorter time-scale than had been previously thought, or there is some hysteresis in the system, which creates a lag between the emission observed in different wave-bands.

It seems clear that in order to understand the variability of this intriguing source, multi-wavelength observations must be made much more frequently than done until now. Nevertheless, a number of hints and interesting relationships seem to be revealing themselves through persistent examination.

Acknowledgments Thanks to Rim Dib and the people at McGill for the RXTE data. Thanks to Shri Kulkarni and Derek Fox for the Keck observations. We made use of data retrieved from the CFHT archive at CADC, from the Subaru archive at SMOKA, and from the XMM archive at XSA. We acknowledge financial support from NSERC.

Chapter 5

Extinction Columns and Intrinsic X-ray Spectra of the Anomalous X-ray Pulsars[1]

5.1 Abstract

The X-ray spectra of Anomalous X-ray Pulsars have long been fit by smooth, empirical models such as the sum of a black-body plus a power law. These reproduce the $\sim$0.5 to 10 keV range well, but fail at lower and higher energies, grossly over-predicting the optical and under-predicting the hard X-ray emission. A poorly constrained source of uncertainty in determining the true, intrinsic spectra, in particular at lower energies, is the amount of interstellar extinction. In previous studies, extinction column densities with small statistical errors were derived as part of the fits of the spectra to simple continuum models. Different choices of model, however, each produced statistically acceptable fits, but a wide range of columns. Here, we attempt to measure the interstellar extinction in a model-independent way, using individual absorption edges of the elements O, Fe, Ne, Mg and Si in X-ray grating spectra taken with *XMM-Newton*. We find that our inferred equivalent hydrogen column density $N_{\rm H}$ for 4U 0142+61 is a factor of 1.4 lower than the typically quoted value from black-body plus power-law fits, and is now consistent with estimates based on the dust scattering halo and visual extinction. For three other sources, we find column densities consistent with earlier estimates. We use our measurements to recover the intrinsic spectra of the AXPs empirically, without making assumptions on what the intrinsic spectral shapes ought to be. We find that the power-law components that dominate at higher energies do not extend below the thermal peak.

5.2 Introduction

The Anomalous X-ray Pulsars (AXPs) are a group of about six young, isolated neutron stars showing pulsations with periods of the order 10 s, whose high-energy luminosity vastly exceeds what is available in rotational energy losses. They are modeled as *magnetars*, their energetics dominated by energy released from a decaying super-strong magnetic field, $\sim 10^{14}$ G externally. See Woods & Thompson (2004) for a summary of current observations

[1] Accepted for publication in ApJ (Durant & van Kerkwijk, 2006a).

and their interpretation in the context of the magnetar model.

Since their discovery, the X-ray spectra of the AXPs have been fitted with simple continuum models, most commonly the sum of a black body, representing the peak of the spectrum around a few keV, and a power law to account for the emission at higher energies. The overall spectra are relatively soft, as indicated by high power-law indices. In the fitting process, the interstellar extinction is estimated as well, by including a multiplicative term to take account of the absorption of all elements, parameterized by the hydrogen column density, $N_{\rm H}$.

While these smooth continuum spectral models reproduce the spectra of all AXP well in the range observed by satellites such as *Chandra*, *XMM* and *ASCA* (roughly 0.5 to 10 keV), their extrapolation fails at both higher and lower energies. At energies from tens of keV to $\sim$1 MeV, Kuiper et al. (2004) and Den Hartog (2006) found from RXTE/HEXE and Integral observations that much harder power-law components are present, which dominate the total energetics. In the optical and infrared, the first detections of AXPs made by Hulleman et al. (2000, 2001) already showed that while the optical and infrared emission is only a tiny part of the energy budget, it is well below (by orders of magnitude) the extrapolation of the X-ray spectra dominated by the power law, yet well above the extrapolation of just a blackbody component. Thus, the optical and infrared emission also appears to require a separate emission component. More recently, the situation was complicated even further, when Wang et al. (2006) found from mid-infrared observations from *Spitzer* that at least one of the AXPs (4U 0142+61) shows evidence of a circumstellar dusty disc.

The above discrepancies led us to wonder whether the measurements of interstellar extinction were reliable. These are particularly sensitive to the the low-energy (<500 eV) part of the spectra (where the absorption is highest), and one would expect that they would depend strongly on the assumed model for the intrinsic emission. For instance, the above-mentioned model consisting of a black-body and a power-law component rises towards lower energies, while a model of, say, two black-body components, would turn over. Thus, to match a given observation, the former would require a larger column density than the latter.

From previous studies (see Table 5.1), it is indeed clear that the inferred column density $N_{\rm H}$ depends strongly on the assumed intrinsic model, with the differences in $N_{\rm H}$ for different models fitted to the same spectrum far exceeding the statistical uncertainty obtained for any given one. Clearly, without knowing the intrinsic shape of the spectrum, one cannot measure the extinction accurately, and, conversely, without knowing the extinction independently, one can obtain only little information about the true intrinsic spectrum.

Another clue that the extinction is not estimated correctly, and hence that the models used for the intrinsic spectrum are incorrect, comes from variability studies. AXP spectra have been seen to vary both from one epoch to another, and between phase bins (e.g., Woods et al. 2004; Rea et al. 2005), and, generally, different values of $N_{\rm H}$ are found for these different spectra (see Table 5.1). Although an intrinsic, variable contribution to the extinction is not impossible in light of the discovery of a possible debris disk around 4U 0142+61 (Wang et al. 2006), it seems unlikely, especially on the time-scale of seconds. Indeed, discrepancies in fitted parameters obtained from spectra taken with different instruments, which are often blamed on poor cross-calibration, could well be purely an artifact of the fitting process, with differences in sensitivities leading to differences in weight as a function of energy, and hence

Table 5.1. Hydrogen column densities towards the AXPs inferred using different models.

Object	Telescope/ instrument	PL	PL+BB	BB+BB	BR	BR+BB	Reference
		Model[a]					
4U 0142+61	XMM/EPIC	···	0.96	···	0.82	0.68	Göhler et al. (2004)
	Chandra/HETGS	1.43:	0.88	···	0.92	0.69	Juett et al. (2002)
	ASCA/SIS,GIS	···	0.95	···	···	0.90	White et al. (1996)
1E 2259+586	XMM/EPIC	···	0.94-1.10[b]	···	···	···	Woods et al. (2004)
	Chandra/ACIS	···	0.93	···	···	···	Patel et al. (2001)
	ASCA/PSPC	1.14:	0.85	0.63	0.8	···	Rho & Petre (1997)
1E 1048.1−5937	XMM/EPIC	···	0.95-1.10[b]	0.55-0.67[b]	···	···	Tiengo et al. (2005)
	BeppoSAX/LECS	1.54:	0.45	0.14	···	···	Oosterbroek et al. (1998)
1RXS J170849.0	BeppoSAX/LECS	···	1.3-1.7[c]	···	···	···	Rea et al. (2005)
−400910	BeppoSAX/LECS	···	1.1-1.6[c]	···	···	···	Rea et al. (2003)

Note. — Column Densities are in units ($10^{22}\,\mathrm{cm}^{-2}$). For all models listed, the reduced χ^2 of the fits was less than 2 (those marked with colons are relatively poor fits).

[a]Acronyms are PL: Power Law, BB: Black Body, BR: Bremsstahlung.

[b]Ranges represent measurements made at different epochs. One does not expect the column density to vary with time (see text).

[c]Range represents measurements in different phase bins. Again, one would not expect the column density to vary with rotational phase.

different values for the parameters, including the extinction.[2]

From a physical perspective, it is not clear why there should be a power-law component in the spectra of AXPs. Recent physical models, such as those presented by Lyutikov & Gavriil (2006) can account for a power-law like high-energy tail, but do not predict a soft part. In these models, the blackbody surface flux is modified by interactions in the outer atmosphere or magnetosphere, for example through the inverse-Compton scattering of photons off high-energy particles. This creates an extended high-energy tail but leaves the spectrum at low energies (the Rayleigh-Jeans side of the blackbody spectrum) unaffected.

Absorption in the interstellar medium of X-ray photons is primarily by the photo-electric capture by electrons in inner shells of metals and helium. Since the creation of X-ray absorption models (Morrison & McCammon 1983; Balucinska-Church & McCammon 1992), great advances have been made in our understanding of absorption edge structure and energies (e.g., Juett et al. 2003), largely driven by the improved resolution and sensitivity of X-ray observatories. We are also beginning to understand more about interstellar abundances (e.g., Lodders 2003; but see §5.5 below). With these advances, it is now possible to measure individual elemental absorbing columns to a source independently, and so recover the intrinsic

[2]Another source of differences may be the use of different sets of cross-sections and abundances; see, e.g., Weisskopf et al. (2004).

spectrum without further assumptions.

In this paper, we measure the extinction to the four best-studied AXPs by analyzing the individual absorption edges present in the sensitivity range of XMM/RGS, and use this to derive intrinsic X-ray spectra for each AXP, as well as to estimate reddenings at optical and infrared wavelengths. In §5.2, we present the data sets we use and their reduction. We describe in §5.3 how we infer individual element column densities, and what atomic data we use. In §5.4, we use Monte-Carlo simulations to estimate the uncertainties of our measurements. We present our results in §5.5, and show de-extincted X-ray spectra in §5.6. We continue by deriving optical extinctions for all sources in §5.7, and discussing the overall spectral energy distribution of the best-studied source, 4U 0142+61, in §5.8. We briefly summarize our results and look forward to future work in §5.9.

5.3 Data Reduction

We searched the *XMM-Newton* archive for observations of all the AXPs. The *XMM-Newton* observatory (Jensen, 1999) provides data from three separate telescopes simultaneously, but in this work we are concerned with the Reflection Grating Spectrometer (RGS) instruments (den Herder et al. 2001), which provide high-resolution spectra in the range 6–40 Å. We found a number of long observations for the four brightest AXPs[3] (see Table 5.2; we omitted shorter data sets with few counts). For all these, RGS is used with the same instrumental setup, thus ensuring a fair comparison of the sources. We also searched for high-resolution spectra taken by *Chandra*, but found only a few observations. Since these did not allow a comparison between sources, we decided not to use these in the present work.

We reduced the raw data (Observation Data Files or ODFs) with the 20041122 version of the analysis software, XMM-SAS, and calibration files. We used the pipeline products for the data from the European Photon Imaging Cameras, EPIC (Strüder et al. 2001; Turner et al. 2001; these were used only as additional information for the RGS reduction, see below).

A light curve was produced with 10-s bins from the EPIC data. These showed periods of high background (*flaring*), and such periods were excised from the RGS analysis using Good Time Intervals (GTIs). The EPIC data was also used for source selection, using the automated source detection algorithm. This only works for imaging modes, but fortunately there are three imaging instruments (EMOS1, EMOS2, EPN), and out of these only one is required. The co-ordinates of the brightest source were used to extract the RGS spectra. This eliminates any uncertainties arising from the telescope pointing and bore-sight correction, since the relative alignment of the telescopes and instruments is well known.

Final spectra were obtained by subtracting the background and then converting to flux using the XMM-SAS task `rgsfluxer`. For our spectral modeling, we decided to bin to a relatively low resolution (0.1 Å), since the errors associated with bins with few or no counts is uncertain. We kept a large number of bins in the spectra and response matrix functions until the final fluxing, as recommended in the documentation. The documentation also states that `rgsfluxer` fluxes are not recommended for final scientific analysis, but for the relatively low resolution we use and the relatively poor signal-to-noise ratio of our data, the accuracy is ample.

[3]For the AXP 1E 1841-045, two short XMM observations exist, but we found these contained too few counts to provide reliable measurements.

Table 5.2. Data sets used.

Object	Dataset[a]	Date	Exp.[b] (ks)	Counts[c] (1000)
4U 0142+61	0206670101	2004-03-01	44.1	98.5
	0206670201	2004-07-25	23.9	62.6
1E 2259+586	0038140101	2002-06-11	52.5	20.2
	0155350301	2002-06-21	29.0	22.8
1E 1048.1−5937	0147860101	2003-06-16	69.0	2.3
	0164570301	2004-07-08	33.9	4.6
	0307410201	2005-06-16	23.3	3.4
	0307410301	2005-06-28	25.9	2.6
1RXS J170849.0−400910	0148690101	2003-08-28	44.9	11.2

[a]XMM Science Archive identifier

[b]Exposure time for the RGS instruments only; typically shorter than the total observation time.

[c]In both RGS instruments, in two orders, after good-time-interval filtering and background subtraction.

In order to improve the signal-to-noise ratio, we decided to merge the spectra from different observations of each object into averaged spectra. Here, we must raise two caveats. The first is that some AXPs – 1E 1048.1−5937 in particular – are variable, and the spectral shape may be different in each observation. This, however, should not change our column estimates, since we fit in small spectral regions around each absorption edge. The second caveat is that the amount of extinction to the continuum source might vary if some of it is intrinsic. This seems unlikely, but is perhaps not impossible given the discovery by Wang et al. (2006) of a likely debris disc around 4U 0142+61 (although from broad-band observations there has been no clear evidence for changes in extinction). Unfortunately, our individual datasets do not have enough signal to verify this.

Finally, we note that for 1E 2259+586 there is enhanced background emission due to the supernova remnant surrounding the AXP. From the pipeline-produced *order images*, however, we find that the spectrum of the central source remains distinguishable and that there are no significant background lines which might contaminate it. The increased background does, however, lead to poorer signal-to-noise where the AXP flux is low.

5.4 Analysis

For our measurements, we assume that is is possible to find small regions of a spectrum around an absorption edge, over which the intrinsic spectrum is continuous and well-described by a power-law. To each spectral region of interest, we fit a function of the form

$$F_\lambda = A \times \left(\frac{\lambda}{\lambda_{\rm edge}}\right)^\alpha \times \begin{cases} 1 & \text{for } \lambda > \lambda_{\rm edge} \\ \exp\left[-\left(\frac{\lambda}{\lambda_{\rm edge}}\right)^{5/2} \times N\sigma\right] & \text{for } \lambda \le \lambda_{\rm edge} \end{cases} \tag{5.1}$$

In the fits, the edge wavelength $\lambda_{\rm edge}$ and photo-ionization cross-section at the edge σ were kept fixed, but the normalization A, power-law index α and the column density N were allowed to vary. Note that the value of the power-law index which attenuates the cross-section with wavelength here is not the more familiar 3. The value of 2.5 fits better with theoretical calculations (e.g., Verner & Yakovlev 1995). We note that the fits below are insensitive to this change, and negligible additional uncertainty is incurred.

We used theoretical photo-electric cross-sections from Gould & Jung (1991), since cross-sections are very hard to measure accurately. From recent high-resolution X-ray spectroscopy (see below), we know of several narrow features and additional structure in some of the edges. In contrast to the overall strength of the ionisation edges, the strengths of these additional features depend on the degree of ionisation along the line of sight. Since we do not have enough signal to fit for these, we instead mask any affected points. The spectral ranges to fit around each edge were chosen by balancing the requirement of enough data points for robust fits with that of the intrinsic spectra being well described by power-law form.

For the Oxygen-K edge ($\sigma = 5.642 \times 10^{-19}\,{\rm cm^{-2}}$), we fitted the range 19–26 Å and used $\lambda_{\rm edge} = 23.1$ Å, as found by Takei et al. (2002). We masked the regions 22.5–23.1 Å for multiple edges, and 23.25–23.6 Å for narrow lines.

For the Iron-L edge(s) ($\sigma = 4.936 \times 10^{-19}\,{\rm cm^{-2}}$), we fitted the 16–19 Å range and used an edge wavelength of 17.52 Å, following the work of Juett et al. (2006, in prep.). There are no sharp absorption features, but the edge has multiple components, leading to a complex shape around the edge. Accordingly, we masked the range 17.2–17.56 Å.

In the case of the Neon-K edge ($\sigma = 3.523 \times 10^{-19}\,{\rm cm^{-2}}$), we fitted the range 13–16 Å and used $\lambda_{\rm edge} = 14.31$ Å following once more the work of Juett et al. Three narrow absorption features fall into the fitting range, which we excluded by masking 14.44–14.66 Å and 13.4-13.5 Å.

The Magnesium-K edge ($\sigma = 2.191 \times 10^{-19}\,{\rm cm^{-2}}$) is the only one in our sample which shows no complicated features. We used $\lambda_{\rm edge} = 9.5$ Å, as found by Ueda et al. (2005), and fitted in the range 8.5–10.5 Å.

Finally, for the Silicon-K edge ($\sigma = 1.476 \times 10^{-19}\,{\rm cm^{-2}}$), we once more used the work of Ueda et al., fitting in the range 6.2–7.5 Å and using $\lambda_{\rm edge} = 6.72$ Å. We masked the region 6.61–6.73 Å for edges of silicon in silicates, which are slightly shifted from the edge for atoms in isolation.

5.5 Fitting Method and Error Determination

For each edge, we fit the data with the model in Eq. 5.1, with $\lambda_{\rm edge}$ and σ fixed to the values given above, and the best values of A, α, and N found by χ^2 minimization. For the uncertainties on each data point, we use the errors given by `rgsfluxer`.

There are two possible problems with our fitting method. First, the uncertainties produced by `rgsfluxer` are known to be poorly defined for faint sources. This is because in the high-resolution input spectra (which are rebinned to our 0.1 Å bin size in `rgsfluxer`), bins with zero counts are assigned an arbitrary uncertainty of 1, when the expectation value for the (faint) source might genuinely be near zero and hence the associated uncertainty should be smaller as well. These assigned errors are propagated, and, as a result, the uncertainties on the rebinned fluxes are greatly overestimated, leading to values of reduced χ^2 far smaller than unity in our fits. The second possible problem, related to this, is that for these counting data, it would be more appropriate to use the Cash statistic rather than χ^2, since the probability distribution is Poissonian rather than Gaussian.

Fortunately, in practice these problems are not severe. In a given fitting region, we find that in our 0.1 Å bins both the number of counts and the `rgsfluxer` uncertainty are roughly constant. Thus, even though the given errors are over-estimated, this effect is roughly equal for each point and hence it does not effect the best-fit parameters. Furthermore, the bins we use are sufficiently wide that they contain many counts, and hence the assumption of Gaussian uncertainties is not so bad. Indeeed, fits made by minimizing the Cash statistic led to results very close to those found through the χ^2 method. We preferred not to use them generally, however, since with the Cash minimization our fitting routine converged much less robustly to the global best fit.

In order to estimate the uncertainties on our measurements, we have conducted Monte-Carlo simulations, in which we produce simulated data sets which we fit in the same manner as the real data. We employed two different methods for simulating the data. In the first, we used *bootstrapping,* i.e., we produced simulated data sets with the same number of points as the actual data set by drawing randomly, with replacement, from the actual (λ, F_λ) pairs (Press et al. 1992). In the second method, we simulated data sets based on the best-fit model, adding Gaussian noise with a variance equal to the variance of the real data around that model. Both methods gave consistent results after 1000 trials and the spread of results in the one parameter of interest (the column depth), was well-described by a Gaussian in every case. The one-sigma confidence region was taken to be the region enclosed by the 16th and 84th percentile and these are listed in Table 5.3.

We note that in some cases, in particular for 1E 1048.1−5937, the uncertainties even for the best measurements are similar to the measurements themselves, i.e., the measurements of the indivual columns are not significant. In evaluating this, however, one should keep in mind that we know *a priori* the locations and shapes of the absorption edges (from high signal-to-noise measurements of brighter sources; see §5.3). Being in the Galactic plane, interstellar extinction is inevitable, and our aim is not to prove the existence of the features, but just to measure the strength of features known to be present. Thus, the measured column densities and associated uncertainties can be used as given, and, in particular, columns from different elements can be combined to give a more significant overall measurement of the extinction.

Finally, possible sources of systematic error ought to be mentioned. First, we have chosen to fit the spectral sections with a power law. This should not be a large source of additional uncertainty, since our wavelength ranges are so small – $\Delta\lambda/\lambda = 0.2 \ldots 0.3$ – that a power law should be a good approximation for any smooth continuum. Indeed, the fit would be much better constrained if we could use larger wavelength range, but this would require

Table 5.3. Column densities found for each AXP

AXP	O K ($10^{17}\,\mathrm{cm}^{-2}$)	Fe L[a] ($10^{17}\,\mathrm{cm}^{-2}$)	Ne K ($10^{17}\,\mathrm{cm}^{-2}$)	Mg K ($10^{17}\,\mathrm{cm}^{-2}$)	Si K[a] ($10^{17}\,\mathrm{cm}^{-2}$)
4U 0142+61	28.8 ± 4.5	0.7 ± 1.4	5.3 ± 1.3	2.2 ± 0.5	2.0 ± 2.7
1E 2259+586	...	13 ± 6	9 ± 4	3.6 ± 1.4	0.6 ± 3.6
1E 1048.1−5937	...	...	7 ± 7	2.7 ± 2.4	11 ± 7
1RXS J170849.0−400910	...	...	15 ± 5	2.9 ± 1.8	2 ± 5

Note. — No value is shown in cases where no reliable fit was possible.

[a]We list the results for Fe L and Si K for completeness only. As discussed in the §5.4, we believe these are less reliable.

knowledge of what the intrinsic spectrum ought to be. Second, the optical depth in an edge does not in general have the simplistic form given in Equation 5.1 - the form is different for every ionisation stage of every element. Fortunately, the equivalent width of the resulting feature – and thus the total column – is not sensitive to such details, since it depends on the total cross section. Third, the masking of certain wavelengths due to complicated near-edge structure is not necessarily the best approach, but the alternative – fitting for them – would not be better, since the details of the strengths of the lines depends upon the (unknown) ionization balance along the line of sight; hence, any gain in number of data points included in the fit would be offset by the required additional parameters.

5.6 Results

In Table 5.3, we list the inferred columns for each object, and in Figure 5.1, we show the fits overlaid on the data points, for those objects where a reasonable fit was possible. Note that while points with zero or negative flux were included in the fit, they do not show up in the figures (since the scales are logarithmic).

From the figures and the table, one sees that the values for iron and silicon are in every case uncertain, due to the low flux and low optical depth for the former and the low sensitivity and relatively poor calibration of the RGS at short wavelengths for the latter. Since they do not add information, we will not use these results any further.

For Neon and Magnesium, we find fair measurements for all sources, and one sees that their relative abundances are roughly consistent from one source to another. 1RXS J170849.0−400910 appears to be an exception to this, its magnesium to neon ratio being relatively high, but with the large uncertainties for this highly reddened source, they are still consistent within the errors. From the columns given, it is immediately clear that 4U 0142+61 is least extincted, followed by 1E 1048.1−5937, 1E 2259+586 and 1RXS J170849.0−400910.

We list in Table 5.4 the implied Hydrogen column densities for each source, for each reliably measured photo-electric edge. Here, we use the abundances of Asplund et al. (2004);

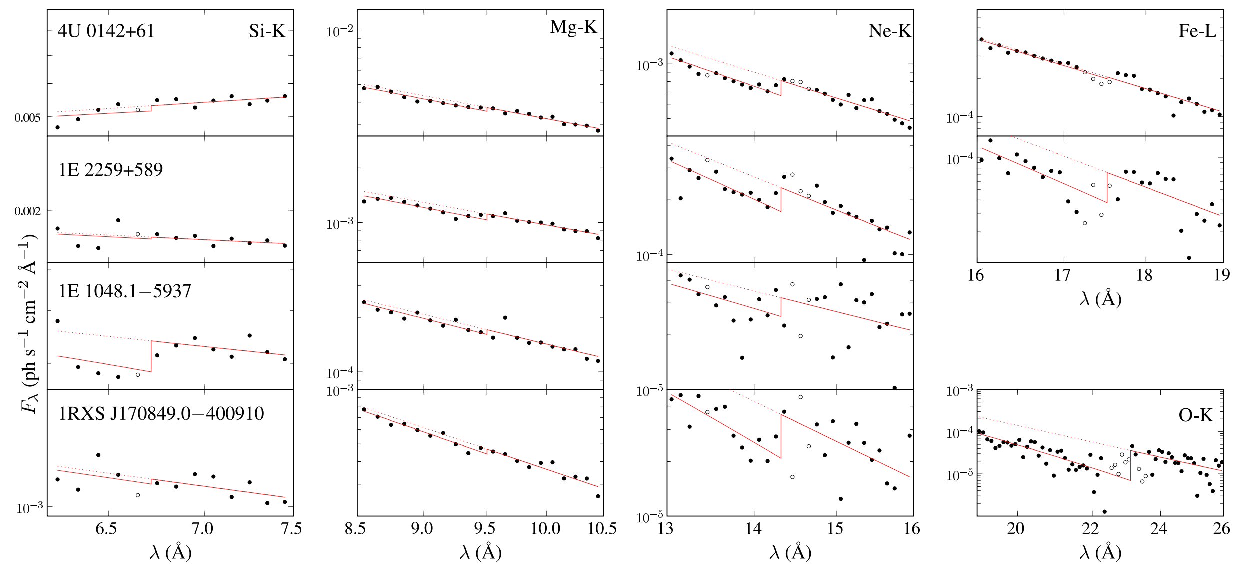

Figure 5.1 Fits obtained for the Si-K, Mg-K, Ne-K and Fe-L edges (left to right), with the O-K edge for 4U 0142+61 only in the lower-right. Open circles have been excluded from the fit, due to complex edge structures or narrow features. For each edge, the scales span the same factor in flux for the different AXPs. As discussed in the §5.4, we do not use iron or silicon in determining the average extinction, since these results are less reliable.

we discuss this further below. Also listed are the weighted means of the column densities.

Comparing our results with those found through broad-band fits using assumed intrinsic models (Table 5.1), one sees that the values are consistent with the ranges found previously. Unfortunately, for all sources but 4U 0142+61, our uncertainties are too large to distinguish between different models. For 4U 0142+61, however, our value of $N_{\rm H}$ is well determined, and we find it to be lower by a factor 1.4 than the value inferred from the commonly used black-body plus power-law model, and closer to that found using the model consisting of two black bodies. Interestingly, this is also the source for which White et al. (1996) found a discrepancy between the extinction and the brightness of its X-ray scattering halo, while Hulleman et al. (2004) found a discrepancy between X-ray extinction, as inferred from the black-body plus power-law model, and optical reddening. With our new value, the different measurements are all consistent.

In the sections below, we will use our $N_{\rm H}$ values to derive intrinsic spectra and optical extinctions. Before doing so, it is worth stressing that while we quote values of $N_{\rm H}$, our measurements are of the Neon and Magnesium (and Oxygen for 4U 0142+61) column densities. Thus, the accuracy with which we can determine columns of a given other element (or dust) depends not only on our statistical uncertainty, but also on the uncertainty on the abundance of that element relative to Neon and Magnesium (as well as on possible corrections for the extent to which a given element is locked up in optically thick dust; e.g., Wilms et al. [2000]; for a general caution on the implications of the set of abundances used, see Weisskopf et al. [2004]).

In general, the relative abundances of refractive elements are known precisely from studies of meteorites, but those of the volatiles are much more uncertain, as has recently become apparent again from the controversy on the abundances of Oxygen and Neon. Briefly, Asplund et al. (2004) inferred from improved models for the solar atmosphere that the solar Oxygen and Carbon abundances were much lower than thought previously. The revised abundances, however, led to discrepancies between helioseismology and models for the solar interior (e.g., Schmeltz et al. 2005). To remedy this, it has been suggested that the abundance of Neon might have to be revised upwards (e.g., Bahcall et al. 2005), but this leads to a number of other problems (e.g., Young 2005; Drake & Testa 2005).

From our data, an increased Neon abundance seems unlikely: the value of the Neon to Magnesium ratio we find, Ne/Mg $= 2.4 \pm 0.7$, is much closer to the solar-abundance value of 2.0 from Asplund et al. (2004) than the value of 5.8 hypothesised by Bahcall et al. (2005) for consistency with helioseismology. For Oxygen, we have only one measurement, for 4U 0142+61, which gives O/Mg $= 13.1 \pm 3.6$. This is also much closer to the revised solar abundance of 13.5 of Asplund et al. (2004) than the old one of 22.4 listed by Anders & Grevesse (1989).[4]

Given the above, we are fairly confident that for columns of other refractive elements (or of dust), any additional uncertainty beyond the statistical one is small. However, we are less confident for the abundances of Hydrogen, Helium, Carbon, Nitrogen, and Oxygen. This will affect our corrections for extinction below, especially at low energies.

5.7 Intrinsic Spectra

The main question underlying this work is the nature of the intrinsic spectra of AXPs. As discussed in §5.1, different simple models reproduce the spectral data equally well, and they do not allow one, e.g., to distinguish between spectra that rise or fall with wavelength at long wavelengths. With the column densities obtained above, we can de-extinct the observations to find the intrinsic spectra empirically. For this purpose, rather than attempt to model the extinction in detail (e.g., Wilms et al. 2000), we will use a simplified model that can be described and reproduced easily; this will be sufficient to answer the main question, whether the intrinsic spectra rise or fall at long wavelengths.

For the extinction correction, we convert the average Hydrogen column densities $\langle N_{\rm H} \rangle$ from Table 5.4 to individual columns for Oxygen, Iron, Neon, Magnesium, and Silicon (using the abundances of Asplund et al. [2004]; see Table 5.4 for O, Ne, Mg; furthermore, $N_{\rm Fe} = 2.8 \times 10^{-5}\, N_{\rm H}$, $N_{\rm Si} = 3.2 \times 10^{-5}\, N_{\rm H}$), and correct the spectra for the contribution of each of these using the simple edge model from Eq. 1 and the cross sections given following that equation. Furthermore, we take into account the absorption by lighter elements, in particular Helium, Carbon, and Nitrogen, with an additional component $\exp[-\tau_{25}(\lambda/25\,\text{Å})^{\beta}]$, where τ_{25} is the optical depth at 25 Å. Inspired by the behaviour of the total cross-section shown in Fig. 1 of Wilms et al. (2000), we choose $\beta = 3$; it is intermediate between the steeper decrease of the cross-sections of Helium and Hydrogen at these energies and the shallower one for Carbon and Nitrogen. For the scaling, we use the relation given by Morrison & McGammon (1983), $\tau_{25} = 7.6 \times 10^{-22}\, N_{\rm H}$.

[4]The good match to the solar abundances is perhaps surprising, given the discrepant abundance rations found in other recent X-ray spectroscopic studies (N. Schultz, 2005, personal comm.); it may be a consequence of the fact that AXPs are not affected by binary interactions.

Table 5.4. Inferred Hydrogen column densities and amounts of visual extinction

AXP	$N_{\rm H}$(O K)	$N_{\rm H}$(Ne K)	$N_{\rm H}$(Mg K)	$\langle N_{\rm H}\rangle$	A_V
Abundance[a]	4.6×10^{-4}	6.9×10^{-5}	3.4×10^{-5}		
4U 0142+61	0.60 ± 0.09	0.77 ± 0.19	0.65 ± 0.15	0.64 ± 0.07	3.5 ± 0.4
1E 2259+586	···	1.23 ± 0.58	1.06 ± 0.41	1.12 ± 0.33	6.3 ± 1.8
1E 1048.1−5937	···	1.0 ± 1.0	0.8 ± 0.7	0.87 ± 0.57	4.9 ± 3.2
1RXS J170849.0−400910	···	2.1 ± 0.7	0.9 ± 0.6	1.4 ± 0.4	7.7 ± 2.2

Note. — All column densities $N_{\rm H}$ are in units of $10^{22}\,{\rm cm}^{-2}$. Column $\langle N_{\rm H}\rangle$ is the weighted mean of all measurements. For previous determinations of the hydrogen column density, from broad-band spectral fits, see Table 5.1. A_V is the extinction (in magnitudes) in the V-band; the errors listed are statistical only, and do not include systematic uncertainties in the conversion from $N_{\rm H}$. The $N_{\rm H}$ values themselves do not include several possible systematic errors (see §5.6).

[a]Elemental abundance $N_{\rm O,Ne,Mg}/N_{\rm H}$ used to convert from the measured column from Table 5.3 to the equivalent Hydrogen column listed here. See §5.3 and 5.5 for details.

The main systematic uncertainty in our correction is due to the relative abundances, in particular for Oxygen and for the lighter elements represented by τ_{25} (see §5.5). The latter uncertainty could be quite large: for example, calculating τ_{25} from the abundances and cross-sections in Morrison & McCammon (1983), one gets a correction ∼1.7 times larger – and thus 1.7 times larger implied intrinsic flux – than by using those in Wilms et al. (2000). This discrepancy, however, reduces rapidly with decreasing wavelength, and does not alter the shape of the spectra by much (at least on the logarithmic scale on which they are shown).

In Fig. 5.2, we show the observed (circles) and de-extincted (triangles) spectrum of 4U0142+61: all the edges apparent in the observed spectrum have been removed in the corrected spectrum (though discrete features are still evident, such as those due to the multiple edges of iron at 17.5 Å). From the de-extincted points, it is clear that the de-extincted spectrum falls with wavelength at longer wavelengths.

In order to see how it might have been possible to infer a rise at longer wavelengths from broad-band data, we also show the spectrum de-extincted with $N_{\mathrm{H}} = 9.5 \times 10^{21}\mathrm{cm}^{-2}$ (crosses), as found by White et al. (1996) from *ASCA* data, and overdraw their fit of the sum of a power-law and black-body (upper curve) and this same model extincted by their value of the hydrogen column (lower curve).[5] One sees from the Figure that, qualitatively, their fit is not unreasonable, so the source has not varied much. Looking in detail, however, especially near the Oxygen edge, it is clear that their column density is too high, and that the data are inconsistent with a intrinsic spectrum rising at long wavelengths.

In Fig 5.3, we show the de-extincted spectra derived for all four AXPs under consideration. Two things are immediately apparent: they are not consistent in shape with one-another, and there is no continuation at long wavelengths of any power-law component representing the emission at $> 2\,\mathrm{keV}$: the photon indices, measured from power-law plus black-body fits, of 2.4 to 4.0 correspond to slopes of $\alpha = -0.6$, -0.1, 0.4, and 1.0 ($F_\lambda \propto \lambda^\alpha$), for 1RXS J170849.0−400910, 1E 1048.1−5937, 4U 0142+61, and 1E 2259+586, respectively, while the spectra shown have indices of approximately $\alpha = -3$, -2, -2, and 0 (if the low-energy tail is taken to be a power-law). Note that the largest cause of uncertainty in these derived spectra are the uncertainties in the column depths of the individual edges, rather than abundances, detector response or photon statistics. However, the conclusion that any power-law component at short wavelengths does not continue to long wavelength is robust.

The above result raises a paradox: How can it be that even for the sources other than 4U 0142+61, for which the equivalent hydrogen columns N_{H} we determine are consistent with those from power-law plus black-body fits, we do not see the power-law component at long wavelength? The answer lies in the fact that the low-energy region is actually not reproduced all that well in typical fits to broad-band spectra, but this may not be noticed in the formal χ^2 since it has relatively few counts and thus carries little weight (if it is included at all). For a good example of this, see Fig. 2 in Woods at al. (2004): below 0.75 keV, the data lie systematically ∼20% above the model (particularly easy to see in this figure, since it has a panel with the ratio of the data to the model, rather than the usual, less instructive χ residuals). With relatively few counts and larger uncertainties, these points do not affect much the overall χ^2, but clearly (by eye) they are not well described by the model (and indeed a bad fit would likely have been found if the data had been binned more heavily).

[5] White et al. (1996) used the cross-sections of Morrison & McCammon (1983) in calculating extinction, so we have used this also in this instance only, for consistency.

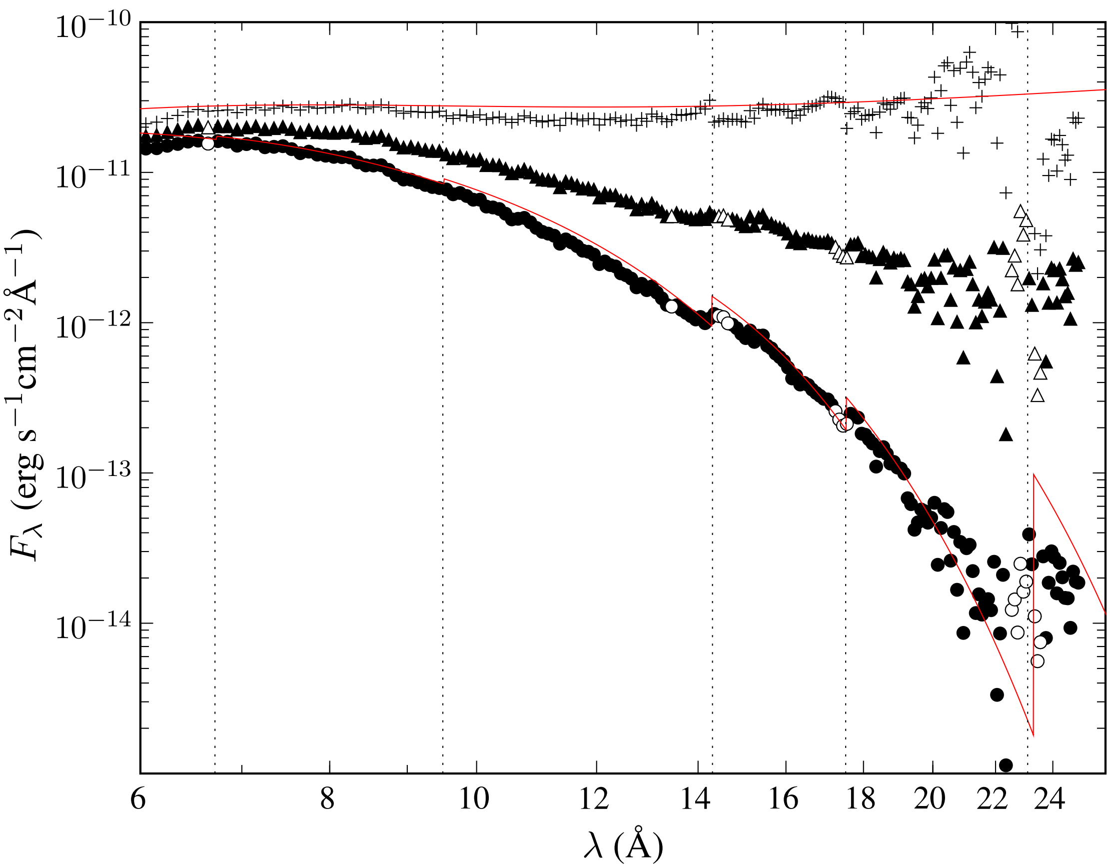

Figure 5.2 Spectra of 4U 0142+61 as observed (circles), de-extincted with the $N_{\rm H}$ found in this work and the abundances as described in the text (triangles) and de-extincted using Morrison & McCammon's cross-sections and $N_{\rm H} = 9.5 \times 10^{21}\,{\rm cm}^{-2}$ (crosses). Open symbols indicate points affected by lines and other structure near the different edges. The over-drawn solid lines are the models of White et al. (1996) that best fit their broad-band *ASCA* data (see text). Vertical lines show the locations of the Si-K, Mg-K, Ne-K, Fe-L, and O-K photo-electric absorption edges.

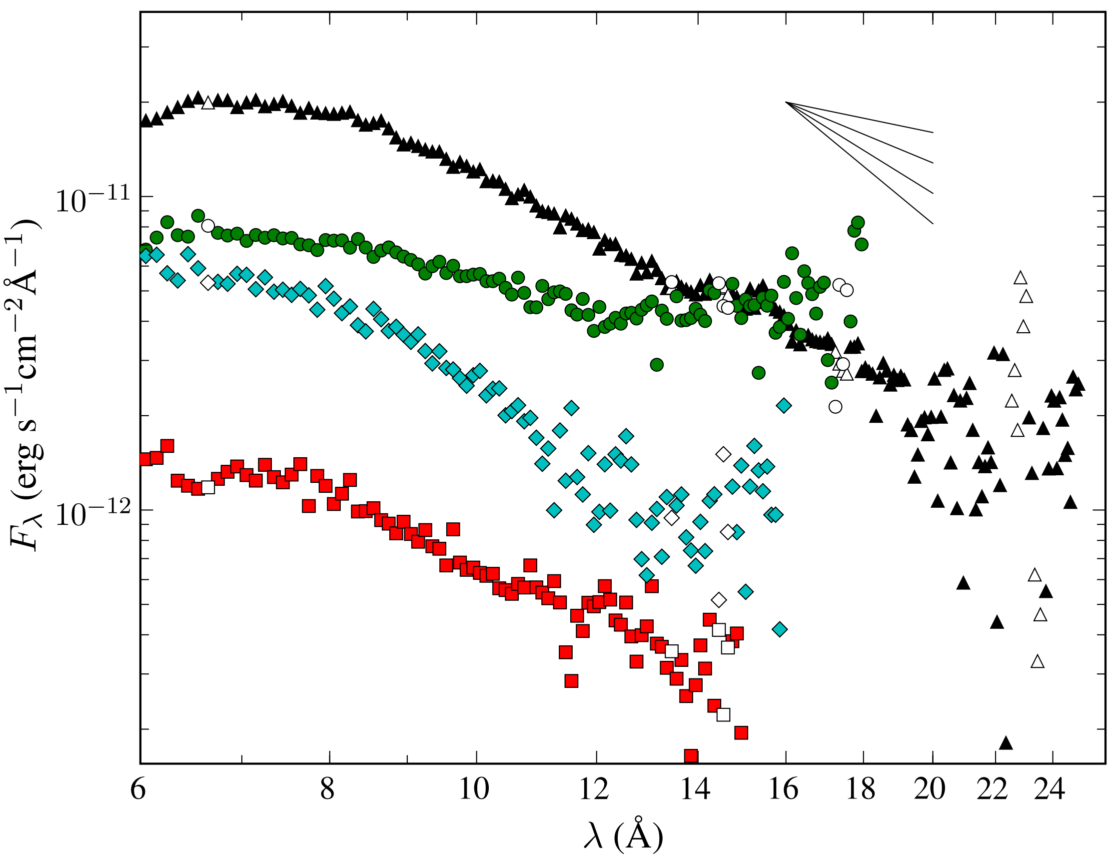

Figure 5.3 Spectra for each AXP, de-extincted with the column densities and continuum extinction found in the text. Black triangles are 4U 0142+61, green circles 1E 2259+586, red squares 1E 1048.1−5937, and cyan diamonds 1RXS J170849.0−400910. Open symbols are affected by absorption edge structure and absorption lines (see text). The spectra have been truncated where the signal-to-noise ratio per bin decreases below about 1. Also shown are power laws ($F_\lambda \propto \lambda^\alpha$, $\alpha = -1, -2, -3, -4$) to guide the eye.

While at long wavelengths there is no evidence of continuations of short-wavelength power-law components, the spectra also do not decline as fast as would be expected if they were due to a black-body component. If the thermal emission arises from the neutron-star surface, as seems likely, this might simply reflect a range of temperatures on the surface. Alternatively, it may indicate that more realistic models are required to describe the emission, which also include the effects of magnetic field, interactions with high-energy particles in the magnetosphere, and gravitational light-bending (the latter particularly important for phase-resolved spectra).

Finally, looking in detail at the spectra, it appears that for 4U 0142+61, there is a hint of a feature in the spectrum at about 13.5 Å (this is easier to see in Fig. 5.4 at around 2×10^{17} Hz). One could interpret this either as a broad absorption feature at ~ 13.5 Å, or a broad emission feature at ~ 15 Å. Assuming it is cyclotron absorption (emission), i.e., $E_{cyc} = \hbar eB/mc$, this corresponds to 7.9×10^{10} G (7.1×10^{10} G) for electrons or 1.5×10^{14} G (1.3×10^{14} G) for protons. If the line is red-shifted, the inferred magnetic field strength would increase by a factor $1 + z_{\rm GR} = (1 - 2GM/Rc^2)^{-1/2}$, equal to ~ 1.3 at the surface (for a neutron star with $M = 1.4\,M_\odot$ and $R = 10$ km). Intriguingly, the value for proton cyclotron lines is close to the magnetic dipole field strength inferred from timing measurements, $B_{\rm dip} = 3.2 \times 10^{19}\sqrt{(P\dot{P})} = 1.3 \times 10^{14}$ G (Woods & Thompson 2004).

5.8 Optical extinction

Our revised X-ray extinction measurements also allow us to estimate the extinction in the optical and infrared. For this purpose, we use the relation between the Hydrogen column $N_{\rm H}$ and visual extinction A_V derived by Predehl & Schmitt (1995): $A_V = 5.6(N_{\rm H}/10^{22}\,{\rm cm}^{-2})$ mag. The resulting values of A_V are listed in Table 5.4. Here, the errors on A_V listed are statistical, i.e., they do not include the uncertainty in the conversion factor. The latter uncertainty could be fairly large, both because there is substantial scatter in the measurements used by Predehl & Schmitt, and because their sample had typically lower values of extinction. Furthermore, their hydrogen column is not measured directly, but is based on X-ray extinction measurements and thus a measure of elements which contribute significantly to absorption in X-rays, i.e., Carbon, Oxygen, Neon, and Magnesium. The latter should not be a problem in our case, however, since we measure some of the same elements in Predehl & Schmitt's sensitivity range (they did not have the spectral resolution to measure individual absorption edges), and thus systematic effects in converting to $N_{\rm H}$ should cancel. The only caveat is that we used the revised solar abundances of Asplund et al. (2004), while Predehl & Schmitt used, implicitly, the old solar abundances. For Neon and Magnesium, however, the abundances have not changed, while the change for Oxygen should not have a large effect, since for the one case where we measure it – for 4U 0142+61 only – the inferred $N_{\rm H}$ is consistent with the values inferred from Neon and Magnesium (see Table 5.4).

While the above indicates one should be somewhat careful in using the absolute values of the reddening, the relative reddenings should be much more accurate, since any systematic uncertainties in the conversion should be similar from source to source. Our results indicate that in order of increasing reddening, the AXPs are 4U 0142+61, 1E 1048.1−5937, 1E 2259+586 and 1RXS J170849.0−400910.

We can compare our revised estimates with earlier work. First, for 4U 0142+61, Hulleman et al. (2004) found from the colors of field stars, that the reddening along the line of sight was likely substantially lower than the value $A_V = 5.1$ inferred from the literature values of $N_{\rm H}$ for the power-law plus black-body model. Our new value of $A_V = 3.5 \pm 0.4$ is consistent with the range of $A_V = 2$ to 4 seen in their Fig. 3. Second, comparing 4U 0142+61 with 1E 1048.1−5937, Durant & van Kerkwijk (2005a) noted that in order for the broad-band optical/infrared spectrum of these AXPs to have the same shape, the difference in reddening would have to be $\Delta A_V = 2.5 \pm 0.5$. This was inconsistent with previous estimates, which gave very similar values of A_V (based on the very similar values of $N_{\rm H}$; see Table 5.1), but is consistent with our new results, which give a difference in reddening of $\Delta A_V = 1.3 \pm 3$. Thus, the optical/infrared spectra of the different AXPs may be similar in shape, and therefore produced by the same mechanism.

5.9 The Spectral Energy Distribution of 4U 0142+61

With our empirical estimates of the intrinsic (soft) X-ray spectra, and the revised estimate for optical/infrared reddening, we can re-examine the spectral energy distributions of the AXPs. We only consider 4U 0142+61, since this object is the only one for which we find a significantly different column density from that typically quoted. Furthermore, it has the best X-ray data, and the best broad-band coverage, from mid-infrared (Wang et al. 2006), to near-infrared and optical (Hulleman et al. 2004; Israel et al. 2004), to hard X-rays (Den Hartog et al. 2006).

Figure 5.4 shows the inferred intrinsic spectral energy distribution of 4U 0142+61, determined with our new values of $N_{\rm H}$ and A_V. The interpretation of the optical and infrared emission is still unclear: it could be understood as combination of a large mid-infrared bump combined with a rising power-law that has a sharp break at B, or as a combination of a much smaller mid-infrared bump combined with a flatter power-law and a large emission feature centered between R and V. Wang et al. (2006) interpret the mid-infrared bump as arising from a passively illuminated dusty disc. This disc is presumably formed from supernova fall-back material, and the data is well fitted by a blackbody from dust at the sublimation radius. This disc would also influence the flux in the K-band. Wang et al. used our new estimate of $N_{\rm H}$, but their results are not very sensitive to the exact value of $N_{\rm H}$, as long as the reddening is above $A_V \approx 2.6$ (Chakrabarty, 2005, pers. comm.).

The soft X-ray spectrum in Figure 5.4 suggestively has a slope which would meet up with the optical points if extended. This is in marked contrast with the earlier power-law models, which grossly over-predict the optical emission (see §5.1). The uncertainty in the slope of the soft X-rays is dominated by the uncertainty in the Hydrogen column (and its systematics, particularly due to abundance uncertainties), so there is not enough information at present to say whether the break between the B- and V-bands is due to an emission or an absorption feature.

5.10 Conclusions

We have attempted to measure the extinction to the AXPs without making assumptions about what their intrinsic spectral shapes might be. With our resulting best estimates, we derived intrinsic spectra, which can be compared with each other as well as with predictions,

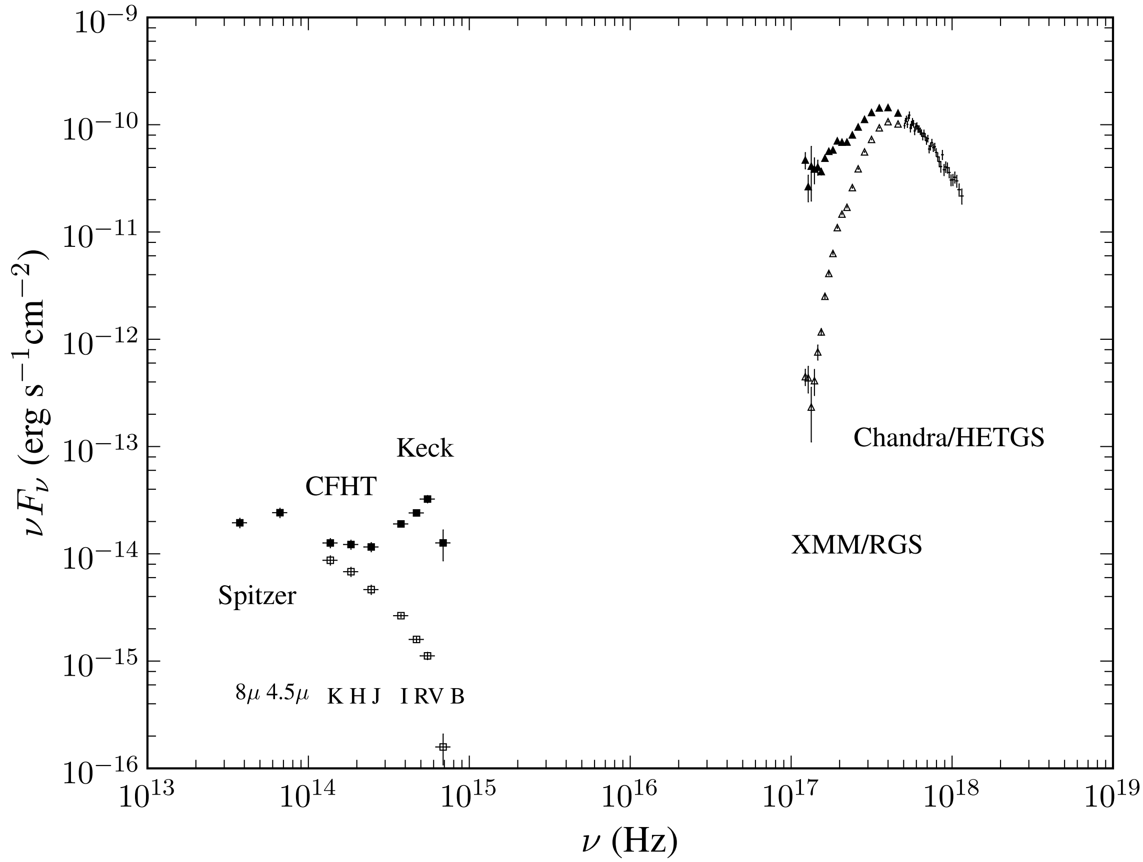

Figure 5.4 Spectral energy distribution for 4U 0142+61. Triangles are XMM/RGS data, as observed (open) and de-extincted (filled) as described in the text. Open squares are observed broad-band photometry (mid-IR from Wang et al., 2006; JKH from Israel et al. (2004); BVRI from Hulleman et al., 2004). Filled squares are the photometric points de-reddened with $A_V = 3.5$ (see text). Crosses in the higher-energy X-ray part of the spectrum come from *Chandra* (Juett et al., 2002); extinction is not important in this region of the spectrum. XMM data is binned in frequency ($\delta\nu$) corresponding to $\delta\lambda = 1\,\text{Å}$, and *Chandra* data to $\delta\lambda = 0.1\,\text{Å}$ for clarity.

such as those from simulations and semi-analytic models that are now being produced within the magnetar framework (e.g., Lyutikov & Gavriil 2006; R. Fernández & C. Thompson 2006, pers. comm.).

Apart from these comparisons, future work could include extending our analysis to other sources (once better spectra become available), or improving the precision of our measurements using further *XMM-Newton* observations (some already taken but not yet public) or *Chandra* spectra (some available). More interestingly, by measuring the run of reddening with distance along the line of sight to the AXPs (using field stars), our extinction estimates can be used to estimate distances and thus determine the intrinsic luminosities of the AXPs. It turns out that although the extinctions are not very well determined, the AXPs fall into areas of rapidly rising extinction associated with spiral arms, and so can be well localized (Durant & Van Kerkwijk, 2006c). Finally, our reddening estimates will place on much firmer footing inferences from further optical and infrared studies, such as could be used, e.g., to uncover the nature of the break seen between V and B in 4U 0142+61 (Hulleman et al. 2004) or to measure the precise parameters of the possible debris disk around that source (Wang et al. 2006).

Acknowledgments We thank Adrienne Juett, Norbert Schultz, and Hermann Marshall for discussion of the X-ray absorption edges, and Vik Dhillon for letting us use his *XMM-Newton* data on 1E 1048.1−5937 before it became public. We also gratefully acknowledge the comments of the anonymous referees, which helped us clarify the statistical significance of our analysis and the presentation of our results. This work is based on archival observations obtained with XMM-Newton, an ESA science mission, and made extensive use of NASA's ADS and Simbad. We acknowledge financial support from NSERC.

Chapter 6

Distances to Anomalous X-ray Pulsars using Red Clump Stars[1]

6.1 Abstract

We identify "red clump stars" – core helium-burning giants – among 2MASS stars and use them to measure the run of reddening with distance in the direction of each of the Galactic Anomalous X-ray Pulsars (AXP). We combine this with extinction estimates from X-ray spectroscopy to infer distances and find that the locations of all AXP are consistent with being in Galactic spiral arms. We also find that the 2–10 keV luminosities implied by our distances are remarkably similar for all AXPs, being all around $\sim 1.3 \times 10^{35}\,\mathrm{erg\,s^{-1}}$. Furthermore, using our distances to estimate effective black-body emitting radii, we find that the radii are tightly anti-correlated with pulsed fraction, and somewhat less tightly anti-correlated with black-body temperature. We find no obvious relationship of any property with the dipole magnetic field strength inferred from the spin-down rate.

6.2 Introduction

The Anomalous X-ray Pulsars (AXPs) are young, energetic, X-ray bright isolated neutron stars, with spin periods of the order 10 s. They are called *anomalous* since their luminosity far exceeds the energy available from spin-down, and no binary companions are seen. AXPs (along with the related Soft Gamma-ray Repeaters or SGRs) are now believed to be *magnetars* (Thompson & Duncan, 1996). Magnetars have huge external magnetic fields ($\sim 10^{14}$G) and even larger internal fields. It is the decay of the magnetic flux which provides the luminosity seen, and is responsible for a whole array of observational effects such as bursting and giant flares. See Woods & Thompson (2004) for a summary of recent observational data on magnetars, and how they are modeled.

Since they are young remnants of massive, short-lived progenitors, all of the AXPs are found in the Galactic plane (except for CXOU J010043.1−721134 which is in the Small Magallanic Cloud). This causes a major obstacle to observations: high interstellar extinction, manifested as photo-electric edges from different elements in the soft X-ray band, and as continuum extinction from dust in the optical and near-infrared. Since the amount of extinction

[1]Accepted for publication in ApJ (Durant & van Kerkwijk, 2006b).

has been difficult to estimate accurately, the spectral energy distributions of AXP have been subject to large uncertainties (Hulleman et al. 2004; Durant & van Kerkwijk 2005a, 2006a).

Furthermore, even if the interstellar absorption is well-characterized, distances and therefore absolute fluxes are difficult to determine. The simplest distance estimate is made by requiring that the black-body component typically inferred from the X-ray spectrum arises from a neutron-star sized area. We do not, however, expect the surfaces of AXPs to be homogeneous, both on observational grounds (they pulsate) and from theoretical considerations (the magnetic field, which affects the heat conduction, will vary across the surface).

For AXPs that are associated with supernova remnants or other interstellar structure, a more direct distance estimate can be made using 21 cm HI measurements and the Galactic rotation curve. Convincing cases for associations with supernova remnants have been made for two AXPs: 1E 2259+589 with CTB 109 (Gregory & Fahlman, 1980), and 1E 1841−045 with Kes 73 (Sanbonmatsu & Helfand 1992). Furthermore, Gaensler et al. (2005) found an HI bubble coincident with the direction of AXP 1E 1048.1−5937, which they suggest was created by the winds of the massive progenitor of the AXP (see Muno et al. 2006 for a discussion of possible massive progenitors to AXPs). Even for these systems, however, distance estimates can be rather uncertain, with different authors finding inconsistent results (we discuss this further in §6.4 and 6.5).

For sources in the Galactic plane, a different clue to the distance is available if one has a good measure of the interstellar extinction, and the run of extinction with distance can be determined independently. This works because the extinction increases with distance, more so towards star-forming regions and molecular clouds.

The so-called red clump method provides a means for deriving the function of reddening versus distance in any given line of sight, based on field stars over a relatively small area. On a coolor-magnitude diagram, core helium-burning giants form a distinctive population: either the horizontal branch (for low metalicitity) or the red clump (for moderate or high metalicity). Stars spend up to 10% of their lifetime in this phase, and are much more luminous than typical main sequence stars. Because their helium cores all have roughly the same mass, their luminosities are largely independent of the total stellar mass (Stanek & Garnavich, 1998). They thus make very useful standard candles, and since the excellent calibration by *Tycho*, have been used for distance measurement (see Stanek et al. 1997; Paczyński & Stanek, 1998). López-Corredoira et al. (2002) noted that in an infrared color-magnitude diagram of a stellar cluster ($J-K$ versus K for example), the distribution of red-clump stars is even tighter, since their infrared colours are insensitive to metallicity. As a result, they are good infrared standard candles and if the red clump can be identified at each of a range of distances, then the reddening at each distance can be calculated. The method has been used not only by López-Corredoira et al. (2002) to measure the density distribution of stars in the Galaxy, but also by, e.g., Drimmel et al. (2003) to map the distribution of dust.

Here, we apply the red-clump method to measure distances to the Anomalous X-ray Pulsars. In section §6.2, we first describe how we applied the red-clump method, focussing on the AXP for which the method was most tricky, and in section §6.3 we use this field to test the reliability of the method, and to estimate uncertainties in the derived values. In §6.4, we present the results of the red clump method applied to each of the Galactic AXPs, and we discuss the implications in terms of distance. In §6.5, we compare our new distances with those in the literature, in particular for the controversial case of 1E 2259+589 and the associated supernova remnant CTB 109. In §6.6, we use our results to infer luminosities and emitting radii, and discuss how these depend on other AXP properties. We draw conclusions in §6.7.

6.3 Method

Our method closely follows that described by López-Corredoira et al. (2002), which in turn is similar to the earlier method presented in Stanek et al. (1997). We start with data from the 2MASS Catalog (Skrutskie et al., 2006) in the J- and K_S-bands. (From here on, we refer to the K_S band as K for brevity.) Since all the Galactic AXPs lie along the plane, we find a large number of 2MASS stars at relatively small radii around each source. For the analysis, we initially chose the 9999 nearest stars and used these to construct $J-K$ versus K color-magnitude diagrams (covering circular fields around each AXP with radii in the range 9.′6 to 20.6.′). Below, we first discuss in some detail the results for the AXP 1E 1048.1−5937, for which applying the method proved to be most tricky.

Figure 6.1 shows the colour-magnitude diagram for 1E 1048.1−5937. On this graph, reddening alone causes stars to move to the right and slightly down (redder and fainter) and increased distance alone causes stars to move down (fainter in all bands). From the Figure, one sees that the main sequence (on the left of the diagram) contains the bulk of the stars. Due to the large range in intrinsic luminosities, stars from different distances and reddenings show up as an amorphous conglomeration, with an increasing range in color towards the faint end. The red clump, however, shows up as a clearly defined stripe (center), representing stars of the same luminosity and color at different distances and reddenings. Since red-clump stars are relatively rare, few are found at magnitudes brighter than about $K = 9$ (distance $\lesssim$1.3 kpc). Stars redward of the red clump are either poorly measured (e.g., blended in the K band), background super-giants or young stars with infrared excess.

One can select any range in K in the diagram in order to find the peak of the red-clump star distribution for that range. Our method works by identifying this peak for various ranges in K-band magnitude. As an example, we have selected a 0.6 mag-wide strip around $K = 12.9$ for analysis. The histogram of $J-K$ colors for the selected stars is shown in Fig. 6.2. To find the peak of the red-clump distribution, we fit a Gaussian function to the histogram values. The main complication is contamination by background, highly reddened main sequence stars (see again Fig. 6.1). These tend to skew the distribution, and for K approaching 14 overwhelm the Gaussian feature. To account for these contaminants, we fit the histogram with a power law plus Gaussian:

$$y = A_{\rm cont}(J-K)^{\alpha} + A_{\rm RC}\exp\left(-\frac{1}{2}\left[\frac{((J-K)-(J-K)_{\rm peak})^2}{\sigma^2}\right]\right) \tag{6.1}$$

where $(J-K)$ is the stellar color, $(J-K)_{\rm peak}$ is the peak of the distribution, σ the width of the peak, $A_{\rm RC}$ and $A_{\rm cont}$ the normalizations of the red-clump and contaminant terms, and α the power-law index.

Equation 6.1 is fitted using a standard least-squares algorithm, assuming the errors in each histogram bin are the same. This process is repeated for successive bins in K until the 2MASS completeness limit is reached. Figure 6.1 shows the fitted red clump positions overdrawn on the color-magnitude diagram. Features from this plot, such as the poor fits around $K = 11$, will be discussed in the next section.

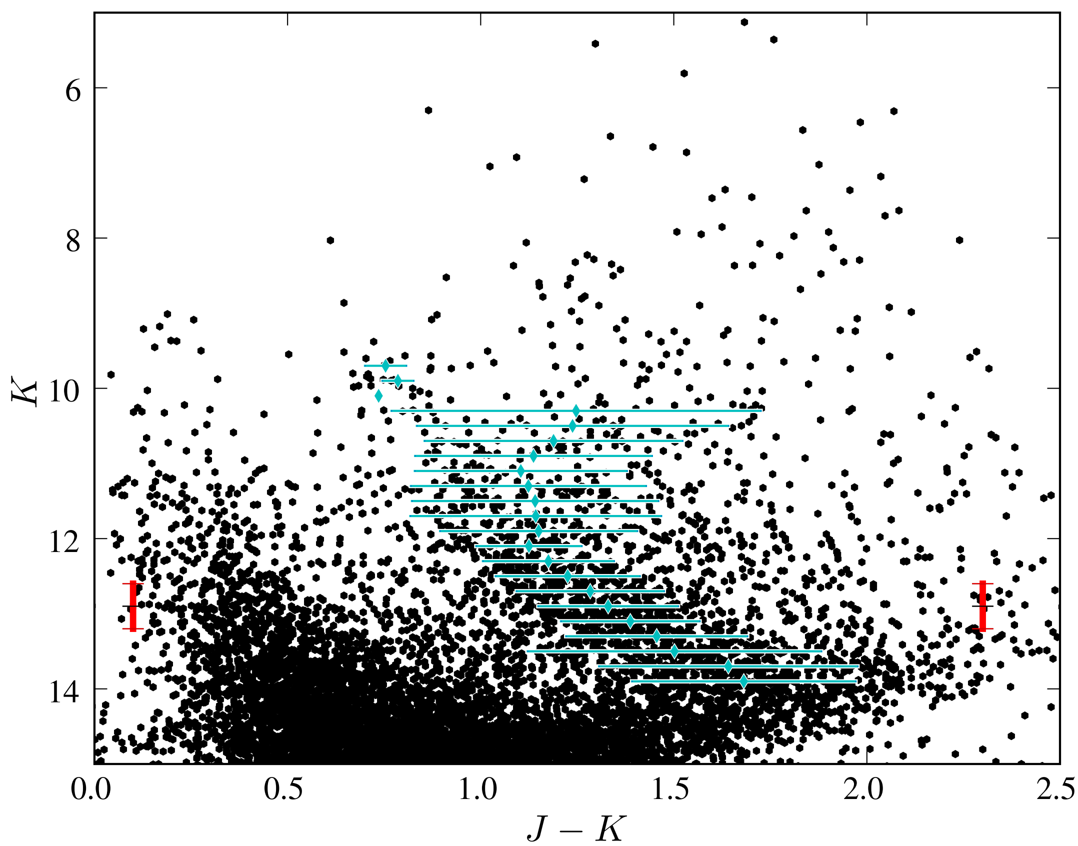

Figure 6.1 Color-magnitude diagram for 9999 stars within 11′.4 of 1E 1048.1−5937. Main-sequence stars are found from about $(J-K, K) = (0.2, 10)$ to (0.5,14), and red-clump stars show up as an over-density from about (1.0,10) to (1.7,14). The fitted location of the red-clump peak (diamonds) and its extent (bars, showing $\pm 1\sigma$ or roughly the full width at half maximum) are marked. The error bars (left and right edges) show the location and size of the strip used to create the histogram shown in Fig. 6.2. The poor fits near $K = 11$ are discussed in §6.3.

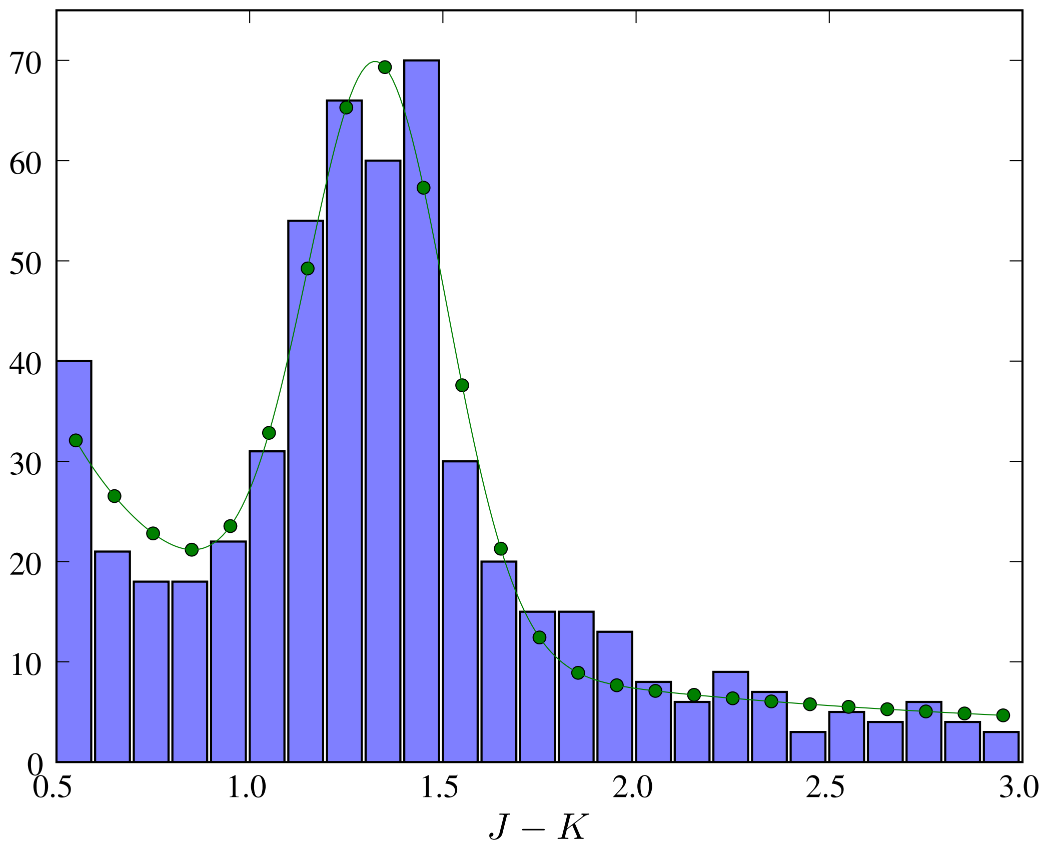

Figure 6.2 Histogram of the $J-K$ values of stars extracted from Fig. 6.1 in a 0.6 mag interval around $K = 12.9$. Overdrawn is a fit to this histogram using Eq. 6.1, with the curve showing the analytical function and the points the best-fit values.

Since our algorithm finds only local minima in the χ^2 surface, it is necessary to supply reasonable starting values to the routine. We found that if we chose our strips in K to overlap, and used the best-fit values of the previous histogram, smooth changes in the peak were well followed. To increase robustness, our algorithm also checks the relative residuals of fits performed with a few different initial values of $(J-K)_{\rm peak}$; this covers the case where there is a sudden jump in reddening. Note that the choice of the range in K of each histogram and the extent to which these strips overlap is arbitrary, but should not change the results. We test this below.

Assuming the intrinsic color $(J-K)_0 = 0.75$ and the intrinsic luminosity $M_K = -1.65$ (Wainscoat & Cowie 1992), the translation of $J-K$ versus K into reddening versus distance corresponds to decomposing the reddening and distance vectors on the diagram for each red-clump peak found. The infrared color excess can be expressed as a visual reddening through (e.g., Schlegel et al. 1998):

$$A_V = \frac{(J-K)_{\rm peak} - (J-K)_0}{0.164} \tag{6.2}$$

The distance is then (correcting for reddening in K):

$$d = 10^{0.2(K-M_K-0.112A_V)} \times 10\,{\rm pc}. \tag{6.3}$$

6.4 Robustness and Uncertainties

The approach discussed above for converting a 2MASS dataset into a run of reddening with distance does not yet yield estimates of the uncertainties. Here, we investigate the error analysis for the field of 1E 1048.1−4937 in detail. We chose this field since it exemplifies the problems faced, and lies near one of the most complicated regions of the Galaxy, the Carina Complex. None of the other five AXP fields are more complex.

For our discussion, we estimate the formal uncertainties on the location of the red-clump peak with $\sigma/\sqrt{N_{\rm RC}}$ (where the number of red-clump stars $N_{\rm RC} = \sqrt{\pi}\sigma A_{\rm RC}$, with σ and $A_{\rm RC}$ from Eq. 6.1), which should be a good approximation if the Gaussian is a reasonable fit for the distribution of infrared colors in the red clump, and if the contamination by other stars is not too large. For the test field, the FWHM of the peak is typically ≈ 0.3 mag and the number of stars of order 100s, giving uncertainties of the position of the peak ~ 0.02 mag (one-sigma).

In principle, one could derive better formal uncertainties, e.g., by calculating the χ^2 values around the best-fit function, or – more appropriately for a counting problem with Poissonian statistics – using a maximum-likelihood method (which might even take into account the probability distributions in J and K for each star). We believe, however, that a better approach is to keep the estimate of the formal errors simple and combine it with empirical tests for systematic effects using different subsets of stars and using multiple fields.

The first test we did was to try different cuts on the 2MASS data using the magnitude error estimates and photometric quality flags, in order to keep only the best measured points. We found, however, that this had the sole effect of truncating the CMD at brighter magnitudes, without significantly tightening the spread in the red-clump stars at any magnitude. This suggests that any spread in the red-clump stripe on a CMD beyond the typical measurement error is due predominantly to field inhomogeneities. Thus, in order to find the reddening to as large a distance as possible, we continue to use all the available 2MASS stars in a given field.

An important feature that can be seen for the bins between $K = 10.5$ and 11.5 in Fig. 6.1 is that there seems to be overdensities at both $J - K = 0.9$ and $J - K = 1.2$ and that the fitted points lie in between these two. This suggests that the reddening at these distances is variable across the field. Since two peaks are visible, part of the field might be obscured by denser interstellar matter.

To investigate the inhomogeneity in reddening, and to determine how this affects the sensitivity of method, we analyzed six fields at a distance of $15'$ from 1E 1048.1−5937 (note that these fields overlap somewhat with the target field). Figure 6.3 shows the resulting graphs of $J - K$ versus K (we show this graph rather than A_V versus d, since d depends on both values). One sees that the distribution of reddenings is bimodal, with fields 1, 5 and 6 showing consistently less reddening as a function of distance than fields 2, 3 and 4, but merging to the same value for faint K (note that field 5 appears to show a decrease in reddening; this is due to the same bimodality that affects the central pointing). Thus, there is structure in the Galactic dust distribution: a dust cloud appears to cover the field gradually from the North-West with increasing distance. Considering the complex structure of the local Carina Nebula, this is not surprising; it is simply a consequence of the large reddening gradients in the area.

From Fig. 6.3, comparing fields with similar runs of $J - K$ as a function of K (such as 1 and 6, and 3 and 4), one sees that the uncertainties inferred from the Gaussian fit (which are similar for all fields) agree roughly with the scatter between those fields, suggesting that they are reasonable estimates of the uncertainties. (One also sees that compared to the scatter along the curve, the error bars appear to be overestimates – this, however, is a consequence of the fact that the points are not independent, as the strips in K overlap.)

Given the inhomogeneity in reddening, we checked whether chosing a smaller field would yield a tighter fit. Figure 6.4 shows a comparison of the results for the original set of 9999 stars around 1E 1048.1−5937 with the results for just the central one-third of those stars, as well as, for comparison, for a randomly chosen one-third of the stars. Interesting behavior is seen in the randomly-chosen curve: generally it follows the curve of the original sample (with increased error bars), but around $K = 12$ the inferred $(J - K)$ color decreases a little and is lower than inferred from the original sample. This is due to the competition between the two areas with different reddening in the field. With fewer stars, the fit is more liable to jump from one over-density to the other. For the central sub-sample, however, this does not occur. Instead, it shows consistently lower reddening than the original sample at all values of K. The errors are only slightly larger, since the smaller number of stars is offset by the smaller spread in the colors of the red-clump stars.

From our tests, we conclude that in the field of 1E 1048.1−5937 a dark cloud towards the North obscures some fraction of area within the $11\overset{'}{.}4$ radius covered by the original 9999 stars, but it does not cover the source and hence should be ignored in determining the run of reddening with distance.

More generally, we conclude that, since our aim is not to determine accurately the *average* reddening in the field, but rather to find the reddening at the center of the field only, we should use the minimum number of stars required for our method to work reliably. Empirically, we find that this is $\sim$3000 stars; with fewer stars, the red-clump peak becomes poorly defined due to small-number statistics.

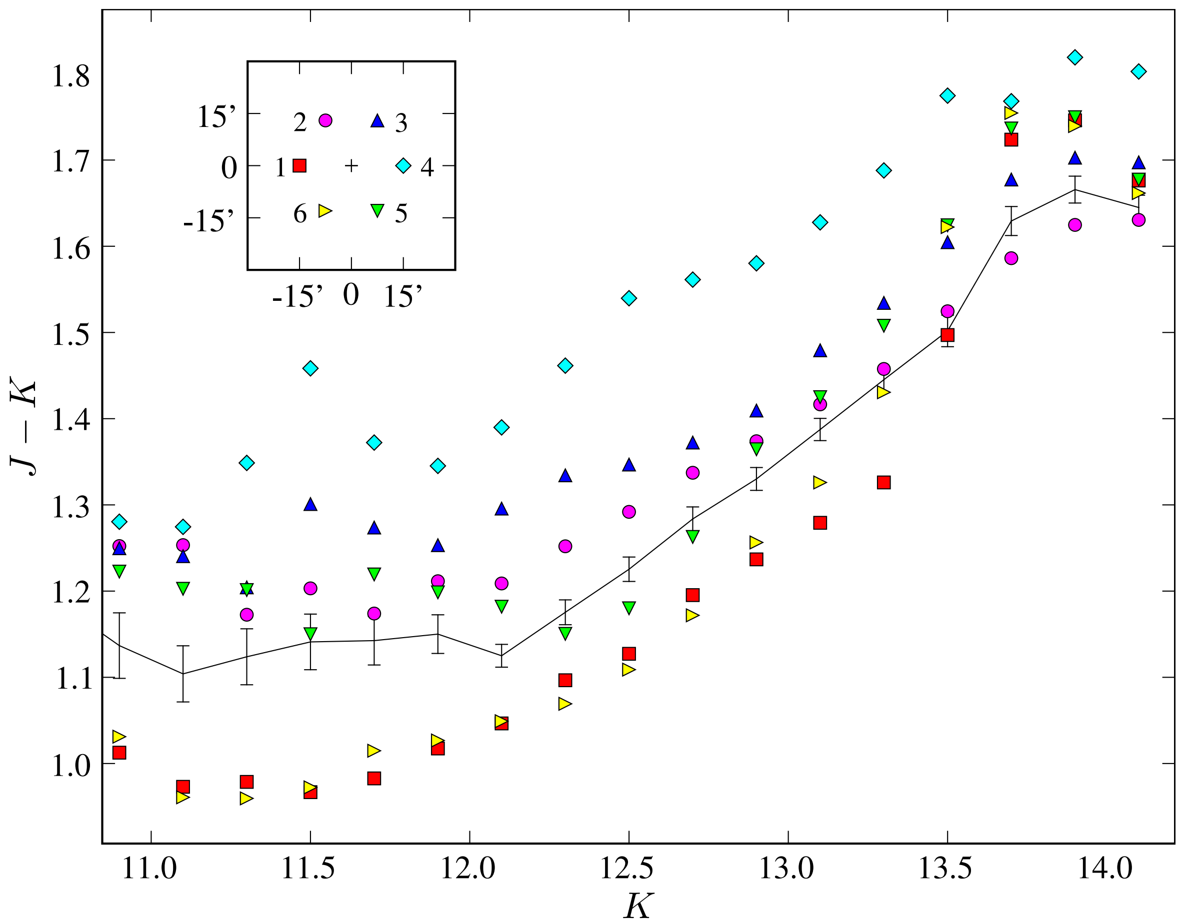

Figure 6.3 Color of the red-clump stars as a function of magnitude for the field around 1E 1048.1−5937 (curve with error bars) and six fields surrounding it (symbols). Field 1 is offset by 15′ to the East, and the other fields are placed anti-clockwise with increasing number (see inset).

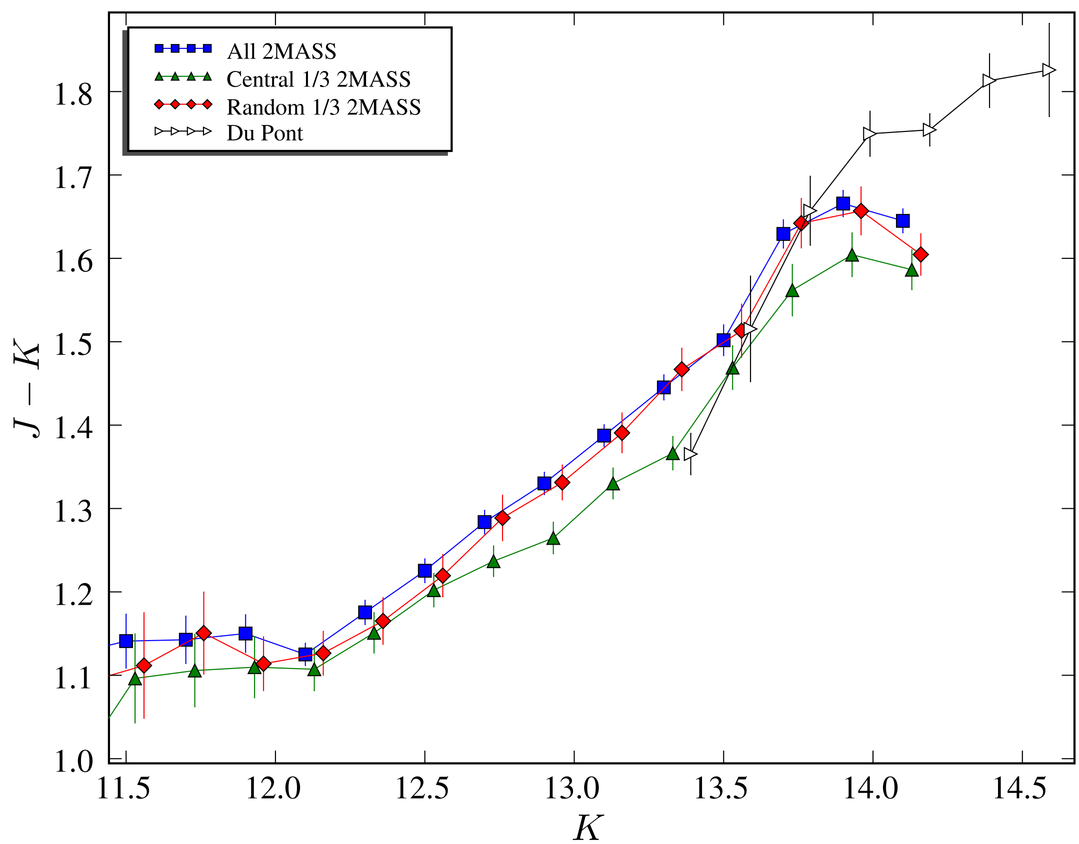

Figure 6.4 Color of the red-clump stars versus magnitude in the direction of 1E 1048.1−5937 for different subsamples (see inset). The curves have been slightly offset in K for clarity.

In the case that there remains substantial inhomogeneity within the small field under examination (this is certainly possible, but it turns out not the case for the AXP fields), we must raise an important caveat to the use of the method. Because the over-desity finding rutine picks the best Gaussian feature out of the color histograms, it will be biased towards the more homogenous part of the field. If the field is highly inhomogenous, it may not be able to locate the red-clump satisfactoraly; if a compact dense cloud obscures part of the field, then the method will give the reddening of the unobscured part of the field, since the cloud will have strong column density gradients across it.

The next effect we checked is that of the choice of the size and overlap of the bins in K. In order to have as high a distance resolution as possible, one would like to use bins in K that are as small as possible. In order for the red-clump peak to be better defined on each histogram, however, one would prefer more stars and a narrower distribution of red-clump star colors. As discussed above, increasing the field size in order to use more stars does not help since the reddening may be non-uniform. The same is true for increasing the K-bin sizes: different colors from different distances will tend to blur the red-clump peak. Since in

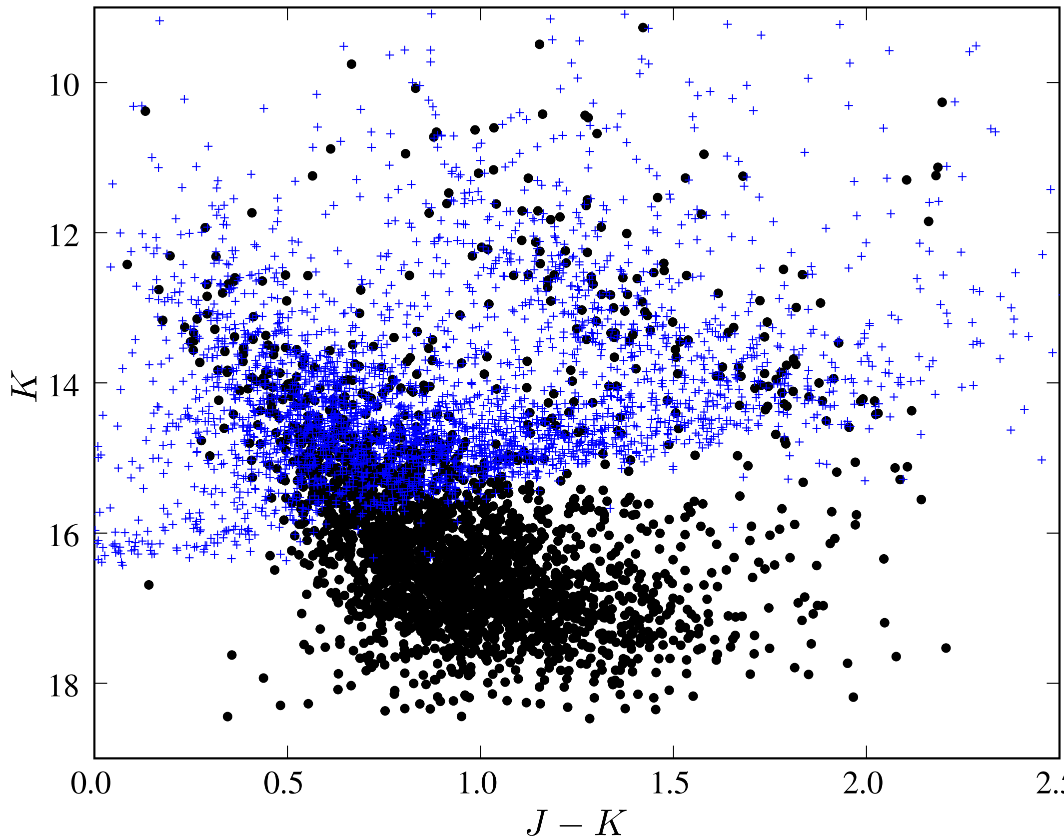

Figure 6.5 Deeper color-magnitude diagram of the field of 1E 1048.1−5937, from Du Pont imaging. The Du Pont sources are shown as black circles, and the 2MASS points (from the closest 3300 stars) as crosses.

this case this also comes at the cost of reduced distance resolution, we opt for bin sizes as small as possible which still give reliable results: 0.6 mag, with steps of 0.2 mag. The overlap factor does not change the results or our method, but it is convenient computationally and also allows us to determine slightly more accurately the locations of jumps in reddening.

The final thing we checked is the effect of the 2MASS limiting magnitudes on our measurements. Our precise estimate of the distance of 1E 1048.1−5937 from 2MASS data alone is uncertain, because the last point in our graph of $J-K$ versus K is likely affected by the incompleteness to fainter and to redder sources. To check for this, we obtained further, deeper JK infrared imaging data from the Wide-field Infrared Camera on the Du Pont 2.5 m telescope, Las Campanas (see Persson et al. 2002). We subtracted a sky frame from each image using the median of the science frames (this is required because of an additive component to the noise from fringing), registered and stacked the images. We tied the photometry directly to 2MASS using many stars cross-identified on each of the chips.

Figure 6.5 shows the new, deeper color-magnitude diagram for stars in the field of

1E 1048.1−5937. This includes stars from the chip containing the AXP and two adjacent chips (each chip has a size 200″ square). One sees that down to $K = 13$, $J - K = 1.4$, which corresponds to the last reliable red-clump location from the 2MASS data, the Du Pont and 2MASS data are consistent, having overdensities at the same colour. However, for the next group, at $K = 14$, $J - K = 1.8$, the Du Pont data indicate a location redder than the 2MASS data would have suggested. Thus we conclude that the reddening rises more quickly in this region, and the AXP is closer than otherwise would have seemed. We show the $J-K$ values obtained from the Du Pont data in Figure 6.4 and use these for the final point on the reddening curve for 1E 1048.1−5937 in Figure 6.7.

As mentioned above, the challenges faced in the field of 1E 1048.1−5937 are more severe than those for any of the other fields; none show reddening gradients as large, and for all the other sources (except 1E 2259+586, see §6.5) the appropriate value of the color excess lies either well before or beyond the completeness limit. Using what we have learned here, we perform our analysis on the central 3300 stars near each AXP, and infer uncertainties using the simple estimate from counting statistics.

6.5 Results

We determined the color of the red clump as a function of brightness using the nearest 3300 stars for each of the six Galactic AXP. In Table 6.1, we list the size of the field covered by these stars, and in Fig. 6.6 we show the corresponding color-magnitude diagrams, with the fitted locations of the red-clump stars indicated.

In converting our results to reddening as a function of distance, we prefer to use non-overlapping points. In choosing the points to use, however, one has a certain freedom to pick those that have with the smallest errors, and that show features most clearly. We attempt to do this, and check against the original color-magnitude diagrams that the breaks occur at the correct values of K. In interpreting the fitted points, we also use the fact that reddening can only increase with distance (e.g., we reject a poorly measured point with high reddening in favor of a later, better measured point with lower reddening).

Figure 6.7 shows the resulting runs of reddening with distance, with associated uncertainties. With X-ray extinction estimates for the AXPs, distances can simply be read off the graphs by first converting to A_V using $A_V = N_H \times 5.6 \times 10^{-22}\,\mathrm{cm}^2$ (Predehl & Schmitt, 1995). For three of the AXPs – 4U 0142+61, 1E 2259+589 and 1RXS J170849.0−400910 – new, model-independent estimates of the extinction were found by Durant & van Kerkwijk (2006a) using photo-electric absorption edges in high-resolution X-ray spectra. These are listed in Table 6.1; the uncertainties reflect the accuracy with which the depths of the various features could be measured. For one further AXP, 1E 1048.1−5937, our measurement was not very constraining, while for the remaining two, 1E 1841−045 and XTE J1810−197, no suitable high-resolution X-ray spectra were available. Hence, for these three AXPs, we use the extinction estimates compiled in Woods & Thompson (2004). These estimates are based on broad-band fits to the X-ray spectra, which means that their accuracy depends on the adequacy of the model (typically a two-component model composed of a power law and a black body). From a comparison of similar estimates with our direct measurements for the three AXPs, we expect that, at the relatively high extinctions found for these two sources, the estimates should be accurate to about 10%.

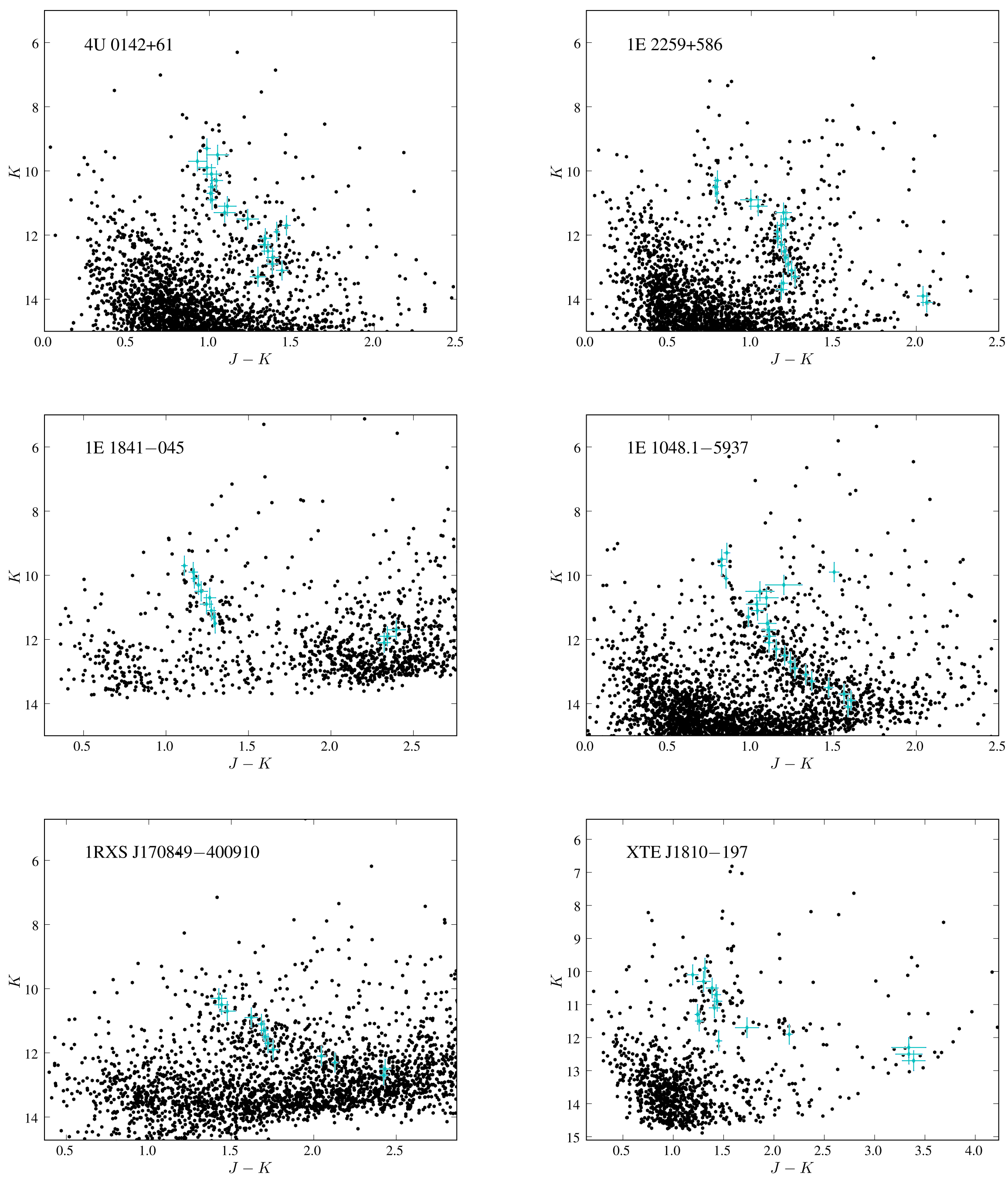

Figure 6.6 The color-magnitude diagrams used to infer the location of the red clump as a function of brightness, derived from the nearest 3300 2MASS stars around each object (within 5 to 12′). Overdrawn are the fitted red-clump peak colors together with the 1-σ uncertainties.

Before continuing, we should address a possible worry: that a large uncertainty is introduced in the various conversions used. First, above we implicity converted photo-electric absorption edges by metals to an equivalent hydrogen column N_H, and that in turn to visual extinction A_V. This is not as uncertain as it appears, however, since the relation of Predehl & Schmitt (1995) between X-ray and visual extinction, while quoted in terms of hydrogen column N_H, was based on X-ray measurements that were sensitive to metals along the line of sight, not hydrogen, just like ours. Hence, there is no uncertainty associated with, e.g., the metallicity or the hydrogen to dust ratio. A second worry one might have is about selective extinction, i.e., variations in the interstellar extinction law (usually parametrised by $R_V \equiv A_V/E_{B-V}$). There is, however, far less variation in the infrared (e.g., Mathis 1990). Since the optical extinction estimates of Predehl & Schmitt were largely based on a standard extinction law, we should thus circumvent any problems at visual wavelengths by using the same standard relation between infrared and visual extinction. (Indeed, it might well be that one would find a tighter relation than that of Predehl & Schmitt (2005) if one redid the analysis in terms of infrared extinction.)

From Fig. 6.7, one sees that for most sources, the measured reddening places the source at a jump in the run of reddening with distance. As a result, the uncertainty in the distance estimate is dominated not by uncertainty in A_V, but by the accuracy with which the jump can be located, which in turn is determined by the size of the bins in K. A bin size of 0.6 mag corresponds to a 15% uncertainty in distance. (As discussed above, the size of the bins was chosen to give the best distance resolution yet yield reliable measures of reddening without using a large field and thus increasing the risk of bias by spatial variations in reddening.) The only source not located at a jump in reddening is 1E 1048.1−5937. Hence for this source, uncertainty in the distance is dominated by the (relatively large) uncertainty in the reddening estimate.

Table 6.1 gives final inferred distances and limits. Below, we describe the results for each object in more detail, trying to match rapid increases in reddening with known spiral arms, and locating the AXPs in the Galaxy (see Fig. 6.8). This can be viewed as an update of the similar map shown in Gotthelf & Vasisht (1998; their Figure 4). We focus on the outcome of our analysis, deferring a more detailed comparison of the implied distances with previous determinations to §6.6, and a discussion of the implications in terms of luminosities and other derived quantities to §6.6.

4U 0142+61. In this field, two regions of reddening are seen, $A_V \simeq 2$ in the near field and $A_V \simeq 4$ out to large distances. The latter confirms the statement by Hulleman et al. (2004) that the reddening could not exceed $A_V \simeq 5$ in this direction, based on the colors of a background galaxy and of field stars. From the estimated reddening to the source of $A_V = 3.6 \pm 0.2$, we conclude that the AXP is located in a region of rapidly rising reddening at $d \simeq 3.5$ kpc. Likely, this region is associated with the Perseus arm.

Looking in more detail at Fig. 6.6, one sees that for $K > 13.5$, one can no longer identify the over-density of red-clump stars. The stripe seen at lower K does not continue and no over-density is seen redward of this stripe either, as could be caused by a sudden increase in reddening. Most likely, this indicates simply that there are not many red-clump stars beyond a distance of ∼8 kpc. Consistent with this, one sees that the red side of the main sequence has a smooth distribution as K increases from 13 to 15; if the absence of red-clump stars beyond $K > 13.5$ were due to a large, sharp increase in reddening, this should be visible for

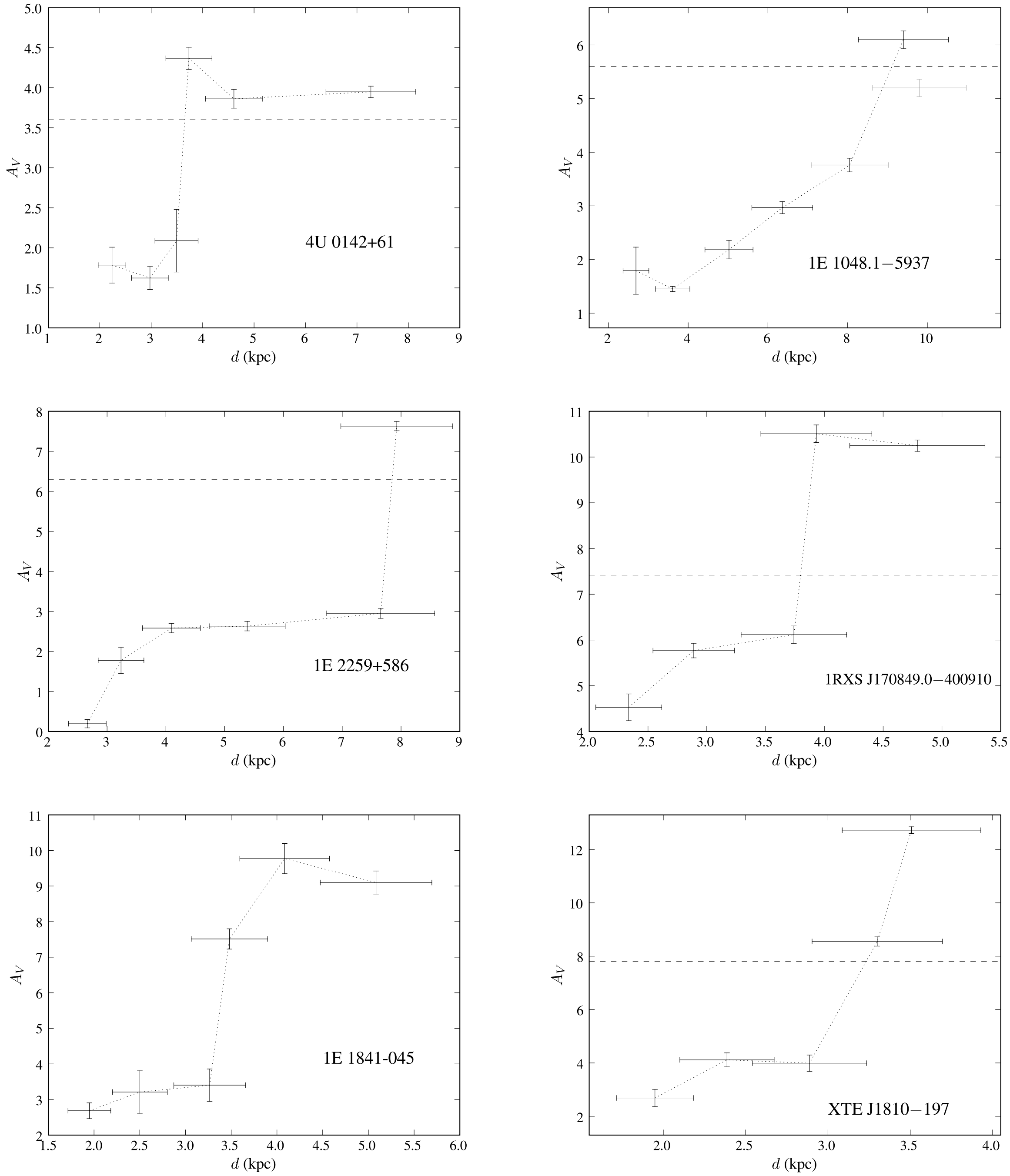

Figure 6.7 Run of reddening with distance along the line of sight to the six Galactic AXPs. The best estimate for the reddening for each object is shown by a dashed horizontal line (for uncertainties, see Table 6.1 and the text); note that the estimated $A_V = 14$ for 1E 1841−045 falls outside the graph. The grey point in the graph for 1E 1048.1−5937 is discussed in the text.

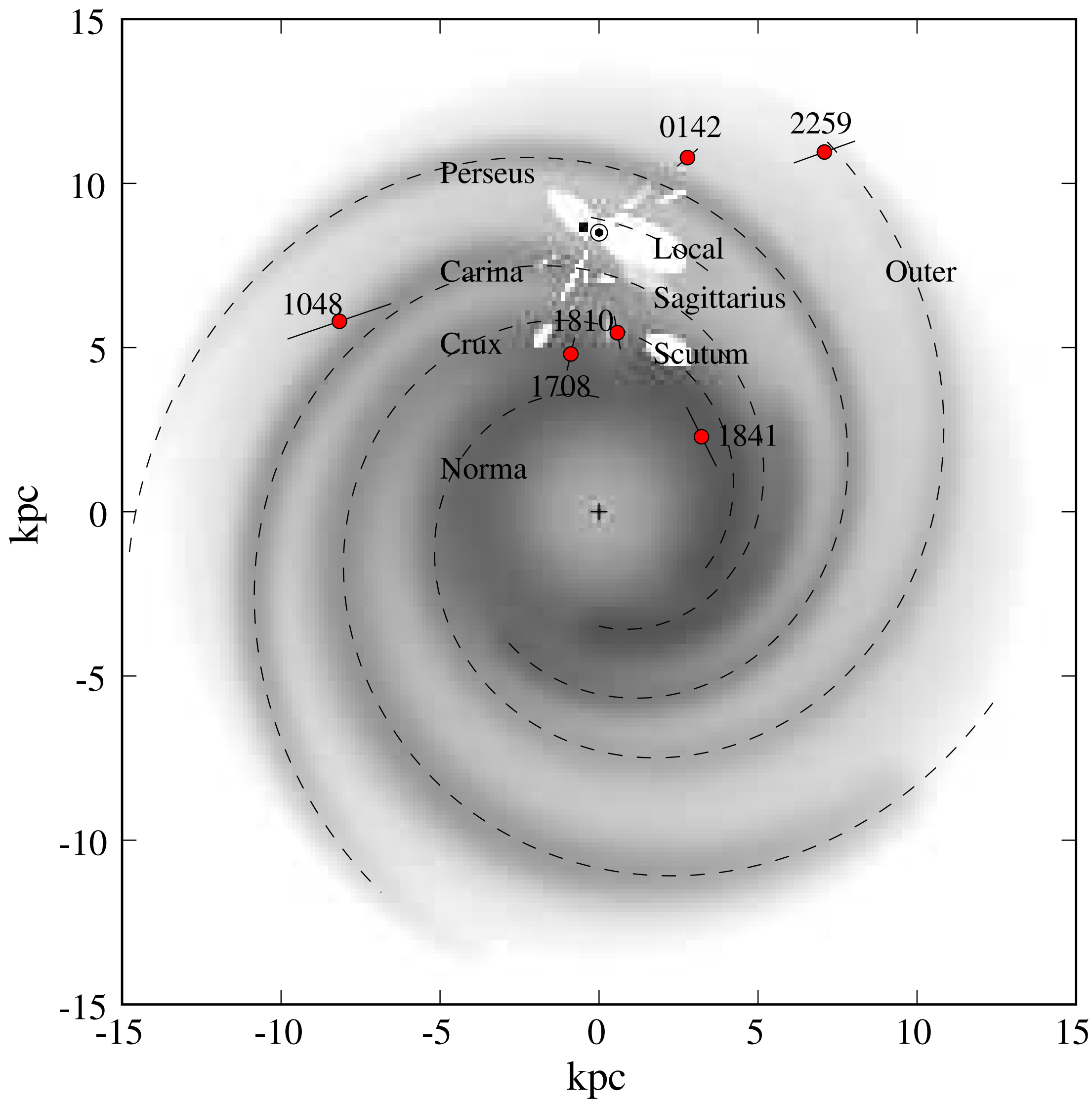

Figure 6.8 Schematic map showing the positions of the AXPs in the Galactic Plane relative to the Galaxy's spiral arms. The AXPs are indicated with circles and labeled with abbreviated names, the Galactic center is marked with a "+" sign, and the location of the sun with a $\odot$ symbol (at a galactocentric distance of 8.5 kpc). Spiral arms are shown using a fit with a simple four-arm logarithmic spiral model (dashed lines, see Cordes & Lazio, 2002) and free electron density (grey scale, taken from Cordes & Lazio, 2002). The white patches are local interstellar cavities and the dark spot near the sun is the Gum Nebula. The grey scale backdrop has been rescaled to fit these axes.

the main-sequence stars too.

1E 1048.1−5937. Reddening rises continuously in this field, almost linearly with distance out to $\sim$12 kpc. This is probably due to the Carina Arm, which lies along the line of sight in this direction (Dame at al. 2001; Fig. 6.8). Our estimate of the reddening to the AXP places it at the tail end of this function. The 2MASS completeness limit in the J-band causes the stars to go undetected beyond a line $((J-K), K) = (1.5, 15)$ to (2.5,12). Our distance estimate is therefore based on the Du Pont photometry we obtained, which goes deeper than the 2MASS survey (see §6.4 and Figure 6.5). This affects only the last point in the graph of $A_V(d)$. We include in Figure 6.7 the furthest point which would have been obtained from the 2MASS data alone in faint grey.

Despite the existance of a new estimate of reddening from Durant & van Kerkwijk (2006a), the value given was not very constraining. We therefore have used the old estimate base on fitting the sum of a black-body and power-law to the X-ray spectrum. In this particular case, that approach should be the least error prone, since the power-law component is the shallowest of the AXPs, and hence has relatively little influence on the low-energy region of the spectrum, to which N_H is most sensative (Woods & Thompson, 2004).

Our estimated distance is around 8.6 kpc. This distance estimate is inconsistent with that of Gaensler at al. (2005); we return to this in §6.6.

1E 2259+589. In this field, the reddening is low up to $d \simeq 3$ kpc, next rises to $A_V \simeq 3$, and then stays at that value out to about 6.5 kpc, where it shows a second and larger jump. From Fig. 6.6, one sees that this second region of reddening is inferred from only a few stars at around $J-K = 2.0$ and $K = 14$. We believe it is genuine, however, for several reasons. First, at $K = 14$ there is a notable absence of stars at $J-K = 1.2$, below the location of the stripe for brighter magnitudes. Second, in contrast to what we saw for 4U 0142+61 above, the main sequence's red edge does appear to show a jump, from about $J-K = 0.7$ at $K = 13.5$ to $J-K = 1.2$ at $K = 14$. Third, the two jumps have a nice correspondance with expected jumps due to spiral arms, with the nearer one being due to the Perseus arm and the farther one due to the Outer arm (Fig. 6.8).

Assuming the second jump in reddening is real, the AXP's estimated reddening of $A_V = 6.3 \pm 0.7$ places it into this region, and thus likely in the Outer arm, at $d \simeq 7.5$ kpc. Were the last point in the curve of $A_V(d)$ affected by incompleteness of the 2MASS sample, as was the case for 1E 1048.1−5937 (above), this would move the point even further redward, make the jump steeper, and not significantly affect the estimated distance. In §6.6, we compare this with other distance estimates, in particular of CTB 109, the well-studied supernova remnant associated with 1E 2259+589.

1RXS J170849.0−400910. For this field, strong jumps in the reddening curve are seen, which likely are associated with the Carina and Crux spiral arms. The estimated reddening for the AXP places it into the second of the jumps, at about 3.5 kpc. From this field, one also sees that the red-clump method fails to work to large distances in the presence of very large reddening: stars can no longer be detected in the J-band. The detection threshold of the 2MASS survey can be seen in Fig. 6.6 as a marked absence of stars in the lower right-hand side.

Table 6.1. Distances to the Galactic Anomalous X-ray Pulsars

Object	Field Radius (arcmin)	N_H $10^{21}\,\mathrm{cm}^{-2}$	A_V (mag)	Distance[a] (kpc)
4U 0142+61	12.1	6.4±0.7	3.5 ± 0.4	3.6 ± 0.4
1E 1048.1−5937	6.3	10.0	5.6	9.0 ± 1.7
1E 2259+589	10.6	11.2±3.3	6.3 ± 1.8	7.5 ± 1.0
1RXS J170849.0−400910	5.3	13.8±4	7.7 ± 2.2	3.8 ± 0.5
1E 1841−045	5.3	25	14	≥ 5
XTE J1810−197	6.0	14	7.8	3.1 ± 0.5

Note. — The three extinction estimates with uncertainties are from measurements of edges in high-resolution X-ray spectra by Durant & Van Kerkwijk (2006a). The other estimates, taken from the compilation of Woods & Thomson (2004), are inferred from broad-band fits to the X-ray spectra. Consequently, their uncertainties are difficult to quantify, though likely they are below 10% (see text).

[a]Uncertainty in the distance is dominated by the width of the bins in K, about 15%.

1E 1841−045. The reddening shows an enormous jump at 3.5–4 kpc, associated with the Scutum arm. The estimated reddening of the source, however, is larger still, and places it behind this spiral arm. We thus can only set a lower limit on its distance, $d > 5\,\mathrm{kpc}$. Fortunately, this AXP is associated with a supernova remnant, Kes 73, for which the estimated distance of 7 kpc (derived from HI absorption measurements; Vasisht & Gotthelf, 1997) is consistent with our analysis. We use the latter value below.

XTE J1810−197. The reddening shows a large jump at $\sim 3\,\mathrm{kpc}$, from $A_V = 4$ to 13. Since the AXP's estimated reddening of $A_V = 7.8$ is inside this range, the object is almost certainly confined to the spiral arm that causes the jump. While the reddening estimate is less secure, since it is based on a fit to the broad-band X-ray spectrum, the jump seen in the run of reddening as a function of distance is so large that the distance measurement should be secure. With this distance, XTE J1810−197 is probably the closest of the AXPs. Our estimate is consistent with the results of Gotthelf et al. (2004), who used the extinction estimated from the X-ray spectrum to suggest a distance in the range 3–5 kpc (based on optical reddening studies), and set a firm upper limit to the distance of 5 kpc by comparing with the hydrogen column and distance inferred from HI measurements to a nearby (but unassociated) supernova remnant.

6.6 Comparison with Previous Work

Above, we have taken estimates of the reddening to AXPs and used them to infer distances by matching them against the run of reddening with distance inferred from red-clump stars. Here, we compare these estimates with results for three AXPs that have been studied in detail. We also include known reddenings and distances of objects near the AXPs as test-cases for the red-clump method, particularly near 1E 2259+586.

6.6.1 4U 0142+61

Hulleman et al. (2004) discussed the various distance estimates for 4U 0142+61, which range from 1 kpc to 4 kpc.

The near edge of the Perseus Arm (as defined by its forward shock) is located at a distance of about 3–3.5 kpc in this direction (e.g., Cordes & Lazio 2002, and references therein), with dense material and stars within a few 100 pc of this. Our distance estimate of 3.8 ± 0.4 kpc is fully consistent with the AXP being in this arm.

Our inferred run of reddening with distance is consistent (and greatly improves upon) what was derived from spectral-energy distribution fits of field stars by Hulleman et al. (2004). For further verification, we also obtained low-resolution classification spectra for a number of brighter stars within a few arcminutes of the source, using the David Dunlap 1.88 m telescope at Richmond Hill, Canada. From the spectral types and the observed optical magnitudes and colours, we confirm that out to a distance of ~ 3 kpc, the reddening does not rise above $A_V = 2$. Unfortunately, however, our sample did not include any stars at greater distance and reddening.

6.6.2 1E 1048.1−5937

Our distance estimate of 8.9 ± 1.9 kpc is in stark disagreement with the estimate of $\sim$2.7 kpc derived by Gaensler et al. (2005) from an HI bubble that is positionally coincident with the source and has no other known source. Our estimate places the AXP towards the far side of the Carina Arm rather than the near edge. Gaensler et al.'s distance would be very hard to reconcile with the large extinction towards this source, since there is little interstellar dust out to 2.7 kpc. We therefore suggest that the bubble Gaensler et al. found is not associated with the AXP.

To check the performance of the red-clump method in this most complex of fields, we compare the function $A_V(d)$ found above with measured distances and reddenings of different types of source in the field: open clusters (from Loktin et al, 1994), Wolf-Rayet stars (van der Hucht, 2001), O-stars (from Garmany et al. 1982) and other early-type stars (Guarinos, 1992) within $40'$of the source. Figure 6.9 shows all these data against the reddening curve found for 1E 1048.1−5937 above. Although, as shown in §6.4, there is a fair amount of scatter due to inhomogeneous reddening in the field, the general trend of reddening with distance is well-followed by all of the data-sets, with the notable exception of WR 29 (at large distance and low reddening). Crucially, none of them indicate the presence of $A_V > 3$ up to 4 kpc, so the AXP would need a substantially lower column than that inferred from the X-ray spectrum in order to be at the distance of Gaensler et al's interstellar bubble.

We also checked the extinction model of Drimmel et al. (2003) to see if their results were consistent with ours. We found that their predicted extinction along this line of sight is consistently higher than ours in the 4–8 kpc range. This is not surprising, given that we know from Gaensler et al. that the source lies through a hole in the interstellar extinction. The Drimmel et al. curve is consistent with curves 2, 3 and 4 from Figure 6.3.

6.6.3 1E 2259+586

The supernova remnant CTB 109, thought to be associated with the AXP 1E 2259+586, has been the subject of a number of studies to try to determine its distance and reddening, with range of previous distance estimates for the magnetar and SNR as about 3 to 7 kpc (Kothes et al. 2002, introduction). Most recently, Kothes et al. (2002) inferred that CTB 109 was at a distance of 3 kpc, from the following argument. The supernova remnant is apparently interacting with a large molecular cloud in the direction $l \approx 108.8°$, $b \approx -0.9°$. This cloud has a velocity of $-50\,\mathrm{km\,s^{-1}}$, which is similar to the range of $-30\ldots-55\,\mathrm{km\,s^{-1}}$ found for several HII regions within a few degrees of the remnant. For these latter regions, spectroscopic distance have been measured, which group around a distance $d = 3\,\mathrm{kpc}$. This is rather nearer by than expected based on the standard rotation curve for this direction, premably because of streaming motion known to be associated with the Perseus Arm shock.

A distance of 3 kpc for 1E 2259+586, however, is excluded by our analysis: at 3kpc, there are no red-clump stars sufficiently highly reddened to be consistent with 1E 2259+589's column. One reason for the discrepancy might be that 1E 2259+589 is not associated with the SNR CTB 109. We believe this is unlikely, however, given both the positional coincidence and the morphology. Similarly, the shape of the remnant strongly suggests that it is indeed interacting with a dense molecular cloud positioned at the above mentioned co-ordinates.

Of the HII regions listed in Table 2 and shown in Figure 2 of Kothes et al. (2002), two have distances consistent with being behind the Perseus shock (Sh 149 and Sh 156, $d = 4\ldots8\,\mathrm{kpc}$). Interestingly, among the 11 regions with velocities similar to the cloud with which CTB 109 appears to be interacting ($v < -40\,\mathrm{km\,s^{-1}}$), these two are amongst the three closest to CTB 109 on the sky.

Figures 4 and 5 of Kothes et al. (2002) show CO and HI data in the direction of CTB 109. From these figures, there appear to be two components to the CO cloud West of the SNR: one which includes the "arm" which passes across the SNR (with velocity $-47\ldots-51\,\mathrm{km\,s^{-1}}$) and a second which does not ($-53\ldots-56\,\mathrm{km\,s^{-1}}$) . These two components show different morphology and span a large range in velocity, suggesting that they are physically distinct. The HI data is less clear, but the morphology at $-55\,\mathrm{km\,s^{-1}}$ again seems match what one would expect from interaction with the supernova remnant. Since the remnant is known not to be interacting with the "arm" (see Sasaki et al. 2004), the above-described morphology suggests it is likely interacting with the second, more distant cloud.

A resolution to the distance discrepancy would thus be that the foreground cloud, including the "arm" which partially covers CTB 109, is indeed involved in streaming motion, but that CTB 109 is interacting with a background cloud unconnected with the first. If this background cloud is not associated with the streaming motion, but follows the standard rotation curve ($\Theta_\odot = 220\,\mathrm{km\,s^{-1}}$, $R_\odot = 8.5\,\mathrm{kpc}$), then its distance is $\sim$6 kpc, which is consistent with our estimate for the distance of 1E 2259+589.

Finally, as an independent check, we note that the Wolf-Rayet star WR 158, which is at an angular separation of 6.1°, has a spectroscopic distance of $\sim 8\,\mathrm{kpc}$ and extinction $A_V \approx 4$ (van der Hucht, 2001). Another, WR 151, at a separation 6.8°, has $d \simeq 5.7\,\mathrm{kpc}$ and $A_V \approx 3.8$. These combinations of reddening and distance are consistent with our inferred run of reddening with distance (Fig. 6.7). Thus, we believe our distance estimate is reliable.

We check further that the red-clump method gives reasonable distances for objects of known reddening and distance in this part of the sky. The first object we check is Cas A, which is similar in some respects to CTB 109: it is a supernova remnant with a central compact X-ray source. The distance to Cas A is well known at $d = 3.4^{+0.3}_{-0.1}\,\mathrm{kpc}$ (Reed et al. 1995). Figure 6.10 shows the derived function $A_V(d)$ for 2000 stars within 10′of the position of Cas A. The reddening of the supernova remnant has been estimated from optical spectra and colors of various sections. The range of estimates of reddening is shown, which includes the majority of the estimates and the poorly measured hydrogen column for the central X-ray source (Fesen & Hurford, 1996; Fesen et al. 2006). (Some estimates lie outside this region, but we discount these extreme estimates). Clearly, the measured distance to the SNR is consistent with the reddening: our method gives a limit on the distance $d > 1.9\,\mathrm{kpc}$. Were we trying to find the distance to Cas A, we would have reasoned that it must reside in the spiral arm (since it is also the product of a short-lived, massive star), close to its known distance (shown by the vertical dashed line).

6.7 Implications

With our distances, X-ray luminosities for the AXPs [2] can be calculated from their unabsorbed flux (taken when they were not thought to be in outburst; we use the numbers from Woods & Thomson, 2004). The results are listed in Table 6.2. For comparison, we also include two sources not considered above, CXOU J010043.1−721134 and SGR 0526−66, for which reasonably good distances are known since they are located in the SMC and LMC, respectively. Of these, the first is thought to be an AXP (Lamb et al. 2002; Majid et al. 2004) and the latter is a Soft Gamma-Ray Repeater (SGR), another class of magnetar.

From Table 6.2, one sees that all Galactic AXPs have remarkably similar X-ray luminosities. In part, this may be a coincidence: all sources are known to vary to some degree, and XTE J1810−197 is a transient. Furthermore, while for SGR 0526−66, which is clearly brighter, one might appeal to it being a different type of source (see also below), the one extra-galactic AXP, CXOU J010043.1−721134 in the SMC, is substantially fainter. Nevertheless, taken together, the luminosities listed in Table 6.2 suggests that the emission mechanism responsible for the persistent soft X-rays is self-limiting in the AXPs, despite differences in their spectra and timing properties.

This result was predicted. Thompson & Duncan (1996, §3.6) noted that the soft X-ray luminosity of a magnetar must saturate at a value near $L_X \simeq 10^{35}\,\mathrm{erg\,s^{-1}}$, because at higher luminosities neutrino emission from the interior would become dominant and cause rapid cooling. Here, the precise limiting luminosity could be greater by a factor of a few, depending on the surface composition (the above limit is for iron, C. Thompson 2006, pers.

[2]The energy associated with the SNRs also depends on distance. For CTB 109, Sasaki et al. (2004) found an explosion energy of $0.7 \times 10^{51}(d/3\,\mathrm{kpc})^{2.5}$ erg, or $6 - 8{\times}10^{51}$ erg for our distance. This makes it a more energetic supernova than most, suggesting that perhaps AXPs generally have higher than typical supernova energies, in contrast to what was inferred previously (Vink, 2006; 2006, pers. comm.).

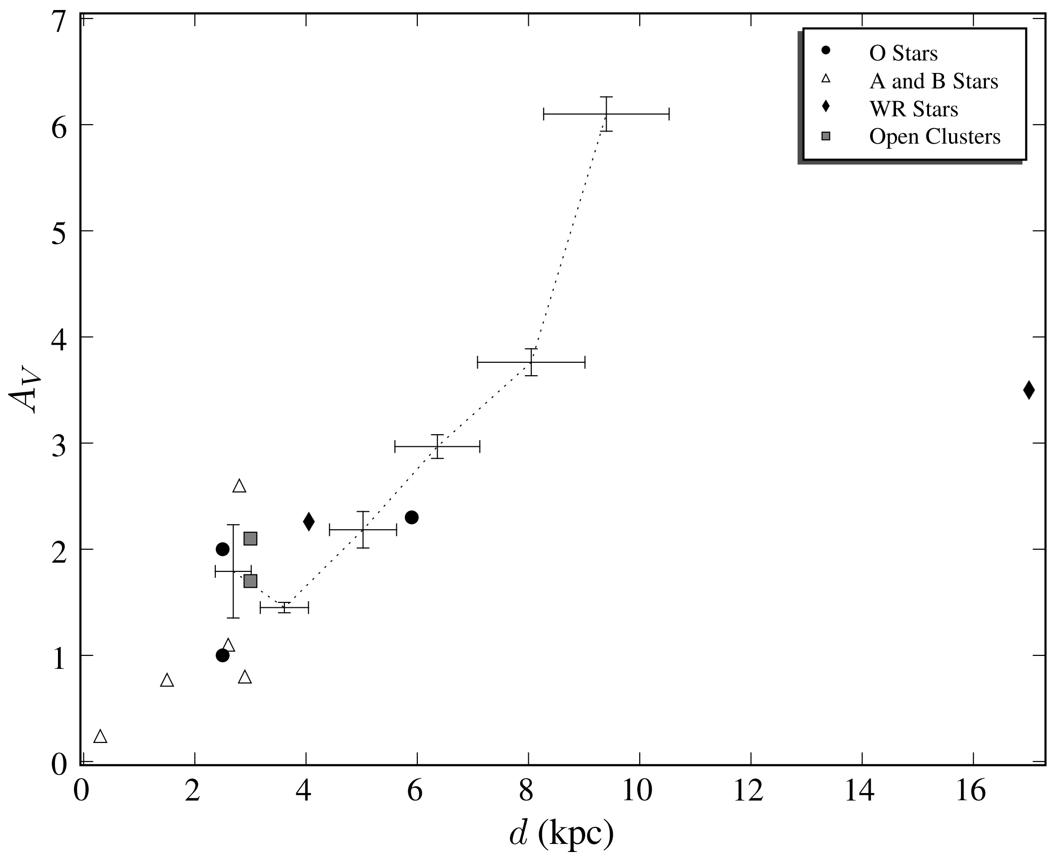

Figure 6.9 Comparison of reddening as a function of distance in the field of 1E 1048.1−5937 from the red-clump method (shown with error bars) with other reddening/distance determinations .

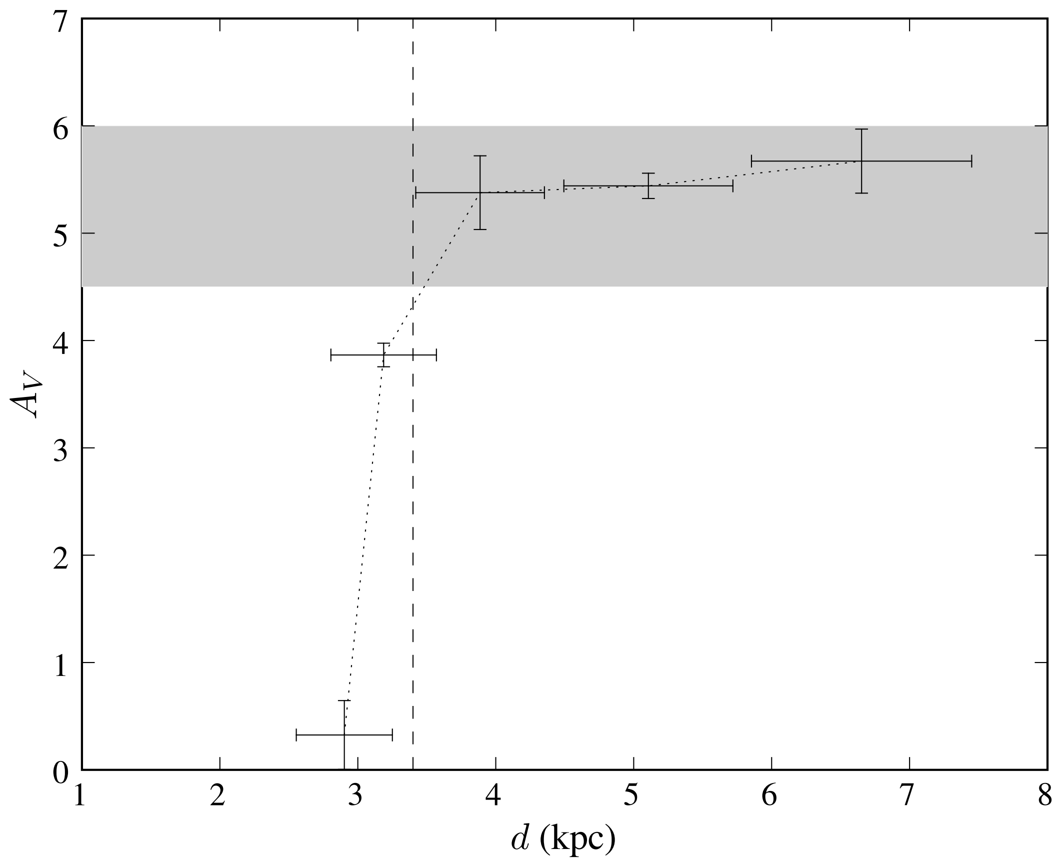

Figure 6.10 The red-clump method as applied to Cas A. The vertical dashed line is the estimated distance of Cas A, and the grey shaded region contains the majority of reddening estimates for the SNR and the central source (a range of estimates rather than the uncertainty on one estimate).

Table 6.2. Inferred quantities

Object	$L_X(2-10\,\mathrm{keV})$ ($10^{35}\,\mathrm{erg\,s^{-1}}$)	$\frac{L_{\mathrm{bb}}^{\mathrm{bol}}}{L_{X,2-10\,\mathrm{keV}}}$	B_{dipole} (10^{14} G)	T_{bb} (keV)	R_{bb} (km)	Pulsed Fraction (%RMS)
4U 0142+61	1.3	0.43	1.3	0.39	8.9	3.9
1E 1048.1−5937	1.4	0.13	3.9	0.63	1.7	62.4
1E 2259+589	1.3	0.11	0.6	0.41	4.2	23.2
1RXS J170849.0−400910	1.1	0.27	4.7	0.44	5.0	20.5
1E 1841−045[a]	1.1	0.32	7.1	0.44	5.5	13
XTE J1810−197[b]	1.3	0.56	2.9	0.67	2.6	42.8
CXOU J010043.1−721134	0.4[c]	…[c]	4.5	0.41[c]	<7[c]	33
SGR 0526−66	2.6	0.06	7.4	0.53	2.6	4.8

Note. — The dipole magnetic field strength B_{dipole}, black-body temperature T_{bb} and pulsed fraction are taken from the compilation of Woods & Thompson (2004). The black-body radius R_{bb} is calculated using the following fits: 0142, White et al. (1996); 1048, Mereghetti et al. (2004); 2259, Woods et al. (2004); 1708, Rea et al. (2003); 1841, Morii et al. (2003); 1810, Gotthelf et al. (2004); 0100, Lamb et al. (2002); 0526, Kulkarni et al. (2003). We do not list uncertainties, since these are dominated by source variability.

[a]We use the distance $d = 7\,\mathrm{kpc}$ derived by Sanbonmatsu & Halfand (1992); it is consistent with our lower limit of 5 kpc.

[b]From the spectrum taken soon after outburst; see Gotthelf et al. (2004).

[c]The numbers are inferred using the black-body only fit by Lamb et al. (2002). As a result, the temperature should be considered somewhat uncertain and the black-body radius is an upper limit. The spectrum can also be reproduced adequately with a power law (Majid et al. 2004); this yields the same 2–10 keV luminosity within about 20%.

comm.). Furthermore, Arras et al. (2002) found, from considerations of the amibipolar diffusion time-scale of the magnetar's internal magnetic field, that AXPs should remain near the limit for $10^3 \ldots 10^5$ yr (i.e., the typical characteristic ages of the AXPs, Woods & Thompson 2004) before exhausting their internal heat supply and cooling rapidly by photon emission from the surface. Thus, it appears that the tight clustering in L_X we find has a natural explanation in the context of the magnetar scenario. For a transient AXP, it would appear that the general luminosity is below the critical value, but that in outburst it is also limited by the threshold.

Typically, the soft X-ray spectra of the AXPs are fit with a composite model, consisting of a black-body and a power-law component. Presumably, the former arises from the neutron-star surface, and typically is responsible for the peak in the observed spectra. With our new distances, we can estimate the emitting area, or, equivalently, the effective black-body radius. This estimate should be fairly robust, since in essence it depends only on the wavelength and the measured flux of the spectral peak.

In Table 6.2, we list the inferred black-body radii for each of the AXPs, as well as a number of other physical parameters which one might expect to be related: the fraction of the total luminosity that is in the black-body component, the black-body temperature, the magnetic field strength inferred from the spin-down rate (assuming magnetic-dipole radiation), and the pulsed flux. All numbers were taken when the objects were thought to be in quiescence (with the exception of XTE J1810−197, which is a transient AXP).

From the Table, one sees that there is no obvious correlation with dipole magnetic field strenght, but the black-body radius and temperature are correlated, with temperature increasing for smaller effective radii. The strongest correlation, however, is between the pulsed fraction and black-body radius: they are well described by PF $\propto R_{\rm bb}^{-2}$. This suggests an inverse proportionality of pulsed fraction with emitting area, as might be expected if different sources had, e.g., different sizes of the regions near the magnetic poles, where heat conduction is largest. (Such a correlation should break down for sources with hot poles close to the rotation axis, or the rotation axis close to the line of sight. But for random mutual inclinations, such geometries are relatively rare, so it is not surprising that our list does not include such an exception.) Our result also implies that any high-energy power-law component within the 2–10 keV band must be tied strongly to the thermal photon flux, since otherwise the correlation would be weakened.

An open question, though, is what causes the differences between the AXPs. In general, one might expect hotter, smaller surfaces for stronger magnetic fields, since stronger fields should lead to larger differences in heat conduction across and along magnetic field lines. But we do not find any correlation with the field strength inferred from the spin-down rate. One possibility is that the latter is not a good measure for the field strength at the surface, e.g., because the surface field is dominated by higher-order multipole components. For that case, however, one might expect to see more complicated pulse shapes than are typically observed. Another possibility would be that the magnetic field strengths are roughly dipolar, but offset from the center (as typically inferred for magnetic white dwarfs and Ap stars; e.g., Wickramasinghe & Ferrario 2000). If so, the AXPs with the largest pulsed fractions might have the largest offsets, for which the effects of partial overlap between polar caps might lead to smaller effective radii.

While the above correlations are intriguing, one sees from Table 6.2 that there is one exception, SGR 0526−66. This object, although discovered in 1979 as the first SGR through its gamma-ray outbursts, is the most AXP-like of its class in its timing and spectral properties (Kulkarni et al. 2003). Yet, it flouts both the temperature and black-body radius correlations with pulsed fraction, and has a higher 2–10 keV luminosity than the limit inferred for the AXPs. The luminosity of the black-body component alone, however, is in the same range as for the AXPs. If the emission source for the thermal component is the same as it is for the AXPs, this suggests that the non-thermal component is powered at least partly from another, additional reservoir of energy. For instance, the energy could be stored in a large magnetic twist imparted during the previous gamma-ray bursting phase. Such magnetic twists are thought to decay on time scales of the order decades (Beloborodov & Thompson 2006), so it is possible that SGR 0526−66 has not yet returned to a quiescent, AXP-like state.

Intriguingly, it would seem that the AXPs, particularly 1E 1048.1−5937 and 1E 2259+586 seem to be located through gaps in the interstellar extinction. This likely is selection effect: the objects are detected primeraly in the soft X-ray band due to the sensitivities of the main X-ray observatories, and the X-ray spectra of the AXPs fall rapidly in the 2–10 keV range.

The only two AXPs with estimated hydrogen columns $N_H > 1.5 \times 10^{22}\,\mathrm{cm}^{-2}$, 1E 1841−045 and AX J1845−0258 were discovered through observations of the SNRs Kes 73 and Kes 75 respectively (Kriss et al. 1985; Gotthelf & Vasisht, 1998). This suggests that there may be many more AXPs in the Galaxy, which have not been discovered so far due to high extinction. They could, however, be discovered by their high-energy (>20 keV) emission, if it exists and is pulsed, as has been found for the AXPs detected by INTEGRAL so far (Kuiper et al. 2006).

6.8 Conclusions

We have applied the "red-clump" method to 2MASS data to construct the run of reddening versus distance in the directions of each of the Galactic AXPs. Combined with estimates of the reddenings to the AXPs, half of which are from our recent, model-independent determinations from photo-electric absorption edges in high-resolution X-ray spectra, we inferred distances. We found that two of these estimated distances are inconsistent with ones in the literature, but found likely reasons for the discrepancy in both cases and concluded that our results were reliable.

From the reddening versus distance diagrams, we find that the AXPs tend to fall in regions of rapidly rising reddening that are associated with spiral arms. This is not surprising, since they are the young remnants of short-lived massive stars. In particular, 4U 0142+61 has a position consistent with the Perseus Arm, 1E 1048.1−5937 lies on the far side of the Carina Arm, and 1XTE J1810−197 and 1RXS J170849.0−400910 fall along the Crux-Scutum arm. 1E 1841−045 could either lie in the Scutum arm or in the Molecular Ring, which dominates the gas and dust density at galactocentric distances of about 4 kpc (Dame et al. 2001). 1E 2258+586 falls near the end of the Outer Arm, known to exist in this direction beyond the Perseus arm (e.g., Kimeswenger & Weinberger 1989).

From our distances, we infer 2–10 keV luminosities and we find that these cluster tightly around $1.3 \times 10^{35}\,\mathrm{erg\,s^{-1}}$, consistent with the prediction in the context of the magnetar model that a saturating luminosity must exist above which rapid internal neutrino cooling is effective. Furthermore, we calculated effective emitting radii for the thermal components in the X-ray spectra, and find that these are inversely correlated with temperature, while the corresponding areas are inversely proportional to the pulsed fraction. This suggests the internal heating is released predominantly through one or more hot polar caps, with sizes that differ between the different AXPs.

The red-clump method can be applied to any line of sight in the Galactic plane, and is particularly useful combined with reddening estimates from X-ray spectroscopy. More accurate results may be obtained using deeper infrared imaging of selected fields, although, unfortunately, it may not be possible to extend the method to regions with very high reddening, since the red clump stars may well become confused with highly reddened main-sequence stars. As a result of the latter limitation, the method may not be generally useful for the other class of magnetars, the soft gamma-ray repeaters, which generally suffer very high extinction. It should be useful, however, for point sources such as the Compact Central Objects.

Generally, for further analysis of distances and structure within the Milky Way, it would be useful to cross-calibrate results from the red-clump method with those from X-ray absorption studies, X-ray dust scattering haloes, and HI and CO measurements.

Acknowledgments: We would like to acknowledge the thoroughness and many useful suggestions and comments of the anonymous referee. We thank David Kaplan for pointing out the paper describing the red-clump method to us, and Martin López-Corredoira for information on the applicability of the red-clump method. We also thank Bryan Gaensler for help with interpreting CO and HI data and for discussions about 1E 1048.1−5937, Manami Sasaki and Terrance Gaetz for discussing the case of CTB 109, and Tom Dame and Peter Martin for general discussions of Galactic gas and dust. This publication makes use of the Two Micron All Sky Survey, which is a joint project of the University of Massachusetts and the Infrared Processing and Analysis Center/California Institute of Technology, funded by NASA and NSF. Some of our data was based on data obtained at the David Dunlap Observatory, University of Toronto. We acknowledge financial support from NSERC.

Chapter 7

Conclusions

The AXPs were introduced in Chapter 1 as exotic, enigmatic objects, with a whole variety of poorly understood behaviour. An overarching theory, the magnetar model, has existed for some time and although this describes in, general, the evolution and energetics of the AXPs, it is short on detail. In this particular field, observations are indeed ahead of theory. What is required, then, is a systematic characterisation of the class, so that the emergent relationships can spur new thinking in the theoretical description. The preceding chapters contribute to this effort.

Next follows a very brief review of the main results, followed by the implications of this work and future developments. My work has focused both on the individual objects within the AXP group (counterparts and variability) and on the group as a whole (intrinsic spectra and distances/luminosities).

7.1 Review

7.1.1 Optical and Infrared Counterparts

The infrared and optical counterpart to 1E 1048.1−5937 was detected in quiescence following its initial discovery in outburst. The optical counterpart to CXOU J010043.1−721134 was discovered serendipitously from HST archival imaging, in one band only. The counterpart to 1E 1841−045 was not discovered despite deep infrared imaging; the crowding in the field was the main obstacle to good photometry. The infrared counterpart to 1RXS J170849.0−400910 was identified in archival adaptive optics and new deep imaging (refuting an earlier identification of another infrared source in the field).

The canon of AXP counterparts is thus complete (bar one). The X-ray to infrared flux ratios are very similar (unabsorbed $F_{2-10\,\mathrm{keV}}/F_K = 2700\ldots6000$ in quiescence), despite their temporal variability, suggesting not only that the emission mechanisms in the two wave-bands are connected, but that their relationship is the same for each AXP. For the two X-ray to optical flux ratios, CXOU J010043.1−721134 is significantly lower than 4U 0142+61 (unabsorbed $F_{2-10\,\mathrm{keV}}/F_V = 18$ and 460[1], respectively) suggesting that either the optical emission is different than the X-ray (or infrared) or that the object had varied considerably.

[1]This is for the old value of reddening. With the new value ($A_V = 3.5$), the ratio is even larger (~ 2000).

7.1.2 Variability

In the few data-points obtained for 1E 1048.1−5937, its K-band brightness varied by over a magnitude in a way which did not obviously correlate with either pulsed X-ray flux (2–10 keV) or with spin-down rate.

For 4U 0142+61, we obtained many data points in the infrared, optical and X-ray (unpulsed) to complement the pulsed X-ray flux measurements from RXTE. In the infrared, the shortest time-scale for variability was less than a day, with a dramatic dimming of over a magnitude (which coincided with the faintest R-band optical measurement). There is, however, no conclusive correlation of the variability in any of the wavebands with that in the pulsed X-ray flux. Similarly, there is no correlation between the fluxes in different optical bands. In the infrared, the fluxes in the JHK filters are correlated, varying the most in K (suggesting separate spectral components, with most variability at the long-wavelength end of the infrared, or a power-law with a varying slope).

7.1.3 Intrinsic Spectra

The interstellar column densities measured through X-ray absorption edges were consistent with the old measurements for three AXPs, but for 4U 0142+61 the column was $\sim 40\%$ lower than had been thought. This solved a number of outstanding problems with the old value. In the inferred intrinsic spectra, none of the AXPs showed evidence for the continuation of the 2–10 keV power-law component at lower energies (<1 keV). For 4U 0142+61, which has the most low-energy photons, the X-ray spectrum points reassuringly towards the optical photometry and shows a hint of a spectral feature at 14 Å ($\sim$800 eV), which could be interpreted as a cyclotron absorption from protons in a $\sim 1.5 \times 10^{14}$ G (whereas the dipole field as measured from the spin-down is $\approx 1.3 \times 10^{14}$ G).

7.1.4 Luminosities

By combining the red-clump method to construct the function of reddening versus distance, $A_V(d)$, with estimated reddenings for the AXPs, their distances were found. These distances are fairly accurate ($\sim 10\%$), as the AXPs tend to fall into regions of steeply rising reddening (spiral arms). Astoundingly, the 2–10 keV luminosities of the AXPs are the same ($\approx 1.3 \times 10^{36}$ erg s^{-1}) with the exception of CXOU J010043.1−721134 (in the SMC), which is too low (0.4×10^{36} erg s^{-1}). Furthermore, the luminosity of the one SGR with a known distance, SGR 0526−66 (in the LMC), is higher (2.6×10^{36} erg s^{-1}). Another surprise, was that the re-calculated black-body radii are anti-correlated with the pulsed fraction (related approximately $P.F. \sim R_{bb}^{-2}$).

7.2 Implications: From the Inside Out

The 2–10 keV X-ray luminosities of the AXPs are very similar. This is in spite of differences in spectral shape, pulsed fraction and dipole magnetic field. Since the flux in this part of the spectrum is dominated by the thermal peak, this suggests that the thermal luminosities of the AXPs are very similar. This heat originates in the stellar interior, from the decay of the magnetic field.

Thompson & Duncan (1996) predicted that there should be an upper limit to the amount of heat escaping from a neutron star. If the interior temperature rises above a critical threshold, then neutrino emission turns on (the emissivity is a very strong function of temperature) and transports the majority of the energy out of the neutron star. One thus expects that if the magnetic decay is sufficient to reach this temperature, the photon flux from the core will stay near the threshold, and the excess will come out in neutrinos (and that the temperature will remain near this threshold). The transient AXP, XTE J1810−197, also reached the same peak luminosity, albeit for only a short time, suggesting that the same threshold limited its thermal output. In the case of CXOU J010043.1−721134, the luminosity is less than the other AXPs, so either less heat is generated, or perhaps the neutrino emission mechanism is more efficient in this case. For SGR 0526−66, the luminosity is greater than the AXP limit, and this could be due to an extra thermal reservoir provided by its previous large flares, or additional surface heating caused by currents associated with a large magnetospheric twist (Thompson, Lyutikov & Kulkarni, 2002).

The pulsed fractions of the AXPs are very different from one-another, with no clear dependence on the inferred dipole magnetic field strength. Likely, the pulsations are due to the thermal emission arising predominantly in hot spots. The existence of such a thermal hot-spot is a natural consequence of the thermal conductivity's dependence on the magnetic field geometry and strength: since conduction is suppressed across field lines (and mildly enhanced along them), one would expect the core heat to reach the surface at the magnetic poles. One would also expect smaller poles (and thus a higher pulsed fraction) for stronger fields, but this is not what is seen. What, then, does the surface temperature profile depend upon? The dipolar field measured from the spin-down must not be the complete picture; the simplest explanations could be off-set dipoles (the closer the dipole to the surface, the smaller the hot area and greater the pulsed fraction), or an internal toroidal field, which creates a field more parallel to the surface at low magnetic latitudes, blanketing the hot core (Page et al. in prep.).

With model-independent measurements of the interstellar extinction (N_H), the intrinsic spectra of the AXPs can now be modelled. It must be the magnetosphere that creates not only the declining power-law tail (at the high-energy end of the thermal emission), but also the hard X-ray emission which dominates the AXP energetics. The current idea is that the thermal photons from the surface seed the declining tail, and affect the population of high-energy particles in the near-magnetosphere which are responsible for the hard X-ray emission. Neither process has been modelled in detail, but with the intrinsic spectrum known, this has now become possible. For instance, the declining power-law will now be well-defined independent of the modelling assumptions made, and so its relationship with spin-down, for example, can be found.

Since the black-body radii correlate so well with the pulsed fraction in the 2–10 keV range, both the thermal and declining tail must contribute to the effect, suggesting that the up-scattering of photons happens near the hot-spot.

According to the Beloborodov & Thompson (2006) model, the energy dissipation rate along a field line depends only on the amount of twist (because the pair creation threshold is easily reached, and regulates the footprint to footprint voltage). Helicity is delivered to the magnetosphere along field lines (see a simplified version in Figure 1.2) and so must include the poles. At the poles the density of flux bundles, all independently luminous of one-another, will be the highest. The model, therefore, predicts that the polar hot-spots should coincide with the location of most high-energy emission. The 20–150 keV hard X-ray emission is ∼100% pulsed in every case, and do not have pulsation peaks aligned with the 2–10 keV emission. This suggests that the hard X-rays are magnetospheric, but not spatially connected with the thermal emission. This would appear to contradict the Beloborodov & Thompson model. In particular, the surface thermal emission cannot be caused by thermalization in the dense crust of the same current, which causes the high-energy emission.

The (average) X-ray to infrared flux ratios are similar for the AXPs, as are their infrared colours. The optical emission is certainly magnetospheric, because of its large pulsed fraction, and although there may be a mid-infrared component from circumstellar material, the near infrared emission is probably magnetospheric too (it lies far above the X-ray thermal black-body and does not have a thermal shape). The constant flux ratio suggests that the infrared emission is powered by the thermal emission. Variability in the infrared and thermal X-rays do not generally correlate, suggesting that there is hysteresis in the system. The dimming event seen for 4U 0142+61 could be interpreted as a *short-out* or interruption of the magnetospheric current to large radii. Following a flare, the X-ray and infrared flux do correlate as they decay: a reservoir of energy (the initial flare) must have been distributed throughout the magnetosphere, affecting all emission channels.

XTE J1810−197 has recently been detected as a radio pulsar by Camilo et al. (2006), and shows a peculiarly flat spectrum, making it the brightest radio pulsar above 20 GHz. This demonstrates that there can be transitions between magnetar-like and radio pulsar-like behaviour, and, moreover, that the suppression of radio emission in AXPs is probably due to the magnetospheric currents rather than to the strong surface magnetic field alone. For XTE J1810−197, helicity must be released into the magnetosphere at a slow enough rate, such that the currents associated with it dissipate on a shorter time-scale, allowing the radio emission to switch on.

The X-ray to optical flux ratios for the only two sources measured are far from similar. The discrepancy seems too much to cover with chance variability: both the optical and X-ray luminosities are individually inconsistent. In this respect, CXOU J010043.1−721134 is the odd one out: it is the AXP with an 2–10 keV luminosity below the others, and may yet turn out not be a regular AXP (although it should be stressed, the optical identification needs to be confirmed). If the result holds up, then the optical emission must be decoupled from the X-rays – this was also suggested by the variability in the optical spectrum of 4U 0142+61.

The variability time-scales for the infrared emission, in particular, are short, of the order one day or less. Some level of variability exists throughout the spectrum (we await results from the hard X-ray band), with the lower energy emission varying by more than the high-energy emission. This makes sense in terms of cyclotron emission from currents in the magnetosphere: the lower-energy emission comes from large radii, where there are fewer particles. There is thus less inertia in magnetic and particle energies to withstand changes.

A consistent X-ray to infrared flux ratio may be expected from reprocessing by a circumstellar dusty debris disc, as the inner radius, temperature and density of the disc can all be controlled by the incident X-ray flux. The reprocessing timescale is very short, however, so it becomes hard to reconcile infrared and X-ray emission which do not correlate, in particular as the infrared has varied by a greater range than the X-ray. The dust could emit by reprocessing high-energy X-rays, which may be variable (something that, unfortunately, would be very hard to measure on the timescales of days, given the low count-rates involved).

From our studies of the extinction and distance, there is evidence that the AXPs are located preferentially along lines of sight passing through gaps between clouds. This could reflect the observational bias that they were discovered in soft X-rays (with the exception of 1E 1841−045 and AX J1845−0258, which have higher extinctions and were discovered through SNR observations). This raises the possibility that the number of AXPs in the galaxy is larger than had been thought; a more complete sample might be discovered in the 10–150 keV band. The SGRs, which were discovered through their high-energy outbursts, would not be affected by this, and have much higher typical extinctions. It may also be the case, that some neutron stars in binaries, which were assumed to be LMXB/HMXBs are, in fact, not accreting, but active magnetars. This would be relatively easy a investigate, and could yield a large population of thus far undiscovered AXPs.

7.3 Outlook

These studies have raised a number of concrete questions, that could be answered with further targeted observations:

- Phase-resolved infrared photometry of the brightest sources: is there a disc? is the infrared emission mechanism related to X-ray emission?
- A detailed measurement of the shape of 4U 0142+61's optical spectrum: is this an emission line or a break?
- Studies of CXOU J010043.1−721134 in the UV: is this source different from 4U 0142+61? is there any UV emission? could one obtain a detailed UV spectrum for this least extincted source?
- Infrared imaging to look for scattered light from SGR 1806−20 from light echoes: could this give a flare history in a similar manner to the work on Cas A? how often and over what time-scale do SGRs flare?
- Systematic phase-resolved X-ray spectroscopy of all AXPs: what components really are varying? how do the sources compare with one-another? A wealth of archival (XMM) data exists.
- Spitzer infrared spectrum of 4U 0142+61: is there any signature of dust?
- Daily (hourly?) multi-wavelength monitoring of 4U 0142+61: what is the variability timescale and instantaneous SED? do the components correlate when taken simultaneously?

More generally, the AXP emission is now sufficiently well characterised to allow detailed modelling. For instance, can the 2–10 keV emission (both spectrum and pulse profile) be reproduced in terms of thermal photons interacting with magnetospheric particles? Such an analysis will place constraints on the geometry of the magnetic field and on the energy distribution of magnetospheric particles (Fernández & Thompson, 2006, in prep).

The red-clump method and interstellar column determination have shown their power in deducing important information about the AXPs. This could be accomplished more effectively with more data, and using a direct calibration between X-ray absorption and infrared colour excess. Such a calibration could be found from the number of bright X-ray sources with known distances in the Galaxy. In this way, not only would the distances of the AXPs be much more accurately determined, but the technique could be applied to other X-ray sources, such as the Central Compact Objects. It may well turn out, that the various classes of neutron star are more similar than it would at first have appeared (as shown for the radio emission by Camilo et al. 2006). There may yet be many more AXPs discovered, either in binary systems or behind high extincting columns, that would make statistical comparisons of AXP properties meaningful.

The localisation of magnetars and the determination of supernova energies from SNR will shed light on their formation. If more magnetars can be discovered by observing in higher energies, or by re-analysis of binary systems, than this becomes even more tractable. There have been suggestions that magnetars are associated with high-mass star forming regions (e.g., from the new possible AXP in Westerlund 1; Muno et al. 2006) and possibly high-energy supernovae (Vink, 2006, pers comm). A more definite answer to this question may elucidate the difference between the types of neutron stars.

The tentatively detected feature in the X-ray spectrum of 4U 0142+61 augers well for finding physical implications: the shape and variability of the feature (if confirmed) will give valuable information about the emission mechanism: for example, if it is an electron absorption line, then does it correlate with the magnetospheric current density (as shown by the 2–10 keV spectral tail, for instance)? Here, we are finally getting a handle on the physical processes in the regime of interest: the intense magnetic field in the near magnetosphere.

In summary, a large amount of information about the AXPs has been uncovered, which makes it possible to constrain the physical processes of magnetar interiors and magnetospheres. New questions have presented themselves, and new observational avenues have opened up, promising a wealth of new knowledge in the coming few years. Now the main task is to attempt to model all of this in a cohesive physical model.

Bibliography

[1] Anders, E., Grevesse, N., 1989, Geochimica et Cosmochimica Acta, 53, 197

[2] Akiyama, S., Wheeler, C., Meier, D., Lichtenstadt, I., 2003, ApJ, 584, 954

[3] Alpar, M. A., Ankay, A., Yazgan, E., 2001, ApJ, 557, L61

[4] Arras, P., Cumming, A., Thompson, C., 2004, ApJ, 608, L49

[5] Asplund, M., Grevesse, N., Jacques Sauval, A., 2004, in *Cosmic Abundances as Records of Stellar Evolution and Nucleosynthesis*, ASP Conference Series, eds F. N. Bash and T. G. Barnes

[6] Baade, W., & Zwicky, F., 1934, Phys. Rev., 45, 138

[7] Bahcall, J. N., Basu, S., Serenelli, A. M., 2005, ApJ, 631, 1281

[8] Balucinska-Church, M., McCammon, D., 1992, ApJ, 400, 699

[9] Baring, M., Harding, A., 1998, ApJ, 507, L55

[10] Beloborodov, A & Thompson, C., 2006, ApJ submitted, (`arXiv:astro-ph/0602417`)

[11] Bessell, M., Brett, J., 1988, PASP, 100, 1134

[12] Burwitz, V., Haberl, F., Neuhäuser, R., Predehl, P., Trümper, J., Zavlin, V. E., 2003, A&A, 399, 1109

[13] Cameron, P., Chandra, P., Ray, A., Kulkarni, S., Frail, D., Wieringa, M., Nakar, E., Phinney, E., Miyazaki, A., Tsuboi, M., Okumura, S., Kawai, N., Menten, K., Bertoldi, F., 2005, Nature, 434, 111

[14] Camilo, F., Kaspi, V., Lyne, A., Manchester, R., Bell, J., D'Amico, N., McKay, N, Crawford, F, 2000, ApJ, 541, 367

[15] Camilo, F., Ransom, S., Halpern, J., Reynolds, J., Helfand, D., Zimmerman, N., Sarkissian, J., 2006, Nature, submitted.

[16] Carraro, G., Romaniello, M., Ventura, P., Patat, F., 2004, A&A, 418, 525

[17] Chadwick, J., February, 1932, Nature, p.312

[18] Chatterjee, P., Hernquist, L., Narayan, R., 2000, ApJ, 534, 373

[19] Cline, T., Desai, U., Pizzichini, G., Teegarden, B., Evans, W., Klebesadel, R., Laros, J., Hurley, K., Niel, M., Vedrenne, G., 1980, ApJ, 237, L1

[20] Cordes, J., & Lazio, T., 2002, arxiv:astro-ph/0207156

[21] Crampton, D. & Murowinski, R., 2004, SPIE, 5492, 181

[22] Curti, R. et al. (2003) VizieR On-line Data Catalog: II/246. Originally published by: University of Massachusetts and Infrared Processing and Analysis Center (IPAC/California Institute of Technology)

[23] Dall'Osso, S., Israel, G., Stella, L., Possenti, A., Perozzi, E., 2003, ApJ, 599, 485

[24] Dame, T., Hartmann, D. & Thaddeus, P., 2001, ApJ, 547, 792

[25] den Hartog, P. R., Hermsen, W., Kuiper, L., Vink, J., in 't Zand, J., Collmar, W., 2006, A&A, 451, 587

[26] den Herder, J., et al., 2001, A&A, 365, L7

[27] Dhillon, V., Marsh, T., Hulleman, F., van Kerkwijk, M., Shearer, A., Littlefair, S., Gavriil, F., Kaspi, V., 2005, MNRAS, 363, 609

[28] Dib, R., Gonzalez, M., Kaspi, V., Gavriil, F., 2006, ApJ, submitted

[29] Dolphin, A., 2000, PASP, 112, 1383

[30] Drake, J., Testa, P., 2005, Nature, 436, 525

[31] Drimmel, R., Cabrera-Lavers, A. & López-Corredoira, M., 2003, A&A, 409, 205

[32] Duncan, R., 2000, American Institute of Physics Conference Series, 526, 830

[33] Duncan, R. & Thompson, C., 1992, ApJ, 392, L9

[34] Durant, M., & van Kerkwijk, M., 2005, ApJ, 632, 563 (§3.2)

[35] Durant, M., & van Kerkwijk, M., 2005a, ApJ, 627, 376 (Chapter 2)

[36] Durant, M., & van Kerkwijk, M., 2005b, ApJ, 628, L135 (§3.1)

[37] Durant, M., & van Kerkwijk, M., 2006a, ApJ, accepted (Chapter 5)

[38] Durant, M., & van Kerkwijk, M., 2006b, ApJ, accepted (Chapter 6)

[39] Durant, M., & van Kerkwijk, M., 2006c, ApJ, accepted (§3.3)

[40] Durant, M., & van Kerkwijk, M., 2006d, ApJ. accepted (Chapter 4)

[41] Eichler, D., Gedalin, M., Lyubarsky, Y., 2002, ApJ, 578, L121

[42] Epps, H. & Miller, J., 1998, SPIE, 3355, 48

[43] Ertan, Ü., Alpar, M. A, 2003, ApJ, 593, L93

[44] Ertan, Ü., Erkut, M., Ekşi, K., Alpar, M. A., 2006, ApJ submitted (astro-ph/0606259)

[45] Fesen, R. & Hurford, A., 1995, AJ, 110, 747

[46] Fesen, R. & Hurford, A., 1996, ApJS, 106, 563

[47] Fesen, R., Pavlov, G., Sanwal, D., 2006, ApJ, 636, 848

[48] Ferrario, L., Wickramasinghe, D., 2006, MNRAS, 367, 1323

[49] Garmany, C., Conti, P., Chiosi, C., 1982, ApJ, 263, 777, Vizier on-line catalogue II/82

[50] Gaensler, B., Slane, P., Gotthelf, E., Vasisht, G., 2001, ApJ, 559, 963

[51] Gaensler, B., McClure-Griffiths, N., Oey, M., Haverkorn, M., Dickey, J., Green, A., 2005, ApJ, 620, L95

[52] Gavriil, F., Kaspi, V., & Woods, P., 2002, Nature, 408, 689

[53] Gavriil, F. & Kaspi, V., 2002, ApJ, 567, 1067

[54] Gavriil, F., & Kaspi, V., 2004, ApJ, 609, L67

[55] Göhler, E., Staubert, R., Wilms, J., 2004, MmSAI, 75, 464

[56] Gotthelf, E., Gavriil, F., Kaspi, V., Vasisht, G., Chakrabarty, D., 2002, ApJ, 564, L31

[57] Gotthelf, E., Halpern, J., Buxton, M., Bailyn, C., 2004., ApJ, 605, 368

[58] Gotthelf, E., Vasisht, G., 1998, NewAts, 3, 293

[59] Gould, R. J., Jung, Y., 1991, ApJ, 373, 271

[60] Gregory, P., Fahlman, G., 1980, Nature, 287, 805

[61] Guarinos, 1992, Ph.D. Thesis, Strasbourg Observatory, Vizier on-line catalogue V/86

[62] Hewish, A., Bell Burnell, S. J., Pilkington, J., Scott, P., Collins, R., 1968, Nature, 217, 709

[63] Hilditch, R., Howarth, I., Harries, T., 2005, MNRAS, 357, 304

[64] Ho, W., Lai, D., 2003, MNRAS, 338, 233

[65] Hodapp, K., Jensen, J., Irwin, E., Yamada, H., Chung, R., Fletcher, K., Robertson, L., Hora, J., Simons, D., Mays, W., Nolan, R., Bec, M., Merrill, M., Fowler, A., 2003, PASP, 115, 1388

[66] Hook, I., Jrgensen, I., Allington-Smith, J., Davies, R., Metcalfe, N., Murowinski, R., Crampton, D., 2004, PASP, 116, 425

[67] Hulleman, F., van Kerkwijk, M., & Kulkarni, S., 2000, Nature, 408, 689

[68] Hulleman, F., Tennant, A., Van verkwijk, M., Kulkarni, S., Kouveliotou, C., Patel, S., 2001, ApJ, 563, L49

[69] Hulleman, F., van Kerkwijk, M., & Kulkarni, S., 2004, A&A, 416, 1037

[70] Ibrahim, A., Markwardt, C., Swank, J., Ransom, S., Roberts, M., Kaspi, V., Woods, P., Safi-Harb, S., Balman, S., Parke, W., Kouveliotou, C., Hurley, K., Cline, T., 2004, ApJ, 609, L21I

[71] Israel, G., Mereghetti, S., Stella, L., 1994, ApJ, 433, L25

[72] Israel, G., Covino, S., Stella, L., Campana, S., Marconi, G., Mereghetti, S., Mignani, R., Negueruela, I., Oosterbroek, A., Parmar, A., Burderi, L., & Angelini, L., 2002, ApJ, 580, L143

[73] Israel, G., Covino, S., Perna, R., Mignani, R., Stella, L., Campana, S., Marconi, G., Bono, G., Mereghetti, S., Motch, C., Negueruela, I., Oosterbroak, T., & Angelini, L., 2003, ApJ, 589, L93

[74] Israel, G., Stella, L., Covino, S., Campana, S., Angelini, L., Mignanini, R., Mereghetti, S., Marconi, G., Penna, R., 2004, IAU Symposium 218

[75] Jahoda, K., Swank, J., Stark, M., Strohmayer, T., Zhang, W., & Morgan, E. 1996, Proc. SPIE, 2808, 59

[76] Jensen, G., 1999, Bulletin of the American Astronomical Society, 32, 724

[77] Jewitt, D., Luu, J., Chen, J., 1996, AJ, 112, 1225

[78] Juett, A., Marshall, H., Chakrabarty, D., Schulz, N., 2002, ApJ, 568, L31

[79] Juett, A. M., Schulz, N. S., Chakrabarty, D., Canizares, C. R., 2003, AAS HEAD meeting 7, 06.02

[80] Juett et al, 2006, ApJ, accepted (astro-ph/0605674)

[81] Kaspi, V., Lackey, J., Chakrabarty, D., 2000, ApJ, 537, L31

[82] Kaspi, V., Gavriil, F., Chakrabarty, D., Lackey, J., & Muno, M., 2001, ApJ, 558, 253

[83] Kern, B., & Martin, C., 2002, Nature, 417, 527

[84] Kimeswenger, S., Weinberger, R., 1989, A&A, 209, 51

[85] Kobayashi, N., et al. 2000, IRCS: Infrared Camera and Spectrograph for the Subaru Telescope, in Proc. SPIE 4008: Optical and IR Telescope Instrumentation and Detectors, eds M. Iye & A. F. Moorwood, 1056

[86] Kothes, R., Uyaniker, B., Yar, A., 2002, ApJ, 576, 169

[87] Kouveliotou, C., Eichler, D., Woods, P., Lyubarsky, Y., Patel, S., Göğüş, E., van der Klis, M., Tennant, A., Wachter, S., Hurley, K., 2003, ApJ, 596, L79

[88] Krause, O., Rieke, G., Birkmann, S., Le Floc'h, E., Gordon, K., Egami, E., Bieging, J., Hughes, J., Young, E., Hinz, J., Quanz, S., Hines, D., 2005, Science, 308, 1604

[89] Kriss, G., Becker, R., Helfand, D., Canizares, C., 1985, ApJ, 28, 703

[90] Kuiper, L., Hermsen, W. & Mendez, M, 2004, ApJ, 613, 1173

[91] Kuiper, L., Hermsen, W., den Hartog, P. R., Collmar, W., 2006, ApJ, 645, 556

[92] Kulkarni, S., Kaplan, D., Marshall, H., Frail, D., Murakami, T., Yonetoku, D., 2003, ApJ, 585, 948

[93] Lamb, R, Fox, D., Macomb, D., Prince, T., 2002, ApJ, 574, L29

[94] Landau, L., 1932, Phys. Z. Sowjetunion, 1, 285

[95] Lenzen, R., Hartung, M., Brandner, W., Finger, G., Hubin, N., Lacombe, F., Lagrange, A., Lehnert, M., Moorwood, A., Mouillet, D., 2003, SPIE, 4841, 944

[96] Lodders, K., 2003, ApJ, 591, 1220

[97] Loktin, A., Matkin, N., Gerasimenko, T., 1994, A&A T 4, 153, Vizier on-line catalogue V/96

[98] López-Corredoira, M., Labrera-Lavers, A., Garzón, F., & Hammersley, P., 2002, A&A, 394, 883

[99] Lyne, A., Pritchard, R., Graham-Smith, F., Camilo, F., 1996, Nature, 381, 497

[100] Lyutikov, M., 2003, MNRAS, 346, 540

[101] Lyutikov, M., & Gavriil, F., 2006, MNRAS, 368, 690

[102] Majid, W., Lamb, R., Macomb, D., 2004, ApJ, 609, 133

[103] Martini, P., Persson, S., Murphy, D., Birk, C., Shectman, S., Gunnels, S., Koch, E., 2004, Proc SPIE, 5492, 1653

[104] Mathis, J., 1990, ARA&A, 28, 37

[105] Matteucci, F., Chiappini, C., 2005, PASA, 22, 49

[106] Mereghetti, S., Caraveo, P., Bignami, G., 1992, A&A, 263, 172

[107] Mereghetti, S., Mignani, R., Covino, S., Chaty, S., Israel, G., Neuhäuser, R., Plana, H., Stella, L., 2001, MNRAS, 321, 143

[108] Mereghetti, S., Tiengo, A., Israel, G., 2002, ApJ, 569, 275

[109] Mereghetti, S., Tiengo, A., Stella, L., Israel, G., Rea, N., Zane, S., Oosterbroek, T., 2004, ApJ, 608, 427

[110] Middleditch, J., Nelson, J., 1976, ApJ, 208, 567

[111] Middleditch, J., Mason, K., Nelson, J., White, N., 1981, ApJ, 244, 1001

[112] Monet, D. et al., 2003, AJ, 416, 1037

[113] Moorwood, A., 1998, ESO Conference and Workshop Proceedings 55

[114] Morii, M., Sato, R., Kataoka, J. & Kawai, N., 2003, PASJ, 55, L45

[115] Morii, M., Kawai, N., Nataoka, J., Yatsu, Y., Kobayashi, N., Terada, H., 2005, Adv Sp Res., 35, 1177

[116] Morrison, R., McCammon, D., 1983, ApJ, 270, 119

[117] Motch, C., Belloni, T., Buckley, D., Gottwald, M., Hasinger, G., Pakull, M., Pietsch, W., Reinsch, K., Remillard, R., Schmitt, J., Trumpler, J., Zimmermann, H., 1991, A&A, 246, L24

[118] Muno, M., Clark, S., Crowther, P., Dougherty, S., de Grijs, R., Law, C., McMillan, S., Morris, M., Negueruela, I., Pooley, D., Portegies Zwart, S., Yusef-Zadeh, F., 2006, ApJ, 636, L41

[119] Neckel, T., Klare, G., & Sarcander, M., 1980, A&AS, 42, 251

[120] Oosterbroek, T., Parmar, A., Mereghetti, S., Israel, G. L., 1998, A&A, 334, 925

[121] Paczyński, B & Stanek, K., 1998, ApJ, 494, L219

[122] Patel, S., Kouveliotou, C., Woods, P., Tennant, A., Weisskopf, M., Finger, M., Göğüş, E., van der Klis, M., Belloni, T., 2001, ApJ, 563, L45

[123] Persson, S., Murphy, D., Krzeminski, W., Roth, M., Rieke, M., 1998, ApJ, 116, 2475

[124] Persson, S., Murphy, D., Gunnels, S., Birk, C., Bagish, A., Kock, E., 2002, ApJ, 124, 619

[125] Predehl, P., & Schmitt, J., 1995, A&A, 293, 889

[126] Press, W., Teukolsky, S. A., Vetterling, W., and Flannery, B., 1992, *Numerical Recipes: the art of scientific computing*, 2nd Edition, Cambridge University Press

[127] Rea, N., Israel, G., Stella, L., Oosterbroek, T., Mereghetti, S., Angelini, L., Campana, S., Covino, S., 2003, ApJ, 586, L65

[128] Rea, N., Oosterbroek, T., Zane, S., Turolla, R., Méndez, M., Israel, G. L., Stella, L., Haberl, F., 2005, MNRAS, 361, 710

[129] Reed, J., Hester, J., Fabian, A., Winkler, P., 1995ApJ...440..706

[130] Rho, J., Petre, R., 1997, ApJ, 484, 828

[131] Rigaut, F., Salmon, D., Arsenault, R., Thomas, J., Lai, O., Rouan, D., Veéran, J., Gigan, P., Crampton, D., Fletcher, J., Stilburn, J., Boyer, C., Jagourel, P., 1998, PASP, 110, 152

[132] Rousset, G., Lacombe, F., Puget, P., Hubin, N., Gendron, E., Fusco, T., Arsenault, R., Charton, J., Feautrier, P., Gigan, P., Kern, P., Lagrange, A., Madec, P., Mouillet, D., Rabaud, D., Rabou, P., Stadler, E., Zins, G., 2003, SPIE, 4839, 140

[133] Sanbonmatsu, K., Helfand, D., 1992, AJ, 104, 2189

[134] Sasaki, M., Plucinsky, P., Gaetz, T., Smith, R., Edgar, R., Slane, P., 2004, ApJ, 617, 322

[135] Schlegel, D., Finkbeiner, D., Davis, M., 1998, ApJ, 500, 525

[136] Schmelz, J., Nasraoui, K., Roames, J., Lippner, L., Garst, J., 2005, ApJ, 634, L197

[137] Shectman, S., & Johns, M., 2003, Proc SPIE, 4837, 910

[138] Seward, F., Charles, P., & Smale, A., 1986, ApJ, 305, 814

[139] Smith, J., Tucker, D., Kent, S., Richmond, M., Fukugita, M., Ichikawa T., Ichikawa, S., Jorgensen, A., Uomoto, A., Gunn, J., Hamabe, M., Watanabe, M., Tolea, A., Henden, A., Annis, J., Pier, J., McKay, T., Brinkmann, J., Chen, B., Holzman, J., Shimasaku, K., & York, D., , 2001, AJ, 123, 2121

[140] Smith, J., Tucker, D., Kent, S., et al. 2002, AJ, 123, 2121

[141] Guide Star Catatog 2.2, Space Telescope Science Institute (STScI) & Osservatorio Astronomico di Torino, 2001, Vizier catalog I/271

[142] Stanek, K., Udalski, A., Szymański, M., Kałużny, J., Mubiak, M., Mateo, M., Krzemiński, W., 1997, ApJ, 477, 163

[143] Stanek, K., Garnavich, P., 1998, ApJ, 503, L131

[144] i Stetson, P., 1987, PASP, 99, 191

[145] Stetson, P., 2000, PASP, 112, 925

[146] Strüder, L., et al., 2001, A&A, 365, L18

[147] Sugizaki, M., Nagase, F., Torii, K., Kinugasa, K., Asanuma, T., Matsuzaki, K., Koyama, K., Yamauchi, S., 1997, PASJ, 49, L25

[148] Takei, Y., Fujimoto, R., Mitsuda, K., Onaka, T., 2002,ApJ, 581, 307

[149] Tam, C., Kaspi, V., van Kerkwijk, M., Durant, M., 2004, ApJ, 617, L53

[150] Thompson, C., Duncan, R., 1993, ApJ, 408, 194

[151] Thompson, C. & Duncan, R., 1995, MNRAS, 275, 255

[152] Thompson, C. & Duncan, R., 1996, ApJ, 473, 322

[153] Thompson, C., Lyutikov, M., Kulkarni, S., 2002, ApJ, 574, 332

[154] Tiengo, A., Göhler, E., Staubert, R., & Mereghetti, S., 2002, A&A, 383, 182

[155] Tiengo, A., Mereghetti, S., Turolla, R., Zane, S., Rea, N., Stella, L., Israel, G., 2005, A&A, 437, 997

[156] Tolstoy, E., 1999, IAU Symposium 192, ASP, eds Whitelock, P. and Cannon, R.

[157] Turner, M., et al., 2001, A&A, 365, L27

[158] Ueda, Y., Mitsuda, K., Murakami, H., Matsushita, K., 2005, ApJ, 620, 274

[159] van der Hucht, K., 2001, New Astronomy Reviews, 45, 135 (Issue 3)

[160] van Kerkwijk, M., Kaplan, D., Durant, M., Kulkarni, S., Paerels, F., 2004, ApJ, 608, 432

[161] Vasisht, G., Gotthelf, E., 1997, ApJ, 486, L129

[162] Vink, J., Kuiper, L., 2006, MNRAS accepted, `astro-ph/0604187`

[163] Voges W., Aschenbach B., Boller T., Braeuninger H., Briel U., Burkert W., Dennerl K., Englhauser J., Gruber R., Haberl F., Hartner G., Hasinger G., Kuerster M., Pfeffermann E., Pietsch W., Predehl P., Rosso C., Schmitt J.H.M.M., Trümper J., Zimmermann H.U., 1999 A&A, 349, 389

[164] Wachter, S., Patel, S., Kouveliotou, C., Bouchet, P., Özel, F., Tennant, A., Woods, P., Hurley, K., Becker, W., & Slane, P., 2004, ApJ, 615, 887

[165] Wainscoat, R., Cowie, L., 1992, AJ, 103, 332

[166] Wang, Z. & Chakrabarty, D., 2002, ApJ, 579, L33

[167] Wang, Z., Chakrabarty, D., Kaplan, D., 2006, Nature, 440, 772

[168] Weisskopf, M., O'Dell, S., Paerels, F., Elsner, R., Becker, W., Tennant, A., Swartz, D., 2004, ApJ, 601, 1050

[169] Werner, D., & Yakovlev, D., 1995, A&AS, 109, 125

[170] White, N., Angelini, L., Ebisawa, K.,, Tanaka, Y., Ghosh, P., 1996, ApJ, 463, L83

[171] Wickramasinghe, D. T., & Ferrario, L., 2000, PASP, 112, 873

[172] Wilms, J.; Allen, A.; McCray, R., 2000, ApJ, 542, 914

[173] Woods, P., Kaspi, V., Thompson, C., Gavriil, F., Marshall, H., Chakrabarty, D., Flanagan, K., Heyl, J., Hernquist, L., 2004, ApJ, 605, 378

[174] Woods, P., & Thompson, C., 2004, in "Compact stellar X-ray sources", eds Lewin, W., van der Klis, M.

[175] Young, P., 2005, A&A, 444, L45

[176] Zane, S., Turolla, R., Stella, L., Treves, A., 2001, ApJ, 560, 384

[177] Zombeck, M., Chappell, J., Kenter, A., Moore, R., Murray, S., Fraser, G., & Serio, S., 1995, Proc. SPIE, 2518, 96